


Spring 5-12-2017

Pavement Surface Distress Detection, Assessment, and Modeling Using Geospatial Techniques

Su Zhang

University of New Mexico - Main Campus

Follow this and additional works at: https://digitalrepository.unm.edu/ce_etds

 Part of the [Civil and Environmental Engineering Commons](#), [Geographic Information Sciences Commons](#), and the [Remote Sensing Commons](#)

Recommended Citation

Zhang, Su. "Pavement Surface Distress Detection, Assessment, and Modeling Using Geospatial Techniques." (2017).
https://digitalrepository.unm.edu/ce_etds/169

This Dissertation is brought to you for free and open access by the Engineering ETDs at UNM Digital Repository. It has been accepted for inclusion in Civil Engineering ETDs by an authorized administrator of UNM Digital Repository. For more information, please contact disc@unm.edu.

Su Zhang

Candidate

Civil Engineering

Department

This dissertation is approved, and it is acceptable in quality and form for publication:

Approved by the Dissertation Committee:

Susan Bogus Halter, Chairperson

Christopher D. Lippitt

Guohui Zhang

Vanessa Valentin

**PAVEMENT SURFACE DISTRESS DETECTION,
ASSESSMENT, AND MODELING
USING GEOSPATIAL TECHNIQUES**

by

SU ZHANG

**BACHELOR OF CONSTRUCTION MANAGEMENT
AGRICULTURAL UNIVERSITY OF HEBEI**

JUNE, 2006

**MASTER OF CONSTRUCTION MANAGEMENT
THE UNIVERSITY OF NEW MEXICO**

AUGUST, 2010

**MASTER OF SCIENCE IN GEOGRAPHY
THE UNIVERSITY OF NEW MEXICO**

MAY, 2016

DISSERTATION

Submitted in Partial Fulfillment of the
Requirements for the Degree of

**Doctor of Philosophy
Engineering**

The University of New Mexico
Albuquerque, New Mexico

May 2017

Dedication

This dissertation is dedicated to my family, especially my wife and my grandfather. I will never be able to complete it without their support and encouragement. This dissertation is also dedicated to my advisors and colleagues in the Department of Civil Engineering, Department of Geography and Environmental Studies, and Earth Data Analysis Center.

Acknowledgements

I would like to express my great gratitude to Dr. Susan Bogus Halter, my academic advisor and dissertation committee chair, for providing me the opportunity to pursue my Ph.D. degree in Civil Engineering and work with her as her research assistant. Dr. Susan Bogus Halter is not only my academic advisor, but also my mentor and dear friend. Dr. Susan Bogus Halter's enormous support has encouraged me to do well in school and pursue my dreams.

I would also like to thank Dr. Christopher D. Lippitt, Dr. Guohui Zhang, and Dr. Vanessa Valentin for serving on my dissertation committee and guiding me in the research. I also appreciate their help for both my study at UNM and my life in the United States.

Thanks also go to my amazing colleagues in the Department of Civil Engineering, Department of Geography and Environmental Studies, and Earth Data Analysis Center at UNM for giving me advice and keeping me happy during my study. Without these colleagues, my dissertation could not have been completed.

Thank you all!

Pavement Surface Distress Detection, Assessment, and Modeling Using Geospatial Techniques

By

Su Zhang

Bachelor of Construction Management, Agricultural University of Hebei, 2006

Master of Construction Management, The University of New Mexico, 2010

Master of Science in Geography, The University of New Mexico, 2016

Doctor of Philosophy in Engineering, The University of New Mexico, 2017

Abstract

Roadway pavement surface distress information is essential for effective pavement asset management, and subsequently, transportation agencies at all levels dedicate a large amount of time and money to routinely collect data on pavement surface distress conditions as the core of their asset management programs. These data are used by these agencies to make maintenance and repair decisions. Current methods for pavement surface distress evaluation are time-consuming and expensive. Geospatial technologies provide new methods for evaluating pavement surface distress condition that can supplement or substitute for currently-adopted evaluation methods. However, few previous studies have explored the utility of geospatial technologies for pavement surface distress evaluation. The primary scope of this research is to evaluate the potential of three geospatial techniques to improve the efficiency of pavement surface distress evaluation,

including empirical analysis of high-spatial resolution natural color digital aerial photography (HiSR-DAP), empirical analysis of hyper-spatial resolution natural color digital aerial photography (HySR-DAP), and inferential geospatial modeling based on traffic volume, environmental conditions, and topographic factors. Pavement surface distress rates estimated from the aforementioned geospatial technologies are validated against distress data manually collected using standard protocols. Research results reveal that straightforward analysis of the spectral response extracted from HiSR-DAP can permit assessment of overall pavement surface conditions. In addition, HySR-DAP acquired from S-UAS can provide accurate and reliable information to characterize detailed pavement surface distress conditions. Research results also show that overall pavement surface distress condition can be effectively estimated based on the extent of geospatial data and inferential modeling techniques. In the near term, these proposed methods could be used to rapidly and cost-effectively evaluate pavement surface distress condition for roadway sections where field inspectors or survey vehicles cannot gain access. In the long term, these proposed methods are capable of being automated to routinely evaluate pavement surface distress condition and, ultimately, to provide a cost-effective, rapid, and safer alternative to currently-adopted evaluation methods with substantially reduced sampling density.

Table of Contents

Chapter 1 Introduction	1
Chapter 2 Literature Review.....	7
2.1 Roadway Pavement Surface Evaluation	7
<i>2.1.1 Roadway Networks.....</i>	<i>7</i>
<i>2.1.2 Pavement Surface Distress Evaluation.....</i>	<i>8</i>
<i>2.1.3 Pavement Surface Distress Evaluation Methods</i>	<i>13</i>
<i>2.1.3.1 Manual Evaluation.....</i>	<i>13</i>
<i>2.1.3.2 Automated Evaluation.....</i>	<i>15</i>
<i>2.1.3.3 Aircraft-based Evaluation.....</i>	<i>19</i>
2.2 Geospatial Technology (GT)	20
<i>2.2.1 Global Navigation Satellite Systems</i>	<i>21</i>
<i>2.2.2 Geographic Information Systems.....</i>	<i>23</i>
<i>2.2.3 Remote Sensing.....</i>	<i>24</i>
2.3 Gaps in Knowledge.....	27
Chapter 3 Extracting Pavement Surface Distress Conditions Based on High-Spatial Resolution Natural Color Digital Aerial Photography (HiSR-DAP).....	28
3.1 Introduction	28
3.2 Methodology	30
<i>3.2.1 Data Acquisition and Preparation</i>	<i>30</i>
<i>3.2.2 Image Processing.....</i>	<i>33</i>
<i>3.2.2.1 Image Aggregation.....</i>	<i>33</i>
<i>3.2.2.2 Evaluation Polygon Creation</i>	<i>33</i>
<i>3.2.2.3 Image Degradation</i>	<i>35</i>
<i>3.2.2.4 Spectral Response Extraction</i>	<i>36</i>
3.2.3 Multiple Linear Least Squares Regression Analysis.....	36
<i>3.2.3.1 Variables</i>	<i>36</i>
<i>3.2.3.2 Linear Regression</i>	<i>41</i>
<i>3.2.3.3 Validation.....</i>	<i>42</i>

3.3 Results and Discussion	43
3.4 Conclusions	49
Chapter 4 Characterizing Pavement Surface Distress Conditions with Hyper-spatial Resolution Natural Color Digital Aerial Photography (HySR-DAP)	51
4.1 Introduction	51
4.2 Materials and Methods	56
4.2.1 Data Acquisition and Preparation	57
4.2.2 Aerial Triangulation	61
4.2.3 Rutting Depth Measurement	64
4.2.4 Alligator Cracking Measurement	68
4.2.5 Transverse Cracking Measurement	70
4.2.6 Measurement Results Comparison	70
4.3 Results	73
4.4 Discussion	81
4.5 Conclusions	87
Chapter 5 Estimating Pavement Surface Distress Conditions with Geospatial Modeling	88
5.1 Introduction	88
5.2 Methodology	91
5.2.1 Data Acquisition and Preparation	91
5.2.1.1 Traffic Volume Interpolation for Unmeasured Locations	100
5.2.1.2 Explanatory Variable Values Extraction	103
5.2.2 Model Development	104
5.2.3 Model Validation	106
5.2.4 Determination of the Minimum Number of Survey Sites	107
5.3 Results and Discussion	108
5.4 Conclusions	115
Chapter 6 Summary and Conclusions	117
6.1 Summary of Research Results	117

6.1.1 <i>Appropriate Application of Each Proposed Method</i>	118
6.1.2 <i>Broader Research Impact</i>	119
6.2 Research Limitations	120
6.3 Implications for Future Research	121
REFERENCES	123
Appendix A. Flexible Pavement Distress Evaluation Reference Chart	153
Appendix B. Flexible Pavement Distress Types and Ratings	154
Appendix C. Rigid Pavement Distress Evaluation Reference Chart ...	155
Appendix D. Rigid Pavement Distress Types and Ratings	156
Appendix E. Illustration of Test Sections on Two-Lane and Four-Lane Highways	157

Table of Figures

Figure 1. Illustration of flexible pavement surface distress; (a) raveling and weathering; (b) bleeding; (c) rutting and shoving; (d) longitudinal cracking; (e) transverse cracking; (f) alligator cracking; (g) edge cracking; (h) patching.....	11
Figure 2. Illustration of rigid pavement surface distress; (a) corner break; (b) faulting of transverse joints and cracks; (c) joint seal damage; (d) lane/shoulder drop off; (e) longitudinal cracking; (f) patch deterioration; (g) spalling of joints and cracks; (h) transverse and diagonal cracks.....	12
Figure 3. Illustration of manual evaluation walking along the shoulder.	14
Figure 4. Automatic pavement surface distress evaluation system.	15
Figure 5. Exclusion of unwanted features on the images.	35
Figure 6. Correlation of predicted ODR versus actual ODR for (a) 6-inch, (b) 12-inch, (c) 24-inch natural color digital aerial photography.....	45
Figure 7. Examples of untethered low altitude AGL S-UAS; (a) rotary-wing S-UAS; (b) Fixed-wing S-UAS.....	58
Figure 8. The helium weather balloon small-unmanned aircraft system (S-UAS); (a) a filled helium weather balloon and a helium tank; (b) customized rigging and mounted Canon SX260 HS digital camera; the characteristics of the rigging are lightweight, durable, resilient, capable of protecting the sensor, capable of removing the string in the aerial images and capable of dynamically adjusting the sensor position (i.e., the lens always facing down the nadir or principal point); (c) balloon mapping kit, including a balloon, reels, gloves, rubber bands, and zip ties; (d) front facet of Canon SX 260 HS digital camera and Canon Hack Development Kit (CHDK) graphical user interface (GUI).....	59

Figure 9. An illustration of the RTK system in a base/rover configuration. 61

Figure 10. (a) An example of hyper-spatial resolution orthophotos with 0.003 m resolution and (b) an example of hyper-spatial resolution digital surface model (DSM) with 0.003 m resolution. The black to white color scale in (b) indicates elevations. 63

Figure 11. An illustration of the locations of rutting depth actual measured points and wooden bars. 66

Figure 12. Rutting depth calculation process. DA indicates the horizontal distance from Point A to Point D, while DB is the horizontal distance from Point B to Point D. RD indicates the calculated rutting depth. 67

Figure 13. An illustration of orthophoto-based alligator cracking measurement. The blue polygons are the digitized alligator cracking area while the red polygon is the entire manual evaluation zone. Areas for these polygons can be calculated with GIS software and therefore, alligator cracking area percentage can be determined by dividing alligator cracking area by the entire evaluation zone area. 69

Figure 14. An illustration of orthophoto-based transverse cracking measurement. The blue polylines are the digitized transverse cracking while the red polygon is the entire evaluation zone. The lengths of these transverse cracks and the length of the entire evaluation zone can be calculated with GIS software and, therefore, transverse cracking length can be determined by dividing total transverse cracking length by the entire evaluation zone length. 71

Figure 15. Box plot for each set of measurement. In each quadrant, the two boxes are ground-based measurement and HSR-AP derived products based measurement, respectively. (a) Inner wheel path rutting depth measurement; (b) outer wheel path rutting

depth measurement; (c) alligator cracking area percentage measurement; (d) transverse cracking length measurement. The uppermost bar is the maximum measurement value, while the lowermost bar is the minimum measurement value. The bar inside of the box indicates the median. The dots in (a) and (b) indicate measurement outliers..... 76

Figure 16. The frequency distribution of each distress' measurement differences (residuals); measurement difference is defined as the difference between ground-based measurement and HSR-AP derived products based measurement. (a) Inner wheel path rutting depth measurement difference; (b) outer wheel path rutting depth measurement difference; (c) alligator cracking area percentage measurement difference; (d) transverse cracking length measurement difference..... 77

Figure 17. Radar plot for each set of measurement. In each quadrant, the whole numbers (i.e., 1 to 28) adjacent to the outmost ring indicate each of the twenty-eight study sites. (a) Inner wheel path rutting depth measurement, and the decimal numbers adjacent to the multiple-rings indicate rutting depths in m; (b) outer wheel path rutting depth measurement, and the decimal numbers adjacent to the multiple-rings indicate rutting depths in m; (c) alligator cracking area percentage measurement, and the whole numbers adjacent to the multiple-rings indicate alligator cracking area percentages; (d) transverse cracking length measurement, and the whole numbers adjacent to the multiple-rings indicate transverse cracking length in m per km. 78

Figure 18. State of New Mexico and locations of surveyed mileposts. The yellow dots indicate the locations of mileposts and the number of total mileposts is 11,170..... 93

Figure 19. Data characterizing the environmental conditions of the State of New Mexico; AAP indicates average annual precipitation, AAMAT indicates average annual maximum

temperature, and AAMIT indicates average annual minimum temperature; (a) shows the total precipitation for the year of 2009; (b) shows the average annual precipitation (AAP) from 2005 to 2009; (c) shows the AAP from 2000 to 2009; (d) shows the average annual maximum temperature (AAMAT) for the year of 2009; (e) shows.....	95
Figure 20. Data characterize the soil types of the State of New Mexico.....	96
Figure 21. Data show the elevation of the State of New Mexico in shaded relief.....	97
Figure 22. Data show the slope of the State of New Mexico in degrees.	98
Figure 23. Data show the aspect of the State of New Mexico in degrees.....	99
Figure 24. Data characterizing the traffic volume of the State of New Mexico; Inverse distance weighted (IDW) method was used for spatial interpolation; (a) Interpolated AADT for the year of 2005; (b) Interpolated AADT for the year of 2006; (c) Interpolated AADT for the year of 2007; (d) Interpolated AADT for the year of 2008; (e) Interpolated AADT for the year of 2009; (f) Interpolated AADT for 5 years from 2005 to 2009.	102
Figure 25. Data characterizing the heavy vehicle traffic volume of the State of New Mexico; HV indicates heavy vehicle; Inverse distance weighted (IDW) method was used for spatial interpolation; (a) Interpolated HV AADT for the year of 2005; (b) Interpolated HV AADT for the year of 2006; (c) Interpolated HV AADT for the year of 2007; (d) Interpolated HV AADT for the year of 2008; (e) Interpolated HV AADT for the year of 2009; (f) Interpolated HV AADT for 5 years from 2005 to 2009.	103
Figure 26. Correlation of predicted ODR versus actual ODR for in-samples regression results; (a) 10,000 in-samples correlation; (b) 9,000 in-samples correlation; (c) 8,000 in-samples correlation; (d) 7,000 in-samples correlation; (e) 6,000 in-samples correlation; (f)	

5,000 in-samples correlation; (g) 4,000 in-samples correlation; (h) 3,000 in-samples correlation; (i) 2,000 in-samples correlation; (j) 1,000 in-samples correlation. 111

Figure 27. The distribution pattern of large residuals with a value greater than 35 or less than -35, which the RMSE of the 10,000 in-sample regression; residual is defined as the difference between predicted ODR and actual ODR; Global Moran's I test shows the *p*-value is less than 0.0001 and the Moran's I is 0.4292, meaning the large residuals are spatial autocorrelated. 113

Figure 28. Anselin Local Moran's I test results. HH indicates high values are surrounded by high values at a 95% confidence interval; LL means low values are surrounded by low values at a 95% confidence interval; HL indicates high values are surrounded by low values, while LH indicates low values are surrounded by high values. 114

Table of Tables

Table 1. Pearson Correlation Results of Texture Measurement of the 6-Inch, 12-Inch, and 24-Inch Natural Color Digital Aerial Photography	38
Table 2. Pearson Correlation Results of the Mean Value and Standard Deviation Value of the 6-Inch, 12-Inch, and 24-Inch Natural Color Digital Aerial Photography.....	39
Table 3. PCA Loadings of the Three Sets of Natural Color Digital Aerial Photography.	40
Table 4. Model Fit for Prediction of ODR Values.....	43
Table 5. Test of a Variety of Options to Infer Overall Distress Rates.....	47
Table 6. Model Validation for Prediction of ODR Values	48
Table 7. Error Summary for Predicted ODR	49
Table 8. Accuracy Assessment Result (RMSE) for Each Study Site. RMSE refers to root-mean-squared-error	64
Table 9. Rutting Depth Measurements for Inner and Outer Wheel Path (in m).....	74
Table 10. Alligator Cracking Area Percentage and Transverse Cracking Length Measurements	75
Table 11. Wilcoxon Signed Rank Test Results for Each Distress	79
Table 12. Levene’s Test and Bartlett’s Test Results.....	80
Table 13. Mann-Whitney U Test for Each Distress.....	81
Table 14. Best Available Datasets and Extracted Explanatory Variables	94
Table 15. Global Moran’s Test for New Mexico Traffic Volume.....	101
Table 16. Pearson Correlation Analysis of Explanatory Variables	105
Table 17. Multiple Linear Least Squares Regression Results Using 10,000 Sites	108
Table 18. Results of the Estimation Models based on Various Number of Samples	110

Chapter 1 Introduction

As one of the most critical types of transportation infrastructure, roadways provide a foundation to the performance of all national economies, delivering a wide range of economic and social benefits to citizens (Rodrigue et al. 2013). In most countries, roadways are the primary transport mode for both freight and passengers (Kveiborg and Fosgerau 2007; Mannering and Washburn 2012; Olamigoke and Emmanuel 2013; and Rodrigue et al. 2013).

Similar to other types of transportation infrastructure, roadways deteriorate over time due to various factors such as age, traffic load, and weather conditions (Hartgen et al. 2014). The serviceability of roads (i.e., the ability of a road to serve traffic) primarily depends on pavement surface conditions, and subsequently, road management agencies at all levels (i.e., federal, state, and local) dedicate large amounts of time and money to routinely evaluate pavement surface distress conditions as the core of their asset management programs. These pavement surface distress data are used by these agencies to make maintenance and repair decisions and ensure roadways meet functional standards and safety standards (Haas et al. 1994).

Currently, two types of pavement surface distress evaluation methods have been operationally adopted by state and local transportation agencies, including manual evaluation (human observation and human analysis) and automated evaluation (machine observation and machine analysis). Only a few state and local transportation agencies are still using manual methods to survey the surface distress of roadways (Bandini et al. 2012). Using this method, data are collected by inspectors on the ground through visual observation. Collected data are presented in the form of handwritten notes with pictures

attached. Analyzing these notes and pictures based on standard scoring protocols enables inspectors to determine the pavement surface distress on-site.

With automated evaluation methods, pavement surface condition data are still collected on the ground. The automated methods typically include the use of vehicle-mounted electronic sensors at a fine enough spatial resolution to detect individual distress measures (e.g., cracks) in the pavement surface. Both manual evaluation and automated evaluation methods are classified as ground-based evaluation methods because the evaluation action occurs from the ground.

All state transportation agencies use one of the two aforementioned types of pavement surface distress evaluation methods. Each of these methods has strengths and weaknesses (discussed in [Section 2.1.3](#)), but they have two weaknesses in common – time-consuming and expensive. For example, an annual manual evaluation of the highways across the State of New Mexico performed by New Mexico Department of Transportation (NMDOT) costs approximately one million dollars and three months (Montoya and Mann 2016). Another example is that the Vermont Agency of Transportation reported costs of up to \$170 per mile in urban areas for total combined costs for their adopted automated evaluation (McGhee 2004). For a state like New Mexico with over 15,000 lane miles, the total cost could reach three-million dollars.

The slow performance and high cost of manual and automated methods is caused by multiple reasons. For manual evaluation, the slow performance is caused by “boots on the ground” data collection, while the high cost is caused by the employment of experienced inspectors and enormous travel cost (inspectors are required to drive to the evaluation destination). For automated evaluation, the slow performance is also caused

by on the ground data collection, while the high cost is caused by deployment of special sensors, employment of specialized staff, and enormous travel cost (specialized operators are required to drive survey vehicles to perform evaluation statewide).

Another method to evaluate pavement surface condition, although it has not been used for any operational programs yet, is through airborne observation. The application of an analog aerial photography-based evaluation method to pavement surface distress was first implemented in the 1950s. However, extremely high cost, coarse spatial resolution, and limited compatibility with modern image processing techniques ultimately prevented the further exploration of their application for pavement surface evaluation at the time (McMaster and Legault 1952; Stoecker 1968; and Stoecker 1970). The transition from analog aerial photography to digital aerial photography occurred two decades ago since the first digital camera was placed on the market (Neumann 2008). Aerial photography has steadily stepped into a digital era characterized by low-cost, high-spatial resolution, and being compatible with numerous image processing techniques (Ahmad 2006), which warrants further exploration of the application of airborne observation for pavement surface distress evaluation.

Commonly known as geomatics, geospatial technology (GT) refers to a suite of technologies and practices used to acquire, store, analyze, and visualize spatially referenced data. An example of GT products is digital aerial photography. GT is the ideal tool to effectively collect and analyze pavement surface distress data since roadway infrastructure is fundamentally spatial (roadways are spatially and extensively distributed). With advances in computer hardware and software, the computation ability of GT has been empowered to process geospatial data rapidly.

One technique from GT, high-spatial resolution aerial imaging, has been used to routinely collect myriad high-spatial resolution (i.e., from 1-inch to 1-meter) digital aerial photography which contains pavement surface distress condition information. These data are processed, archived, and provided to the public for free. This publicly available high-spatial resolution digital aerial photography (HiSR-DAP) holds the potential to rapidly detect and assess overall pavement surface conditions with substantially reduced costs when comparing with ground-based evaluation methods.

Small-unmanned aircraft system (S-UAS) based hyper-spatial resolution imaging and automated aerial triangulation techniques from GT can be used to collect hyper-spatial resolution (millimeter scale) aerial images that have synoptic coverage of the ground features. These collected hyper-spatial resolution aerial images hold the potential to enable transportation agencies to rapidly detect and assess detailed pavement surface conditions at a lower cost.

Another technique from GT, geospatial modeling, is widely used to model natural phenomena that are influenced by various geospatial factors. Coupled with routinely collected and publicly available geospatial data, geospatial modeling techniques hold the potential to model overall pavement surface conditions with substantially reduced amount of survey sites, and ultimately, reducing the cost for pavement surface evaluation.

This dissertation explored the utility of GT approaches to rapidly detect and evaluate flexible pavement (i.e., asphalt concrete pavement) surface distress conditions. Asphalt concrete (AC) pavement is selected for this research since it is the most widely used roadway pavement material across the United States. Specifically, the research examined three novel GT-based pavement surface distress evaluation approaches through

the use of routinely acquired high-spatial resolution natural color digital aerial photography (HiSR-DAP), S-UAS acquired hyper-spatial resolution natural digital aerial photography (HySR-DAP), and geospatial modeling based on traffic volume, environmental conditions, and topographic factors to answer four research questions:

- (1) How well can routinely collected and publicly accessible HiSR-DAP evaluate overall pavement surface distress conditions?
- (2) How well can S-UAS collected HySR-DAP characterize detailed pavement surface distress conditions?
- (3) How well can overall pavement surface distress conditions be modeled using traffic volume, environmental conditions, and topographic factors?
- (4) What is the effect of sampling density on overall pavement surface distress condition estimation for unsampled road segments?

To answer question one, pixel-based spectral response extracted from routinely acquired 6-inch HiSR-DAP was modeled with overall pavement surface distress rates to determine their relationship assuming an L-resolution scene model (Strahler et al. 1986). To address question two, detailed pavement surface distress rates measured from S-UAS collected HySR-DAP were compared with distress rates manually measured on the ground to examine if S-UAS collected HySR-DAP can provide detailed and reliable primary observation suitable for characterizing detailed pavement surface distress conditions. To answer question three, variables extracted from traffic volume, environmental conditions, and topographic factors were modeled with overall pavement surface distress rates to determine their relationship through inferential geospatial modeling. Continued with the research of addressing question three, the amount of input

survey sites for the established model was reduced at a 10% decrement rate to identify a threshold of loss in estimation accuracy to answer question four.

Three distinctive abilities of GT, including synoptic coverage ability (i.e., data collected above the ground), computing ability (i.e., rapid data processing by modern computers), and data sharing ability (data can be used for other fields, e.g., vegetation monitoring), were fully used in the proposed three novel approaches for pavement surface distress condition evaluation. The expected general impact of this dissertation is to provide more cost and time efficient GT-based approaches to evaluate pavement surface distress conditions, and subsequently allow transportation agencies to more efficiently allocate limited resources (e.g., money and personnel) for roadway management. Specifically, the proposed HiSR-DAP based method could be potentially applied to rapidly and cost-effectively evaluate overall pavement surface distress condition for rapid, high-level information checks. The proposed HySR-based method could eventually lead to automation of S-UAS based evaluation of detailed pavement surface distress at a low cost which holds the potential to completely replace current ground-based evaluation methods. The proposed geospatial modeling based evaluation method would allow using existing geospatial data to estimate overall pavement surface distress conditions, while keeping limited survey sites for calibration/validation purposes. In the near term, these proposed methods could be used to rapidly and cost-effectively evaluate pavement surface distress conditions for roadway sections where field inspectors or survey vehicles cannot gain access. In the long term, these proposed methods are capable of being automated to provide a cost-effective, rapid, and safer alternative to currently-adopted evaluation methods with substantially reduced sampling density.

Chapter 2 Literature Review

This review of literature section covers two topics: roadway pavement surface evaluation and geospatial technology (GT). The reviewed literature includes books, journal papers, research reports, conference proceedings, and thesis or dissertations.

2.1 Roadway Pavement Surface Evaluation

This section first discusses the importance of roadway networks in a country's economy. Next the need for evaluation of roadway pavement surface is discussed. Lastly, the current methods for pavement surface distress evaluation are discussed.

2.1.1 Roadway Networks

Because of its intensive use, transportation infrastructure is a critical component of a country's economy as well as economic development at all levels (national, state, and local). In the United States, the importance of transportation infrastructure to the nation's economic strength and efficiency is widely accepted (Smith 1994). Without an effective transportation system, a nation or region cannot achieve the maximum use of its natural resources or the maximum productivity of its people (Garber and Hoel 2014). In general, transportation systems include roadway networks, rail networks, air networks, shipping networks, and pipeline networks (Mannering et al. 2009).

As one of the most important types of transportation infrastructure, roadway networks have played a significant role in the development and sustainability of human civilization from ancient times to the present, and continued to play an important role in regional and national economy (Mannering et al. 2009). In most countries, roadways are the primary transportation mode for both freight and passengers (Kveiborg and Fosgerau

2007; Mannering and Washburn 2012; Olamigoke and Emmanuel 2013; and Rodrigue et al. 2013). According to a survey conducted by the Federal Highway Administration (FHWA), over 90% of personal travel is accomplished by highways, and 25% of freight is moved via highways in the United States (fhwa.org).

2.1.2 Pavement Surface Distress Evaluation

Similar to other types of transportation infrastructure, roads deteriorate over time due to various factors such as traffic load, age, and weather conditions (Hartgen et al. 2014), which could lead to pose a risk to public safety and drivers' comfort (Aoki et al. 2012; Wang 2000). Therefore, maintenance of roadway pavement is essential to ensure good riding quality and avoid the happening of congestion, air pollution, and especially traffic accident (Chan et al. 2009).

Different levels of pavement management activities and decisions are supported by pavement conditions in varying degrees of detail (Haas et al. 1994). To characterize the conditions of existing pavements, surveys are conducted to assess one or more of the four criteria: surface distress, roughness, structural capacity, and surface friction (Gramling 1994; Alkire 2013). The aforementioned criteria vary in the degree of importance in terms of pavement performance and maintenance and rehabilitation needs.

Surface distress is damage or defects (e.g., cracks or rutting) observed on the pavement surface. Pavement surface distress surveys are performed to determine the type, severity, extent, and quantity of surface distresses. This information is often used to determine the overall distress conditions (e.g., Pavement Condition Index or PCI) which helps compute a rate of deterioration, and is often used to project future condition

(Shahin and Kohn 1979). Surface distress is typically the most important type of condition survey (Gramling 1994).

Roughness, also known as ride quality, indicates the ability of the pavement to provide a comfortable ride to the users. Roughness survey is performed to determine the pavement surface distortion along a linear plane. Roughness measurement is often converted into an index such as the pavement Present Serviceability Index (PSI) or the International Roughness Index (IRI). Roughness is considered very important by pavement management agencies (Gramling 1994).

Pavement surface distress and roughness are the basic elements typically included in quantification of the overall pavement condition, although structural capacity and friction may also be incorporated (Gramling, 1994; Prakash et al. 1994). Structural capacity is the maximum load and number of repetitions a pavement can carry before reaching some pre-defined condition. Structural analysis is normally conducted at the project-level to determine the pavement load-carrying capacity and the capacity needed to accommodate projected traffic volume. Structural capacity survey is important in the selection of treatments at the project-level (Gramling 1994).

Surface friction, also known as skid resistance, indicates the ability of the pavement to provide sufficient friction to avoid skid related safety problems. Surface friction survey is important and it is generally considered as a separate measure of the pavement condition and often can be used to determine the need for remedial maintenance by itself (Gramling 1994). Many transportation agencies employ traffic accident maps to locate high accident areas, and then an evaluation is performed to examine whether the accidents are related to friction problems (Gramling 1994).

In the transportation industry, serviceability is an effective indicator to represent the level of service that a pavement can offer to the users. The serviceability of roads (i.e., the ability of a road to serve traffic) primarily relies on pavement surface conditions, and subsequently, transportation management agencies at all levels (i.e., federal, state, and local) dedicate large amounts of time and money to routinely evaluate pavement surface distress conditions as the core of their asset management programs. The collected pavement surface condition data are used by these agencies to determine the serviceability of individual roads to make maintenance and repair decisions. Effective pavement surface distress evaluation is also necessary to measure the effectiveness of various maintenance techniques and repair methods (Hudson and Uddin 1987). Therefore, pavement surface distress evaluation is essential for any roadway pavement management programs.

This research focuses on pavement surface distress evaluation. Different transportation management agencies use different protocols for evaluating pavement surface distress condition. Typically surface distress data are collected in accordance with the criteria adopted by each state transportation agency. However, in general data for the following surface distresses are rated on a severity/extent scale of N/A, low, medium, and high for flexible pavements (i.e., asphalt concrete or AC pavement). Figure 1 shows the surface distresses for flexible pavements (Appendix A and B).

Likewise, in general data for the following surface distresses are rated on a severity/extent scale of N/A, low, medium, and high for rigid pavement (i.e., reinforced concrete pavement). Figure 2 shows the surface distresses for rigid pavements (Appendix C and D).



(a)



(b)



(c)



(d)



(e)



(f)



(g)



(h)

Figure 1. Illustration of flexible pavement surface distress; (a) raveling and weathering; (b) bleeding; (c) rutting and shoving; (d) longitudinal cracking; (e) transverse cracking; (f) alligator cracking; (g) edge cracking; (h) patching.

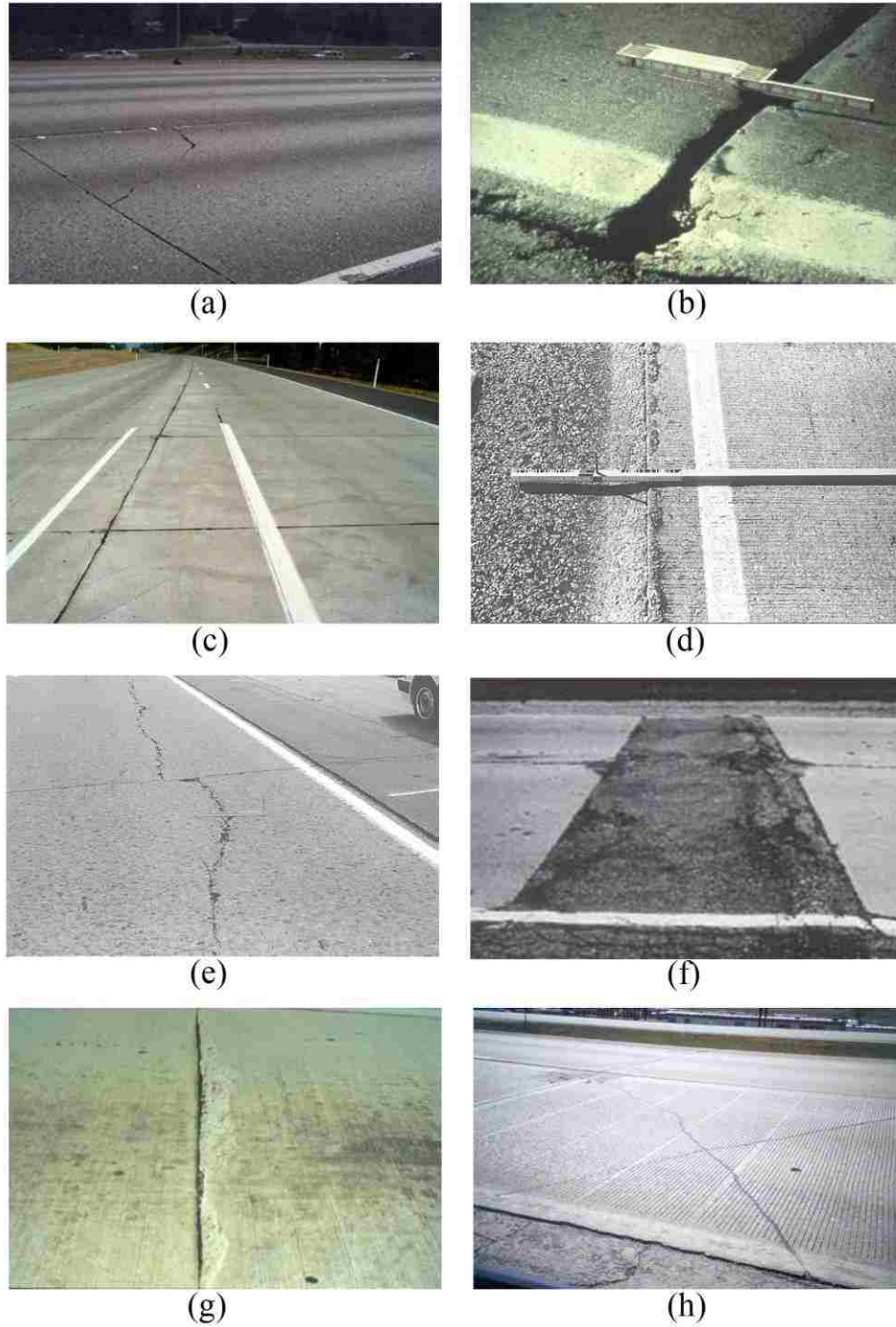


Figure 2. Illustration of rigid pavement surface distress; (a) corner break; (b) faulting of transverse joints and cracks; (c) joint seal damage; (d) lane/shoulder drop off; (e) longitudinal cracking; (f) patch deterioration; (g) spalling of joints and cracks; (h) transverse and diagonal cracks.

2.1.3 Pavement Surface Distress Evaluation Methods

Currently, two types of pavement surface distress evaluation methods have been operationally adopted by state and local transportation agencies, including manual evaluation (human observation and human analysis) and automated evaluation (machine observation and machine analysis). Transportation management agencies across the United States use one of these two aforementioned types of pavement surface distress evaluation methods. Each method has both advantages and disadvantages, which are discussed in details in the following section.

Both manual evaluation and automated evaluation methods are classified as ground-based evaluation method because the evaluation action occurs from the ground. Another method to evaluate pavement surface condition is through airborne observation, although it has not been used for any operational programs yet. In this research, this method is classified as aircraft-based evaluation method.

2.1.3.1 Manual Evaluation

Only a few state and local transportation agencies are still using manual methods to survey the surface distress of roadway pavement (Bandini et al. 2012). Using this method, surface distress data are collected by inspectors walking or driving along a section of pavement and rating the level of distress (Bogus et al., 2010). As shown in Figure 3, inspectors are walking along the shoulder while performing evaluation.

Using this method, surface distress data are primarily handwritten data and attached to archived images acquired by inspectors on the ground (boots on the ground). Manual evaluation methods can collect detailed information for various types of distresses, and it

is the reason that this method is still used. However, this method is expensive, extremely labor intensive, time-consuming, and data collected by different inspectors can exhibit a high degree of variability (Bogus et al. 2010). Manual evaluation is, therefore, sometimes unable to provide meaningful quantitative information, and eventually leads to inconsistencies in distress conditions over space and across evaluation (Cheng et al. 1999; Hudson and Uddin 1987; Wang and Li 1999; Wang 2000).



Figure 3. Illustration of manual evaluation walking along the shoulder.

In addition, manual evaluation relies on the subjective evaluation of distress type extent, and severity by a trained inspector based on visual observation (Hudson and Uddin 1987), which means the evaluation results are prone to subjective bias. Another problem with manual evaluation is that it is potentially dangerous to inspectors. Survey crews must walk along the side of the road to perform their evaluation and, despite safety precautions (e.g., safety training and high-visibility garments), are exposed to substantial risk of personal injury, especially in high traffic volume sections.

2.1.3.2 Automated Evaluation

In an attempt to address the shortcomings of manual evaluation, many transportation agencies have adopted automated technology to conduct surface distress surveys (Bandini et al. 2012). The automated methods typically include the use of vehicle-mounted devices (i.e., video cameras and electronic sensors) at a fine enough spatial resolution to detect individual distress measures (e.g., cracks) on the pavement surfaces. Figure 4 (roadex.org) shows a typical automated evaluation system adopted by state agencies.



Figure 4. Automatic pavement surface distress evaluation system.

The application of video camera based automated evaluation became common in the 1980s (Hudson and Uddin 1987). The development of automated pattern recognition techniques for quantifying surface distress from video film or image frame has led to much wider application of video and image processing technology in pavement surface distress evaluation (Hudson and Uddin 1987; Curphey et al. 1985; Haas et al. 1985). Video cameras, which are mounted to mobile platforms such as survey vans, are used to record video films or image frames of the pavement surface, while pattern recognition techniques are used to analyze the collected videos or images and extract pavement surface distress information.

For automated surveys based on video camera, most of the past and current research focuses on detecting and quantifying individual distresses in the pavement surfaces. For example, Mahler et al. (1991) demonstrated the feasibility of applying image processing techniques to the analysis of pavement surface cracking. Georgopoulos et al. (1995) developed a method which uses digital image processing techniques to provide suitable digital imagery as input for specialized software in order to determine objectively and automatically the type, the extent, and the severity of surface cracking for flexible pavements. Pynn et al. (1999) developed several image processing algorithms to automatically identify the cracking on pavement surfaces based on the video images collected with a survey van mounted video camera system. Lee and Kim (2005) developed a crack type index (CIT) that can be used in automated survey systems to determine the crack type objectively as longitudinal, transverse, and alligator cracking. Huang and Xu (2006) presented an image processing algorithm customized for high-speed, real-time inspection of pavement surface cracking.

Many researchers are still focusing on applying various image processing techniques to identify pavement surface cracks from images collected automated evaluation systems. Mustaffara et al. (2008) proposed a photogrammetric approach to automatically classify and quantify the pavement cracks. Ma (2008) proposed a method to detect pavement surface cracks based on a non-subsampled contourlet transform algorithm. Oliveira and Correia (2008) employed entropy and image dynamic thresholding techniques to automatically segment pavement surface cracks. Nguyen et al. (2009) proposed a method to automatically detect and classify defects on road pavement surface using anisotropy measure. Coudray et al. (2010) developed a multi-resolution

segmentation approach for the detection of pavement surface cracks. Chambon et al. (2010) proposed a method to extract pavement surface cracks with adapted filtering and markov model-based segmentation. Gavilan et al. (2011) presented a support vector machine (SVM) based classifier to distinguish different types of pavement surface cracks. Koch and Brilakis (2011) presented a method to detect pavement surface potholes based morphological thinning and elliptic regression. Adarkwa and Attoh-Okine (2013) proposed a tensor factorization method to detect classify pavement surface cracks.

The application of automated surveys based on electronic sensors also began to appear in the 1980s (Hudson and Uddin 1987). These various types of sensors are designed to assess either a specific type of distress such as transverse cracks or a specific type of pavement such as rigid pavement (Schnebele et al. 2015). Electronic sensors can perform seismic and dynamic testing, radar testing, sonic/ultrasonic testing, and laser testing. Seismic and dynamic sensors are applied for onsite pavement material characterization and structural evaluation (Uddin et al. 1987). Radar sensors, mostly used in the form of ground penetration radar (GPR), are suitable for measuring pavement layer thickness and identifying voids (Uddin et al. 1987; Maser 1996; Saarenketo and Scullion 2000). Forest and Utsi (2004) found GPR can also be used to identify cracks in flexible pavement and measure crack depths ranging from 50 mm to 160 mm. Sonic/ultrasonic sensors are applied to measure longitudinal roughness and rut depth (Uddin et al. 1987; Hudson et al. 1987). Laser sensors, mostly used in the format terrestrial laser scanning (TLS), are suitable for measuring longitudinal roughness, skid resistance, faulting of transverse joints, potholes, rutting and shoving, and transverse cracks and macro-texture

(Hudson et al. 1987; Chang et al. 2005; Yu et al. 2007; Li et al. 2010; Peng and Zhou 2011; Tsai et al. 2012).

Although automated evaluation methods can collect detailed information quickly and safely, and technological advances in computer hardware and imaging recognition have improved the performance of the automated evaluation methods, serious problems still remain in the areas of implementation costs, processing speed, and accuracy (Wang 2000). Automated methods require significant time to process data to extract useful information, since it requires very complicated analytical models and algorithms (Wang 2000). These methods require substantial technical expertise and are expensive to deploy, requiring specially trained operators on a regular basis.

It should be noted that most automated evaluation methods were developed first as semi-automatic systems to reach later automated ones (Gavilan et al. 2011). Semi-automated evaluation uses the aforementioned sensors to collect pavement surface images and perform the distress identification to an off-line process running in workstations with a substantial level of human intervention (Gavilan et al. 2011). The identification of various types of distress and their associated severity and extent from images requires well-trained inspectors on a regular basis. Therefore, a limited number of transportation management agencies are using semi-automated survey systems that are post-processing based which requires substantial human intervention; and its processing speed is about fraction of normal driving speed (Wang and Gong 2002).

In addition, data are collected on the ground as a single task and cannot be shared with other partner agencies to reduce the cost because a single image can only cover a small area which is usually less than five square meters (McGhee 2004). For example, the

Vermont Agency of Transportation (VAT) reported costs of up to \$170 USD per mile in urban areas for automated evaluation methods (McGhee 2004).

2.1.3.3 Aircraft-based Evaluation

Aircraft-based evaluation is characterized by deploying cameras on aircraft to evaluate pavement surface distress through airborne observation. Evaluating pavement surface distress through aircraft is not a new idea, but is also not used for operational evaluation of pavement surface distress yet. The application of an aerial photography-based evaluation method to pavement surface distress was first explored in the 1950s.

Several researchers (McMaster and Legault, 1952; Stoeckeler, 1968; Stoeckeler 1970) focused on visually comparing analog panchromatic aerial photographs to determine pavement surface distress. They concluded that untreated cracks and other high-contrast pavement defects (e.g., patching and bleeding) can be identified through the visual analysis. Although they concluded that visual analysis of panchromatic analog aerial photography is a practical means of conducting pavement conditions surveys, it is not used for operational pavement surface distress evaluation. This is because cracks are distinguishable only in large scale (e.g., 1:100) analog panchromatic aerial photographs and the associated cost is extremely high.

Along with the advances of geospatial technologies, high-spatial resolution digital aerial images can be routinely collected and provided to the public for free through governmental data repository such as United States Geological Survey (USGS) EarthExplorer. Recent advances in geospatial technologies, such as small-unmanned aircraft system (S-UAS) based hyper-spatial resolution imaging and automated aerial triangulation techniques, have enabled the collection of hyper-spatial resolution aerial

images at a low cost (Colomina and Molina 2014). These high-spatial and hyper-spatial resolution aerial images hold the potential to rapidly detect and assess pavement surface distress at a low cost because of its synoptic coverage (Jensen and Cowen 1999).

However, previous studies regarding the application of high-spatial or hyper-spatial resolution digital aerial images for pavement surface distress evaluation are very limited. To the author's knowledge, the only published research on this topic was performed by Chen et al. (2010). This research demonstrates the potential of using high-spatial resolution digital aerial images for assessing bridge deck pavement surface conditions, but not roadway pavement surface conditions. The lack of studies on this topic warrants further exploration and it is the motivation of this study.

2.2 Geospatial Technology (GT)

GT is commonly known as geomatics in the engineering field. GT refers to a system that is used to acquire, store, analyze, and visualize spatially referenced data (data that have a geographical or geospatial aspect) in two or three dimensions (Reed and Ritz 2004). It is a rapidly developing engineering discipline that focuses on using spatial information to support problem-solving (Gomasasca 2011).

GT interacts with a broad range of disciplines, including technical and manufacturing, surveying and mapping, computer science, information science, and other specialized areas of application. In 2004, GT was identified as a rapidly expanding industry that crosscuts nearly every discipline, every aspect of life, and every sector of the U.S. economy (Gewin 2004). Bednarz et al. (2006) contended that the ability to use GT intelligently and critically is becoming a requirement for citizens to effectively participate in today's modern society. Although GT's use is well-known and widespread

in the military and in homeland security, its influence is pervasive everywhere, even in areas with a lower public profile, such as land resources management, flood plain mapping, and environmental protection (Cimons 2011).

With the advances in hardware and software in the two decades, an increasingly wide range of geospatial tools, geospatial data and geospatial services have become available to a widening body of users (Van Manen et al. 2009; Nugent et al. 2010). Typically GT involves systems such as global navigation satellite systems (GNSS), geographic information systems (GIS), and remote sensing (RS).

GT has been successfully applied in many fields, including emergency management, wildlife management, crop monitoring, forest management, hydrology, landscape and landcover monitoring, public health management, disaster susceptibility assessment, and earth observation (Kushwaha and Roy 2003; Delgado et al. 2004; Williams et al. 2006; Li et al. 2009; Dar et al. 2011; Lebourgeois et al. 2010; Safaei et al. 2010; Imam 2011; Vu 2013).

2.2.1 Global Navigation Satellite Systems

The global navigation satellite systems (GNSS) are satellite-based technologies that provide precise location and time information in most weather condition, day or night, in most terrain condition where there is an unobstructed line of sight to four or more navigation satellites (Bolstad 2012). GNSS provides critical location information to military, civil, and commercial users around the world.

The first non-military applications of GNSS have been made for geodetic purposes with baseline measurements using differential methods (Breuer et al. 2002).

Since then, GNSS have become the most common method for coordinate data collection. As of 2016 there are two functioning GNSS, and two more are under development. The Navigation System with Time and Ranging Global Positioning System (NAVSTAR GPS) was the first deployed GNSS and is the most widely used system. NAVSTAR has been under development in the U.S. since 1973 and is operated by the U.S. Department of Defense (Bolstad 2012). There is also an operational Russian system named GLONAS. China and European Union are in the process of expanding their respective system Compass and Galileo into global system by 2020 (Bolstad 2012).

As the most widely used GNSS, GPS can represent all four systems in terms of application. GPS technology has been applied in many fields. The literature review of this section will focus on application of GPS in infrastructure management since the research topic of this study is roadway pavement surface distress evaluation which is a subtopic of infrastructure management.

GPS has been used for high-rise building (and other long-period civil structures) structural health monitoring and displacement monitoring (Celebi 2000; Breuer et al. 2002; Brownjohn 2007). Peyret et al. (2000) and Xu (2007) applied GPS in real-time construction equipment positioning to facilitate infrastructure construction process. Faghri and Hamad (2002) presented the application of GPS in collecting travel time, speed, and delay information of 64 major roads in the State of Delaware. Mintsis et al. (2004) presented a review of applying GPS in railroad planning, vehicle fleet management and monitoring, and transportation network mapping. Lu et al. (2008) applied GPS technology to build a mine-subsidence observation station to establish a reliable datum for displacement and deformation analysis. Janssen et al. (2011) applied

GPS in cadastral infrastructure management. Chen et al. (2012) used GPS in geospatial analysis of pavement evaluation and optimization of maintenance planning.

2.2.2 Geographic Information Systems

Geographic information systems (GIS) are computer-based systems to aid in the collection, maintenance, storage, analysis, output, and distribution of spatial data and information (Bolstad 2012). GIS have been developed since the early 1980s and were one of the fastest growing computer-based technologies of the 1990's (Bolstad 2005; Thakur 2012). In the last decade, uses of GIS have seen unprecedentedly growth, and have been used in a myriad of industries (e.g., construction and transportation) as analytical, managerial, and visualization tools (Migliaccio et al. 2015).

The most important feature of GIS is that it can create a database to store spatially referenced features. This means that in GIS, a data layer can contain not only the location of a feature, but also specific attributes (e.g., population) which are related to the location. This enables users to not quantitatively analyze the attributes of a location.

GIS has been widely and successfully used in almost every discipline since it is a ubiquitous tool (Bolstad 2012). Therefore, it is not possible to review all the literature. The literature review of this section (Section 2.2.2) is focused on the application of GIS in infrastructure management since the research topic of this study is roadway pavement surface distress evaluation which is a subtopic of infrastructure management.

In the 1990s, researchers have started considering the potential of using GIS in transportation planning and infrastructure asset management (Petzold and Freund 1990; Lemer 1998). Leipmik et al. (1993) used GIS for water resources planning and

management. Zhang et al. (1994) applied GIS in designing a common location reference system to efficiently management pavement and infrastructure in urban areas. Ashur and Crockett (1997) applied GIS to analyze cost data and improve cost estimate for infrastructure construction and management through the use of geographic management. Halfawy et al. (2002) and developed an integrated component-based framework that can enable the implementation of knowledge-intensive GIS-based infrastructure management system. They also discussed its application in sustainable infrastructure asset management (Halfawy et al. 2004). She et al. (1999) used GIS to develop a bridge management system to model bridge management agencies' business objectives, functions, and processes. Kulkarni and Miller (2003) discussed the key role of GIS in future pavement management systems. Li et al. (2013) used GIS in assessing environmental impact of construction project site. Zhang et al. (2014) used GIS to develop geographically based surface interpolation methods for adjusting construction cost estimates by project location.

2.2.3 Remote Sensing

Remote sensing (RS) is the acquisition of information about an object or phenomenon without making physical contact with the object (Schowengerdt 2006). In modern usage, RS generally refers to the use of remote sensors to detect, measure, and classify objects on Earth (i.e., surface, oceans, and atmosphere) thorough detecting and analyzing propagated signals (Zhang et al. 2015). These remote sensors can be on satellite or mounted to aircraft or even vehicles.

There are two main types of remote sensing: passive remote sensing and active remote sensing (Liu and Mason 2009). Passive sensors can detect natural radiation that is

emitted or reflected by the object or surrounding areas (Schott 2007). Reflected sunlight is the most common source of radiation measured by passive sensors. Examples of passive sensors include analog cameras, digital cameras, and spectrometers. Active sensors, on the contrary, emit energy to scan objects and areas whereupon a sensor then detects and measures the radiation that is reflected or backscattered from the target. Radio detection and ranging (RADAR) and light detection and ranging (LiDAR) are examples of active sensors where the time delay between emission and return is measured, establishing the location, speed and direction of an object (Liu and Mason 2009).

Two common data formats for passive sensors are aerial photography and satellite imagery. Aerial photography is the collecting of ground photographs from an elevated position (Jensen 2007). An elevated position indicates the photographs are collected above the ground (in the air) but not from a ground-based structure (e.g., power pole). Cameras may be hand held or mounted, and photographs may be taken by a photographer, triggered remotely or triggered automatically (Graham and Roger 1987). Platforms for collecting aerial photography include manned aircraft (both fixed-wing and helicopters), unmanned aircraft systems (UAS), balloons or kites, blimps and dirigibles, rockets, parachutes, stand-alone telescoping, and vehicle mounted poles (Jensen 2007). Satellite imagery consists of imagery of Earth or other planets made by means of artificial satellites. Aerial photography and satellite images have many applications in meteorology, agriculture, geology, forestry, landscape, biodiversity conservation, regional planning, education, intelligence and warfare. Images can be in visible colors and in multispectral or hyperspectral (Li et al. 2009).

Remote sensing has been successfully applied in many fields. The literature review of this section (Section 2.2.3) is focused on application of remote sensing in infrastructure management since the research topic of this study is roadway pavement surface distress evaluation which is a subtopic of infrastructure management.

Some researchers discussed the potential of using imaging spectrometers and hyperspectral imaging to map pavement age and condition (Usher and Truax 2001; Gomez 2002; Herold et al. 2004). Some researcher explored the utility of SAR imagery (either airborne or spaceborne) for detecting damaged building due to earthquakes (Matsuoka and Yamazaki 2004; Chini et al. 2009; Balz and Liao 2010). Turker and Cetinkaya (2005) proposed a method to automatically detect the earthquake-damaged buildings through the use of digital elevation models (DEMs) created from pre- and post-earthquake stereo panchromatic aerial photographs. Herold and Roberts (2005) applied remote sensing techniques to study the spectral characteristics of asphalt road aging and deterioration based on aerial photographs. Yamazaki et al. (2005) proposed a method of detecting earthquake-induced collapsed buildings by visually observing the satellite images from QuickBird. Rehor and Bahr (2007) developed a method to detect building damages caused by earthquakes through the use of LiDAR data. Samadzadegan and Rastiveisi (2008) established an approach to automatically detect and classify the damaged buildings caused by earthquakes by using high resolution satellite imagery and vector data. Rezaeian and Gruen (2011) presented an innovative approach based on Bayesian networks to automatically extract the 3D buildings using aerial and space images. With this proposed method, the height change of the buildings can be detected which can be used for macro-seismic damage assessment in urban areas.

2.3 Gaps in Knowledge

As mentioned in the previous section, GT is the ideal tool to effectively collect and analyze pavement surface distress data since roadway infrastructure is fundamentally spatial (roadways are spatially and extensively distributed). Literature review revealed that three prevalent GT, including HiSR-DAP acquired by high-spatial resolution aerial imaging technique, HySR-DAP acquired by S-UAS based hyper-spatial resolution imaging technique, and geospatial modeling technique, hold the potential to evaluate pavement surface distress conditions.

However, based on the review of literature, the use of these three GT for pavement surface distress condition assessment is lacking and presents a significance gap in the research. Specifically, previous studies regarding the application of HiSR-DAP for pavement surface distress evaluation are very limited. To the author's knowledge, the only published research on this topic was performed by Chen et al. (2010); they investigated the potential of using HiSR-DAP for assessing bridge deck (not roadway) pavement surface conditions by visually analyzing the digitized distresses, which is labor-intensive and time-consuming. Previous studies on the application of HySR-DAP and geospatial modeling technique for pavement surface distress evaluation are completely lacking. To the author's knowledge, there is no published research on this topic. The lack of studies on this topic warrants further in-depth exploration.

The primary scope of this research is to evaluate the potential of the three aforementioned GT to improve the efficiency of pavement surface distress evaluation, including empirical analysis HiSR-DAP and HySR-DAP, and inferential geospatial modeling based on traffic volume, environmental conditions, and topographic factors.

Chapter 3 Extracting Pavement Surface Distress Conditions Based on High-Spatial Resolution Natural Color Digital Aerial Photography (HiSR-DAP)

3.1 Introduction

Pavement surface distress information is essential to pavement management. Pavement management activities and decisions at all levels (i.e., federal, state, and local) are supported by pavement surface condition information of varying detail (Haas et al., 1994). Pavement surface distress evaluation can lead to not only effective allocation of limited resources for timely maintenance and repair (Haas et al. 1994; Hudson and Uddin 1987), but also measurement of the effectiveness of various maintenance techniques and repair methods (Hudson et al. 1987; Hudson and Uddin 1987).

Currently, most transportation agencies use either manual evaluation or automated evaluation to collect data solely for the purpose of pavement surface distress evaluation at significant expense (McGhee 2004). This study therefore explores the utility of routinely-acquired and publically-available high-spatial resolution visible range digital aerial photography (HiSR-DAP) to supplement or replace dedicated surveys of pavement surface condition. Many counties and municipalities routinely acquire HiSR-DAP and most make these images freely available to the public. These photos cover all ground features including roadways, meaning they contain information that may permit discrimination of pavement surface distress. Modern aerial photographs are in digital format, which means they can be readily shared with partner agencies and analyzed to produce standardized results through image processing techniques. The availability of

these images offers the potential of using routinely-collected and publically-available data for standardized evaluation of pavement surface distress, reducing the evaluation cost and time while improving the comparability of results.

There are many programs to routinely collect HiSR-DAP. For example, with the support of the National Agricultural Imagery Program (NAIP), the U.S. Geological Survey (USGS) and the U.S. Department of Agriculture (USDA) regularly acquire digital color-infrared, ortho-corrected aerial photography which covers all states at 1 m spatial resolution, and they provide the data to the public for free. Many counties and cities now routinely acquire natural color 6-inch (0.1524 m) and even 3-inch (0.0762 m) spatial resolution, ortho-corrected aerial photos. In addition, some states have initiated the program to regularly acquire statewide aerial photos. For example, the State of Missouri images the entire state regularly with 2 ft (0.6096 m) spatial resolution multispectral digital aerial photographs (Wright 2014). It would not be hard to imagine more states to moving to do so because the uses for these data continue to expand.

Past and current research for pavement surface distress evaluation has focused on the detection of individual distresses (*e.g.*, an individual crack). This information is commonly aggregated to determine the overall level of pavement surface distress, which is then used by transportation agencies for planning and maintenance purposes. As to aircraft-based pavement surface distress evaluation, cracks are only distinguishable in large-scale (*e.g.* 1: 100) aerial photographs (Stoeckeler 1970). A key limitation of the routinely collected and publicly available HiSR-DAP is that its spatial resolution is too coarse to enable the detection and quantification of individual distresses. As a result, this research does not focus on assessing individual distresses, but rather, on estimating the

overall condition by analyzing the brightness and variation of resolution cells. Specifically, the research presented here is focused on analyzing HiSR-DAP to determine overall pavement surface distress rates through pixel-based spectral response assuming an L-resolution scene model (Strahler et al. 1986).

This research explores the utility of routinely-acquired and publically-available HiSR-DAP for the evaluation of overall pavement surface distress. Specifically, the intent of this study is to examine how well overall pavement surface distress can be estimated from HiSR-DAP. Principal components analysis (PCA) and linear least squares regression models were used to evaluate the potential of using HiSR-DAP to infer pavement surface distress.

3.2 Methodology

PCA and multiple linear least square regression models were used to model the relationship between the dependent variable of overall distress rate (ODR) and explanatory variables extracted from the spectral response of the HSR multispectral digital aerial photography. The ultimate goal is to be able to predict the ODR for roadway segments for which ODR ground reference values are unavailable.

3.2.1 Data Acquisition and Preparation

The study area for this research encompasses six counties in northern New Mexico, including Bernalillo, Cibola, Sandoval, Santa Fe, Torrance, and Valencia. These counties are located around the City of Albuquerque and are covered by all of the existing high-spatial resolution (HiSR) multispectral digital aerial photographs with various spatial resolutions obtained from 2004 to 2012. Within the study area, 50 data collections sites

were identified for use in this study. Each data collection site covers the rightmost lane with a length of one tenth of a mile. These sites were selected because they belong to a set of pavement sections regularly evaluated as part of the New Mexico Department of Transportation (NMDOT) pavement evaluation program.

The road segments of these 50 study sites were visually evaluated in reference to the available HiSR natural color digital aerial photographs to ensure they were covered by aerial photographs and there are no large obstacles (e.g. bridges and overpasses) above them. A geographic information system (GIS) database provides the roadway number, milepost number, and direction for each study site.

Reference pavement surface condition data for the study sites were acquired from records of manual pavement evaluations conducted for NMDOT during the summer of 2009 (Cordova et al. 2009). All of the study sites were constrained to flexible, asphalt concrete (AC) pavements. For flexible pavements, when not including rutting and showing distresses, the NMDOT evaluates severity and extent of the following seven distresses on a scale of 0 – 3 (0=Not Present, 1=Low, 2=Medium, and 3=High): 1) Raveling & Weathering; 2) Bleeding; 3) Longitudinal Cracking; 4) Transverse Cracking; 5) Alligator Cracking; 6) Edge Cracking; and 7) Patching. It should be noted that the listed distresses are all horizontal distress, and they do not reflect distresses in elevation such as rutting and shoving. This makes the use of HiSR natural digital aerial photographs to detect pavement surface overall distress rate (ODR) possible since elevation information cannot be found in a typical aerial photograph (the exception being stereoscopic aerial photographs).

Each study site's ODR can be calculated based on the following equation:

$$ODR = \sum_{i=1}^7(\alpha_i \times \beta_i \times \gamma_i) \quad (1)$$

Where i represents each of the seven distresses, α denotes the severity rating, β denotes the extent rating, and γ denotes the weighting factor. The weighting factors for the distresses have been provided by NMDOT and are 3, 2, 12, 12, 25, 3, and 2, respectively, for each of the seven distresses. The calculated ODR for each of the 50 study sites ranges from 0 to 477. The lower the ODR value, the better the pavement surface condition. The maximum possible value is 504, while the minimum possible value is 0. ODR can be easily converted to Present Serviceability Index (PSI), which is broadly used by various transportation agencies (Bandini et al. 2012). Different agencies can develop and establish their own models to infer the overall pavement surface conditions, no matter what particular metric they are using.

One set of archived and readily available ortho-corrected HiSR natural color digital aerial photographs with a spatial resolution of 6-inch (0.1524 m) were obtained from the Earth Data Analysis Center (EDAC) at the University of New Mexico. The aerial photographs are natural color digital aerial photography that records energy in the region from 0.4 μm to 0.7 μm and they have three spectral bands which include visible blue (0.4 to 0.5 μm), visible green (0.5 to 0.6 μm) and visible red (0.6 to 0.7 μm) (Jensen 2007). These images are in 8-bit data format and are the actual digital numbers recorded. In addition, these aerial photographs are routinely (every the other year) collected with the Zeiss/Intergraph Digital Mapping Camera (DMC) System by the Mid-Region Council of Governments (MRCOG) contracted to Bohannon-Huston, Inc.

The aerial photographs were taken in March-April 2010 and were matched with the manually-collected pavement condition data collected in May-August 2009. This was

the closest time match between the aerial photographs and the pavement condition data available. According to the Federal Highway Administration (FHWA), it is approximately a 15-year process for pavement surface condition to drop 50% in quality (Lenz 2011). Because the time elapsed between the pavement condition data collection and aerial photographs collection was less than a year (approximately 6 months), the assumption is that no significant change occurred at the study site.

3.2.2 Image Processing

3.2.2.1 Image Aggregation

Data on actual pavement surface distress conditions were collected on short sections (0.1-mile [161-m]) of pavement located at specific mileposts. In order to identify the evaluation zone of each study site on the aerial photographs, a buffer of 0.1-mile was created around each individual study site's milepost in the aerial photographs. After creating the buffers, the evaluation zone of several study sites could not be completely covered by a single 6-inch image, because the aerial photographs were divided into tiles to reduce the storage size. In this case, two or more photographs were needed. When multiple photographs were used for a single milepost, it was necessary to create a mosaic of the aerial photographs. These images were mosaicked based on standard overlay-based algorithm and average blending mode.

3.2.2.2 Evaluation Polygon Creation

Pavement surface distress conditions are only evaluated within a portion of the roadway. According to the protocol for manual evaluation employed by NMDOT (Cordova et al., 2009), pavement surface distress data were collected only in the rightmost driving lane

and never in passing lanes, turning lanes, or on the shoulder. For two-lane roadways (one driving lane in each direction), data were collected only in the positive direction (north and/or east) from a given milepost to a distance of 0.1-mile. For multi-lane roadways (two or more driving lanes in each direction), data were collected in both the positive and negative directions (north-south and/or east-west) at a given milepost. In the positive direction the pavement evaluation was conducted from a given milepost to a distance of 0.1-mile, while in the negative direction the evaluation was conducted from 0.1-mile prior to the given milepost. This ensured that the pavement sections evaluated at the given milepost were parallel and aligned to each other (Appendix E).

To ensure alignment between the data collection zones, polygons were created to represent the highway zones used in manual evaluation, and from here on referred to as “evaluation polygons”. These evaluation polygons were created by heads up digitizing over the 6-inch aerial photographs following the protocol mentioned above. It should be noted that these manually created polygons only cover the pavement surface and the polygon creation process does not involve any removal of the non-road surface elements (e.g., vegetation). Therefore, there is no classification involved in the analysis. In addition, there are thousands of pixel cells in each evaluation polygon and therefore, results are not likely sensitive to omission or commission errors of one or several pixels during the digitizing of evaluation polygons.

When creating the evaluation polygons, six types of features on the ground were excluded since they are considered to be noise. These features are center lines, solid white shoulder stripes, other pavement markings, overpasses, power pole shadows, and vehicles. Figure 5 illustrates the excluded features mentioned above.

3.2.2.3 Image Degradation

Most counties and municipalities routinely collect HSR multispectral digital aerial photography. The spatial resolution of most of these images is between 6-inch and 1 m (40 in). In order to examine how well overall pavement surface distress can be estimated from routinely collected HSR multispectral digital aerial photography, the set of 6-inch aerial photography was degraded to 12-inch (0.3048 m) and 24-inch (0.6096 m) aerial photography. This set of 6-inch aerial photography was not degraded to 1 m because previous research completed by Zhang and Bogus (2014) showed that 1 m natural color digital aerial photography lacks the spatial resolution to detect overall pavement distress conditions effectively.

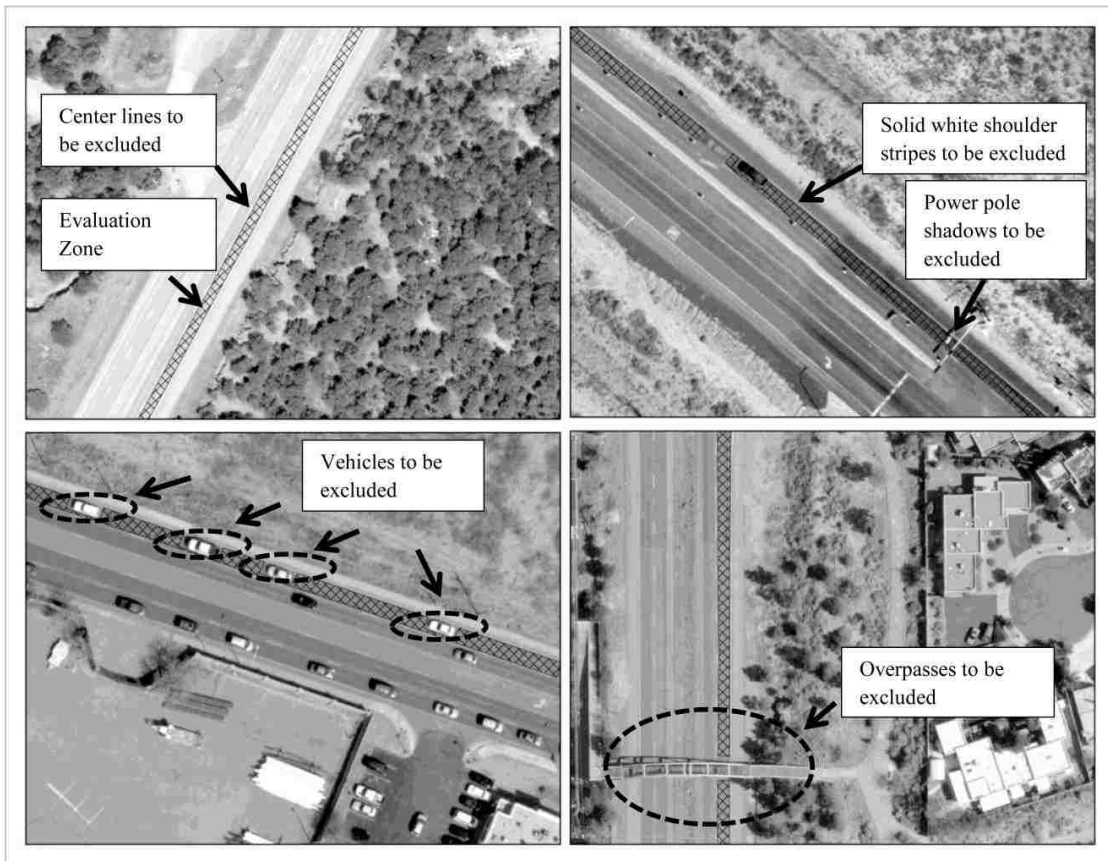


Figure 5. Exclusion of unwanted features on the images.

3.2.2.4 Spectral Response Extraction

Only the data within the evaluation polygons are comparable to known ODR rates. Once evaluation polygons were digitized to correspond to the collected reference or actual ODR data, statistics (e.g. mean, median, standard deviation, variety, majority, minority, maximum, minimum, range, and sum) summarizing the pixel values contained within those evaluation polygons were extracted for each resolution.

3.2.3 Multiple Linear Least Squares Regression Analysis

3.2.3.1 Variables

The dependent variable, or response variable, used in this study is the ODR described in the previous section. ODR was calculated for the field pavement surface distress data collected through manual inspection.

Selecting the most appropriate independent variables from the statistics mentioned in the previous section is necessary for building the regression model. According to Herold (2007), the mean value of the spectral response of the visible wavelengths has a significant negative relationship with ODR. The higher the mean brightness is (higher mean brightness value), the better the pavement surface condition is (lower ODR value). Pavement surface distresses (e.g., cracks) expose deeper layers of the pavement with higher contents of the original asphalt mix, which is then manifested in increased hydrocarbon absorptions features (Herold 2007). Therefore, degraded pavement surfaces cause less reflectance with increasing hydrocarbon features, while less degraded pavement surfaces get brighter with decreasing hydrocarbon features. Also, shadows induced by cracks decrease brightness.

In this research context, image texture, which is a first order derivative measure of variation in brightness values, may also be a significant variable. Theoretically, the worse the pavement surface condition is, the more heterogeneity of brightness values should be exhibited, due to the introduction of shadows associated with cracks and deformations and exposure of pavement aggregate (i.e., gravels). For example, a very good condition pavement section may have a standard deviation value of 4, while a poor one may have standard deviation value of 100. Pearson's correlation analyses were performed on a variety of texture measures and it revealed that other texture measures including range and variety have a strong correlation with standard deviation and therefore, only standard deviation was selected as the texture measure. Table 1 shows the Pearson's correlation results.

For each image dataset, (6-inch, 12-inch, and 24-inch digital aerial photographs), mean and standard deviation values of each band (visible blue, visible green, and visible red) were selected as independent variables, resulting in a total of six variables. Pearson's correlation analyses were performed to examine if there is correlation among these six variables. The results in Table 2 show that in each dataset these six variables have significant correlation with ODR. However, there is also significant correlation among these six variables, which violates the assumption of variable independence by linear least squares regression.

PCA was used on mean and standard deviation values of each band of the three datasets to eliminate the correlation among the six variables (Pearson 1901). These principal components were used as independent variables for the various linear regression

models described below. Table 3 shows the resultant loadings for each principal component obtained from the PCA.

Table 1. Pearson Correlation Results of Texture Measurement of the 6-Inch, 12-Inch, and 24-Inch Natural Color Digital Aerial Photography

Dataset	Variables	R1	STD1	V1	R2	STD2	V2	R3	STD3	V3
6-inch	R1	1.0000								
	STD1	0.8738	1.0000							
	V1	0.9790	0.9222	1.0000						
	R2	0.9952	0.8809	0.9816	1.0000					
	STD2	0.8746	0.9977	0.9234	0.8823	1.0000				
	V2	0.9729	0.9267	0.9969	0.9805	0.9300	1.0000			
	R3	0.9869	0.8491	0.9720	0.9876	0.8536	0.9691	1.0000		
	STD3	0.8877	0.9888	0.9362	0.8954	0.9926	0.9417	0.8784	1.0000	
V3	0.9669	0.8938	0.9884	0.9711	0.8999	0.9891	0.9795	0.9247	1.0000	
12-inch	R1	1.0000								
	STD1	0.7680	1.0000							
	V1	0.9001	0.9403	1.0000						
	R2	0.9949	0.7697	0.9007	1.0000					
	STD2	0.7676	0.9972	0.9411	0.7733	1.0000				
	V2	0.8995	0.9342	0.9961	0.9061	0.9395	1.0000			
	R3	0.9814	0.7474	0.8900	0.9898	0.7541	0.8971	1.0000		
	STD3	0.7709	0.9874	0.9466	0.7783	0.9919	0.9450	0.7720	1.0000	
V3	0.8831	0.9117	0.9861	0.8924	0.9197	0.9901	0.8998	0.9400	1.0000	
24-inch	R1	1.0000								
	STD1	0.8041	1.0000							
	V1	0.8915	0.9559	1.0000						
	R2	0.9956	0.7996	0.8826	1.0000					
	STD2	0.8034	0.9962	0.9514	0.8043	1.0000				
	V2	0.8857	0.9518	0.9930	0.8837	0.9535	1.0000			
	R3	0.9742	0.7631	0.8535	0.9845	0.7744	0.8585	1.0000		
	STD3	0.7977	0.9830	0.9451	0.8017	0.9906	0.9495	0.7900	1.0000	
V3	0.8695	0.9302	0.9780	0.8722	0.9368	0.9843	0.8731	0.9518	1.0000	

Note: 1 indicates the visible red band; 2 indicates the visible green band; 3 indicates the visible blue band; R indicates range, STD indicates standard deviation, and V indicates variety.

Table 2. Pearson Correlation Results of the Mean Value and Standard Deviation Value of the 6-Inch, 12-Inch, and 24-Inch Natural Color Digital Aerial Photography

Dataset	Variables	ODR	M1	STD1	M2	STD2	M3	STD3
6-inch	ODR	1.0000						
	M1	-0.9586	1.0000					
	STD1	0.9043	-0.8938	1.0000				
	M2	-0.9512	0.9958	-0.8781	1.0000			
	STD2	0.9075	-0.9016	0.9987	-0.8871	1.0000		
	M3	-0.9333	0.9859	-0.8456	0.9922	-0.8565	1.0000	
	STD3	0.9263	-0.9148	0.9926	-0.9020	0.9953	-0.8764	1.0000
12-inch	ODR	1.0000						
	M1	-0.7337	1.0000					
	STD1	0.8245	-0.6640	1.0000				
	M2	-0.6993	0.9904	-0.6423	1.0000			
	STD2	0.8243	-0.6766	0.9977	-0.6575	1.0000		
	M3	-0.6832	0.9699	-0.6192	0.9881	-0.6390	1.0000	
	STD3	0.8379	-0.6665	0.9892	-0.6518	0.9935	-0.6420	1.0000
24-inch	ODR	1.0000						
	M1	-0.7246	1.0000					
	STD1	0.5457	-0.5072	1.0000				
	M2	-0.7220	0.9863	-0.4397	1.0000			
	STD2	0.5718	-0.5323	0.9977	-0.4669	1.0000		
	M3	-0.7030	0.9455	-0.3497	0.9833	-0.3793	1.0000	
	STD3	0.6022	-0.5236	0.9868	-0.4550	0.9923	-0.3657	1.0000

Note: 1 indicates the visible red band; 2 indicates the visible green band; 3 indicates the visible blue band; M indicates mean; STD indicates standard deviation; and ODR indicates overall distress rate.

Table 3. PCA Loadings of the Three Sets of Natural Color Digital Aerial Photography

Datasets	Input Features	PC	M1	STD1	M2	STD2	M3	STD3	Proportion
6-inch	M1, STD1, M2, STD2, M3, STD3	PC_{A1}	-0.4121	0.4061	-0.4094	0.4083	-0.4022	0.4113	0.9399
		PC_{A2}	0.3313	0.4472	0.3926	0.4162	0.4914	0.3485	0.0568
		PC_{A3}	0.5719	-0.2041	0.2226	-0.0448	-0.6363	0.4182	0.0019
		PC_{A4}	-0.3650	-0.4431	0.0641	-0.2602	0.3184	0.7052	0.0008
		PC_{A5}	0.5072	-0.1174	-0.7890	0.0057	0.3005	0.1269	0.0005
		PC_{A6}	-0.0545	-0.6191	0.0455	0.7684	0.0160	-0.1451	0.0002
	M3, STD3	PC_{B1}	N/A	N/A	N/A	N/A	-0.7071	0.7071	0.9382
		PC_{B2}	N/A	N/A	N/A	N/A	0.7071	0.7071	0.0618
	M2, STD2	PC_{G1}	N/A	N/A	-0.7071	0.7071	N/A	N/A	0.9435
		PC_{G2}	N/A	N/A	0.7071	0.7071	N/A	N/A	0.0565
	M1, STD1	PC_{R1}	-0.7071	0.7071	N/A	N/A	N/A	N/A	0.9469
		PC_{R2}	0.7071	0.7071	N/A	N/A	N/A	N/A	0.0531
	M1, M2, M3	PC_{S1}	0.5772	N/A	0.5784	N/A	0.5319	N/A	0.9942
		PC_{S2}	-0.6196	N/A	-0.1496	N/A	0.7705	N/A	0.0048
		PC_{S3}	0.5319	N/A	-0.8019	N/A	0.2721	N/A	0.0010
	STD1, STD2, STD3	PC_{T1}	N/A	0.5774	N/A	0.5779	N/A	0.5767	0.9970
		PC_{T2}	N/A	-0.5557	N/A	-0.2393	N/A	0.7962	0.0027
		PC_{T3}	N/A	0.5981	N/A	-0.7802	N/A	0.1830	0.0003
12-inch	M1, STD1, M2, STD2, M3, STD3	PC_{A1}	-0.4112	0.4071	-0.4081	0.4114	-0.4021	0.4096	0.8216
		PC_{A2}	0.3849	0.4181	0.4149	0.4005	0.4278	0.4018	0.1707
		PC_{A3}	0.6219	-0.2356	0.0703	-0.0560	-0.6608	0.3361	0.0056
		PC_{A4}	0.4253	0.4615	-0.2630	0.2295	-0.1566	-0.6780	0.0012
		PC_{A5}	0.3392	-0.1144	-0.7630	-0.1575	0.4333	0.2776	0.0006
		PC_{A6}	0.0073	-0.6147	-0.0705	0.7679	0.0797	-0.1449	0.0002
	M3, STD3	PC_{B1}	N/A	N/A	N/A	N/A	-0.7071	0.7071	0.8287
		PC_{B2}	N/A	N/A	N/A	N/A	0.7071	0.7071	0.1713
	M2, STD2	PC_{G1}	N/A	N/A	-0.7071	0.7071	N/A	N/A	0.8210
		PC_{G2}	N/A	N/A	0.7071	0.7071	N/A	N/A	0.1790
	M1, STD1	PC_{R1}	-0.7071	0.7071	N/A	N/A	N/A	N/A	0.8320
		PC_{R2}	0.7071	0.7071	N/A	N/A	N/A	N/A	0.1680
	M1, M2, M3	PC_{S1}	0.5763	N/A	0.5759	N/A	0.5799	N/A	0.9885
		PC_{S2}	-0.6850	N/A	0.7273	N/A	-0.0415	N/A	0.0101
		PC_{S3}	0.4457	N/A	0.3733	N/A	-0.8137	N/A	0.0014
	STD1, STD2, STD3	PC_{T1}	N/A	0.5573	N/A	-0.5776	N/A	0.5771	0.9956
		PC_{T2}	N/A	0.5765	N/A	0.7889	N/A	0.2128	0.0038
		PC_{T3}	N/A	0.5782	N/A	-0.2098	N/A	-0.7885	0.0005
24-inch	M1, STD1, M2, STD2, M3, STD3	PC_{A1}	-0.4248	0.4077	-0.4088	0.4159	-0.3792	0.4117	0.7181
		PC_{A2}	0.3518	0.4129	0.4127	0.3934	0.4701	0.3995	0.2726
		PC_{A3}	0.7108	0.0589	0.0464	0.0942	-0.6929	-0.0122	0.0065
		PC_{A4}	0.0234	-0.5681	0.0526	-0.2084	-0.0630	0.7916	0.0023
		PC_{A5}	0.4357	0.0142	-0.8087	-0.0758	0.3827	0.0615	0.0003
		PC_{A6}	0.0118	-0.5804	-0.0601	0.7837	0.0687	-0.2011	0.0002
	M3, STD3	PC_{B1}	N/A	N/A	N/A	N/A	-0.7071	0.7071	0.7536
		PC_{B2}	N/A	N/A	N/A	N/A	0.7071	0.7071	0.2464
	M2, STD2	PC_{G1}	N/A	N/A	-0.7071	0.7071	N/A	N/A	0.7334
		PC_{G2}	N/A	N/A	0.7071	0.7071	N/A	N/A	0.2666
	M1, STD1	PC_{R1}	-0.7071	0.7071	N/A	N/A	N/A	N/A	0.6829
		PC_{R2}	0.7071	0.7071	N/A	N/A	N/A	N/A	0.3171
	M1, M2, M3	PC_{S1}	0.5745	N/A	0.5825	N/A	0.5751	N/A	0.9812
		PC_{S2}	0.7206	N/A	-0.0266	N/A	-0.6929	N/A	0.0182
		PC_{S3}	0.3883	N/A	-0.8124	N/A	0.4350	N/A	0.0007
	STD1, STD2, STD3	PC_{T1}	N/A	0.5763	N/A	0.5784	N/A	0.5773	0.9949
		PC_{T2}	N/A	0.7890	N/A	-0.2098	N/A	-0.5774	0.0047
		PC_{T3}	N/A	0.2129	N/A	-0.7883	N/A	0.5773	0.0005

Note: PC indicates principal components; $PC_{A1} - PC_{A6}$ indicate the six principal components extracted from the mean and standard deviation values of each of the three visible bands; $PC_{B1} - PC_{B2}$ indicate the two principal components extracted from the mean and standard deviation values of the visible blue band; $PC_{G1} - PC_{G2}$ indicate the two principal components extracted from the mean and standard deviation values of the visible green band; $PC_{R1} - PC_{R2}$ indicate the two principal components extracted from the mean and standard deviation values of the visible red band; $PC_{S1} - PC_{S3}$ indicate the three principal components extracted from the mean values of each of the three visible bands; and $PC_{T1} - PC_{T3}$ indicate the three principal components extracted from the standard deviation value of each of the three visible bands.

3.2.3.2 Linear Regression

Various multiple linear least squares regression models were built based on reference pavement surface ODR data and the principal components extracted from the 6-inch, 12-inch, and 24-inch multispectral digital aerial photographs. The ultimate goal is the identification of the regression model with the highest correlation to predict pavement surface ODR values.

The regression model that uses six principal components obtained from all three visible bands, Model 1 in Table 4, can be expressed as the following (Equation 2):

$$ODR = \beta_0 + \beta_1 PC_{A1} + \beta_2 PC_{A2} + \beta_3 PC_{A3} + \beta_4 PC_{A4} + \beta_5 PC_{A5} + \beta_6 PC_{A6} \quad (2)$$

Where β_0 represents the intercept parameter, PC_{A1} to PC_{A6} represent the six principal components derived from mean and standard deviation of each band, and β_1 to β_6 represent the corresponding coefficients.

As shown in Table 3, PC_{A1} and PC_{A2} collectively contain more than 99% of the information contained in the aerial imagery. In order to test the significance of the rest principal components (PC_{A3} to PC_{A6}), the first two principal components (PC_{A1} and PC_{A2}) were considered as a break point and PC_{A3} to PC_{A6} were removed from the linear regression, resulting in Model 2 (or Equation 3):

$$ODR = \beta_0 + \beta_1 PC_{A1} + \beta_2 PC_{A2} \quad (3)$$

To analyze which spectral band (visible blue, visible green, and visible red) contributes more or is more significant to the prediction of ODR, three linear regression models were created (Models 3 to 5, or Equations 4 to 6) and they are:

$$ODR = \beta_{B0} + \beta_{B1} PC_{B1} + \beta_{B2} PC_{B2} \quad (4)$$

$$ODR = \beta_{G0} + \beta_{G1} PC_{G1} + \beta_{G2} PC_{G2} \quad (5)$$

$$ODR = \beta_{R0} + \beta_{R1}PC_{R1} + \beta_{R2}PC_{R2} \quad (6)$$

PC_{B1} to PC_{B2} , PC_{G1} to PC_{G2} , and PC_{R1} to PC_{R2} represent the two principal components extracted from the mean values and standard deviation values of the visible blue band, visible green band, and visible red band, respectively. β_{B1} to β_{B2} , β_{G1} to β_{G2} , and β_{R1} to β_{R2} represent the corresponding coefficients. β_{B0} , β_{G0} , and β_{R0} represent the corresponding intercept parameters.

Models 6 and 7 (or Equations 7 to 8) analyze which feature combination (i.e. spectral features [mean values] vs. texture features [standard deviation values]) contributes more to the ODR prediction capability, and these two models are:

$$ODR = \beta_{S0} + \beta_{S1}PC_{S1} + \beta_{S2}PC_{S2} + \beta_{S3}PC_{S3} \quad (7)$$

$$ODR = \beta_{T0} + \beta_{T1}PC_{T1} + \beta_{T2}PC_{T2} + \beta_{T3}PC_{T3} \quad (8)$$

PC_{S1} to PC_{S3} indicate the three principal components derived from the mean values of each of the three visible bands, and β_{S1} to β_{S3} represent corresponding coefficients. PC_{T1} to PC_{T3} indicate the three principal components extracted from the standard deviation value of each of the three visible bands, and β_{T1} to β_{T3} represent corresponding coefficients. β_{S0} and β_{T0} represent the intercept parameters.

3.2.3.3 Validation

In order to test the validity and robustness of the method for predicting ODR operationally, we held out 25 of the sites from the identified regression model with the highest certainty described in the previous section. Among the 50 study sites, 25 of them were selected using a random sample stratified by distress rate and used to develop the regression models while the other 25 were used to validate the predicted ODR values by root mean squared error (RMSE), mean absolute error, and standard error.

3.3 Results and Discussion

Table 4 shows the linear regression results using all six principal components (PC_{A1} to PC_{A6}) and by using only two principal components (PC_{A1} and PC_{A2}). It revealed that removing PC_{A3} to PC_{A6} decreased the R-squared value and increased the RMSE for all three datasets. It proved that PC_{A3} to PC_{A6} are useful components despite containing less than 1% of the original information. This suggests that all six principal components should be used for operational inference of ODR.

Table 4. Model Fit for Prediction of ODR Values

Dataset (Size: 50)	Model #	Var.	Coef.	Standard Error	p-value	R ²	Adjusted R ²	RMSE	Prob > F	
6-inch	Model 1	PC_{A1}	41.08	1.45	<0.0001*	0.9507	0.9439	24.087	<0.0001*	
		PC_{A2}	-13.32	5.89	0.029*					
		PC_{A3}	-35.14	32.42	0.284					
		PC_{A4}	167.81	48.97	0.001*					
		PC_{A5}	15.06	64.32	0.816					
		PC_{A6}	-319.63	112.31	0.007*					
		Intercept	135.36	3.41	<0.0001*					
	Model 2	PC_{A1}	41.08	1.69	<0.0001*	0.9266	0.9235	28.123	<0.0001*	
		PC_{A2}	-13.32	6.88	0.059					
		Intercept	135.36	3.98	<0.0001*					
	12-inch	Model 1	PC_{A1}	38.68	2.95	<0.0001*	0.8208	0.7958	45.843	<0.0001*
			PC_{A2}	14.54	6.47	0.030*				
			PC_{A3}	-38.51	35.68	0.286				
			PC_{A4}	-270.99	76.67	0.001*				
PC_{A5}			-77.86	106.69	0.469					
PC_{A6}			-420.17	175.41	0.021*					
Intercept			125.12	6.48	<0.0001*					
Model 2		PC_{A1}	38.68	3.41	<0.0001*	0.7378	0.7266	53.045	<0.0001*	
		PC_{A2}	14.54	7.49	0.058					
		Intercept	125.12	7.50	<0.0001*					
24-inch		Model 1	PC_{A1}	37.15	3.97	<0.0001*	0.7167	0.6771	57.645	<0.0001*
			PC_{A2}	-11.95	6.44	0.070				
			PC_{A3}	44.86	41.66	0.288				
			PC_{A4}	269.66	69.96	<0.0001*				
	PC_{A5}		31.45	186.91	0.867					
	PC_{A6}		-337.52	266.20	0.212					
	Intercept		125.12	8.15	<0.0001*					
	Model 2	PC_{A1}	37.15	4.51	<0.0001*	0.6004	0.5834	65.484	<0.0001*	
		PC_{A2}	-11.95	7.31	0.109					
		Intercept	125.12	9.26	<0.0001*					

Note: Var. indicates Variables; Coef. indicates Coefficient; PC_{A1} to PC_{A6} indicate the six principal components extracted from the mean and standard deviation values of each of the three visible bands; RMSE indicates root mean squared error; and * indicates the independent variable is significant at $p = 0.05$ level.

Table 4 and Figure 6 show the model fit results (sample size = 50) of the 6-inch, 12-inch, and 24-inch models when using all six principal components. The 6-inch linear regression model is valid at a 95% confidence interval (the joint p -value (Prob > F) is less than 0.001). The adjusted R-squared value is 0.9439 and the RMSE is 24.087. This error number is acceptable since the ODR assessed by manual evaluation can exhibit an error of up to 84 or up to 50% in terms of variability (Bogus *et al.*, 2010). This implies that natural color aerial photographs with 6-inch spatial resolution can be used to assess and predict overall pavement surface distress rates.

The 12-inch linear regression model is valid at a 95% confidence interval (joint p -value (Prob > F) is less than 0.001). The adjusted R-squared value is 0.7958 and the RMSE is 45.843 which is approximately double that of the 6-inch model. This implies that with a higher error, natural color digital aerial photographs with 12-inch resolution can also be used to assess and predict overall pavement surface distress rates. However, 12-inch models still exhibit less error than manual evaluation ($45.843 < 84$).

The 24-inch linear regression model is valid at a 95% confidence interval (joint P -value (Prob > F) is less than 0.001). The adjusted R-squared value is 0.6771 and RMSE is 57.645. This implies that natural color aerial photographs with 24-inch resolution can still be used to assess and predict overall pavement surface distress rates, but with the highest error of the resolutions assessed. However, it is still better than the manual evaluation ($57.645 < 84$) and it has the advantage of lower cost when compared to higher spatial resolution datasets.

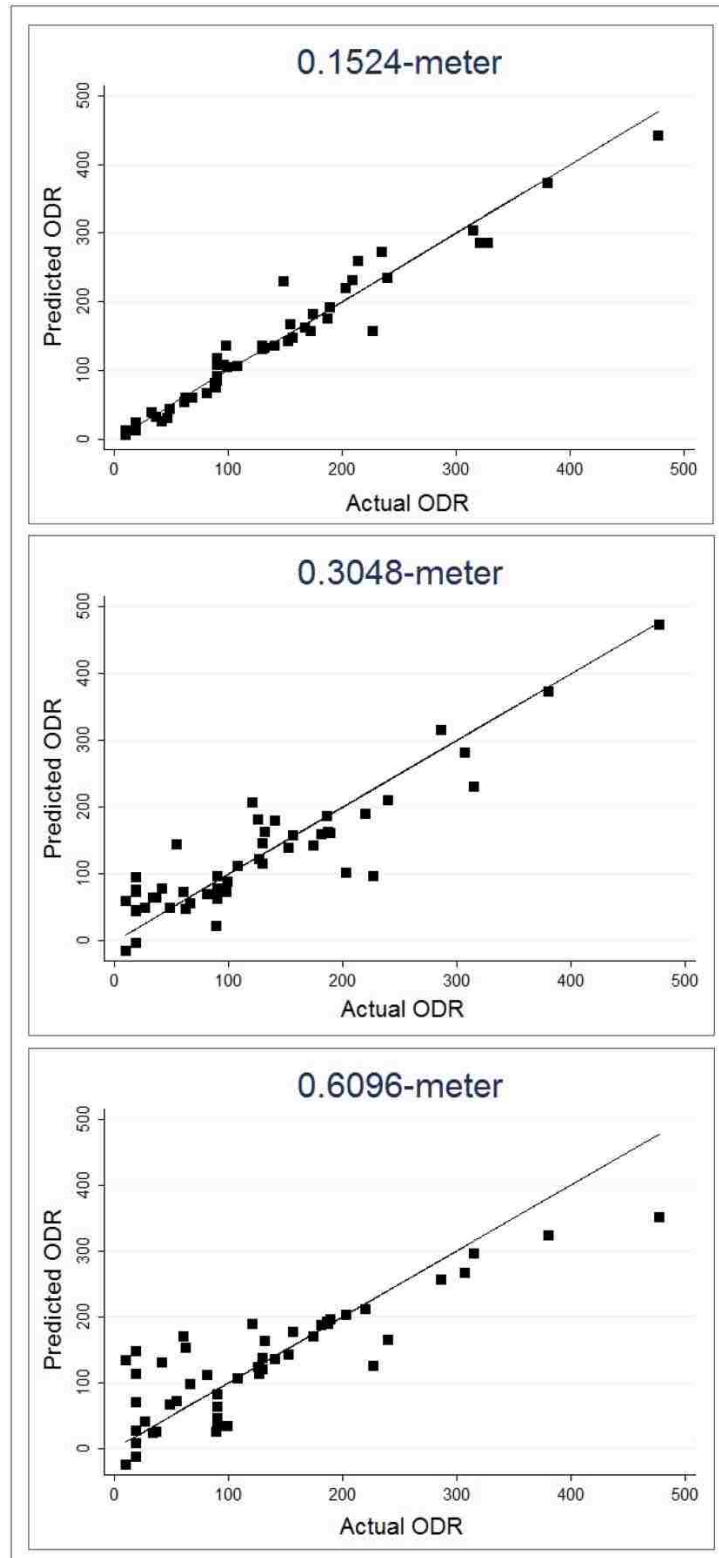


Figure 6. Correlation of predicted ODR versus actual ODR for (a) 6-inch, (b) 12-inch, (c) 24-inch natural color digital aerial photography.

In order to investigate the principles of using HiSR-DAP to infer ODR, this research performed various linear regression models (Model 3 to 7) by using only one visible band and by using only spectral features (mean values) or texture features (standard deviation values). The results were summarized in Table 5. The results revealed that the visible red band best predicts ODR at all spatial resolutions (e.g. 6-inch dataset $R^2 > 93\%$ and $RMSE < 28$), while visible blue band predicts ODR at the lowest certainty. Table 5 also revealed that when compared to texture features, spectral features predict ODR at a higher certainty (e.g. 6-inch dataset $R^2 > 92\%$ and $RMSE < 29$).

Results revealed that the regression model that uses all six principal components exhibited the best capability to predict ODR. Therefore, this model was selected for validation. Table 6 shows the results of the 6-inch, 12-inch, and 24-inch regression models when using only half of the study sites for calibration (sample size = 25). It shows that the R-squared value is decreased while the RMSE is increased for all three models, but not substantially. All three models are still valid at a 95% confidence interval (joint P-value (Prob > F) is less than 0.001).

The other 25 study sites were used to independently validate predicted (model-generated) ODR values versus actual (ground reference) ODR values, the RMSE, mean absolute error, and standard error of which are shown in Table 7. Not surprisingly, the RMSE for each model is higher when validated using holdout samples and predicted using the smaller sample size of 25 to develop the model, but not substantially. In addition, the mean absolute error and standard error are increased when the resolution becomes coarser, but all are less than an error of 84 that manual evaluation can exhibit.

Table 5. Test of a Variety of Options to Infer Overall Distress Rates

Dataset (Size: 50)	Model #	Var.	Coef.	Standard Error	p-value	R ²	Adjusted R ²	RMSE	Prob > F
6-inch	Model 3	PC_{B1}	71.24	3.03	<0.0001*	0.9217	0.9184	29.041	<0.0001*
		PC_{B2}	-4.09	11.80	0.731				
		Intercept	135.36	4.11	<0.0001*				
	Model 4	PC_{G1}	70.80	2.98	<0.0001*	0.9239	0.9206	28.643	<0.0001*
		PC_{G2}	-27.78	12.18	0.027*				
		Intercept	135.36	4.05	<0.0001*				
	Model 5	PC_{R1}	70.71	2.85	<0.0001*	0.9301	0.9271	27.442	<0.0001*
		PC_{R2}	-36.70	12.03	0.004*				
		Intercept	135.36	3.88	<0.0001*				
	Model 6	PC_{S1}	-55.95	2.39	<0.0001*	0.9240	0.9190	28.924	<0.0001*
		PC_{S2}	120.37	34.35	<0.001*				
		PC_{S3}	-34.09	76.27	0.657				
	Model 7	Intercept	135.36	4.09	<0.0001*	0.8806	0.8728	36.252	<0.0001*
		PC_{T1}	53.73	2.99	<0.0001*				
		PC_{T2}	226.37	58.01	<0.0001*				
12-inch	Model 3	PC_{B1}	67.17	5.83	<0.0001*	0.7231	0.7113	54.510	<0.0001*
		PC_{B2}	19.39	12.97	0.142				
		Intercept	125.12	7.44	<0.0001*				
	Model 4	PC_{G1}	66.45	5.91	<0.0001*	0.7379	0.7268	53.030	<0.0001*
		PC_{G2}	31.01	12.66	0.018*				
		Intercept	125.12	7.50	<0.0001*				
	Model 5	PC_{R1}	65.94	6.05	<0.0001*	0.7418	0.7308	52.638	<0.0001*
		PC_{R2}	26.19	13.31	0.055				
		Intercept	125.12	7.71	<0.0001*				
	Model 6	PC_{S1}	48.76	4.64	<0.0001*	0.7129	0.6942	56.103	<0.0001*
		PC_{S2}	104.05	74.77	0.171				
		PC_{S3}	262.22	199.84	0.196				
	Model 7	Intercept	125.12	7.93	<0.0001*	0.5832	0.5560	67.602	<0.0001*
		PC_{T1}	-41.79	5.61	<0.0001*				
		PC_{T2}	116.54	55.58	0.042*				
24-inch	Model 3	PC_{B1}	68.56	7.68	<0.0001*	0.5677	0.5494	68.105	<0.0001*
		PC_{B2}	-11.40	11.28	0.066				
		Intercept	125.12	8.89	<0.0001*				
	Model 4	PC_{G1}	63.27	7.81	<0.0001*	0.5917	0.5743	66.190	<0.0001*
		PC_{G2}	-20.21	12.95	0.125				
		Intercept	125.12	9.36	<0.0001*				
	Model 5	PC_{R1}	68.59	7.68	<0.0001*	0.6317	0.6160	62.865	<0.0001*
		PC_{R2}	-11.40	11.28	0.317				
		Intercept	125.12	8.89	<0.0001*				
	Model 6	PC_{S1}	-42.78	5.99	<0.0001*	0.5285	0.4978	71.898	<0.0001*
		PC_{S2}	27.26	43.98	0.539				
		PC_{S3}	-82.25	231.18	0.724				
	Model 7	Intercept	125.12	10.17	<0.0001*	0.4856	0.4521	75.096	<0.0001*
		PC_{T1}	33.75	6.21	<0.0001*				
		PC_{T2}	290.84	90.70	0.002*				
		PC_{T3}	-540.37	284.34	0.064				
		Intercept	125.12	10.62	<0.0001*				

Note: Var. indicates Variables; Coef. indicates Coefficient; $PC_{B1} - PC_{B2}$ indicate the two principal components extracted from the mean and standard deviation values of the visible blue band; $PC_{G1} - PC_{G2}$ indicate the two principal components extracted from the mean and standard deviation values of the visible green band; $PC_{R1} - PC_{R2}$ indicate the two principal components extracted from the mean and standard deviation values of the visible red band; $PC_{S1} - PC_{S3}$ indicate the three principal components extracted from the mean values of each of the three visible bands; $PC_{T1} - PC_{T3}$ indicate the three principal components extracted from the standard deviation value of each of the three visible bands; and * indicates the independent variable is significant at $p = 0.05$ level.

Table 6. Model Validation for Prediction of ODR Values

Dataset (Size: 25)	Var.	Coef.	Standard Error	<i>p</i> -value	R ²	Adjusted R ²	RMSE	Prob > F
6-inch	<i>PC_{A1}</i>	46.03	3.22	<0.0001*	0.9232	0.8976	37.206	<0.0001*
	<i>PC_{A2}</i>	-13.17	11.74	0.277				
	<i>PC_{A3}</i>	-102.89	61.00	0.109				
	<i>PC_{A4}</i>	264.22	129.98	0.057				
	<i>PC_{A5}</i>	-43.32	152.78	0.780				
	<i>PC_{A6}</i>	-539.59	272.10	0.063				
	Intercept	137.28	7.44	<0.0001*				
12-inch	<i>PC_{A1}</i>	45.33	5.12	<0.0001*	0.8178	0.7571	57.309	<0.0001*
	<i>PC_{A2}</i>	-4.55	13.65	0.743				
	<i>PC_{A3}</i>	42.88	59.73	0.482				
	<i>PC_{A4}</i>	-175.53	143.74	0.238				
	<i>PC_{A5}</i>	50.69	241.64	0.836				
	<i>PC_{A6}</i>	187.02	335.35	0.584				
	Intercept	137.28	11.46	<0.0001*				
24-inch	<i>PC_{A1}</i>	33.06	7.73	<0.0001*	0.7166	0.6222	71.476	<0.0001*
	<i>PC_{A2}</i>	-42.78	9.45	<0.0001*				
	<i>PC_{A3}</i>	125.42	76.79	0.120				
	<i>PC_{A4}</i>	-231.38	118.32	0.066				
	<i>PC_{A5}</i>	-88.60	300.07	0.771				
	<i>PC_{A6}</i>	194.58	486.38	0.694				
	Intercept	137.28	14.30	<0.0001*				

Note: Var. indicates Variables; Coef. indicates Coefficient; *PC_{A1}* and *PC_{A6}* indicate the six principal components extracted from the mean and standard deviation values of each of the three visible bands; RMSE indicates root mean squared error; and * indicates the independent variable is significant at *p* = 0.05 level.

Validation results, consistent with model fits, show that the 6-inch aerial photography results in the lowest error when compared to manual evaluation results, whether measured by RMSE, mean absolute error, or standard error. Therefore, we conclude that ODR can be most effectively predicted by the 6-inch aerial photography. While none of the models can be used to detect detailed distress (e.g., cracks) or vertical distress (e.g., rutting), all models indicate potential for the direct estimation of ODR with less error than manual approaches.

One limitation of the proposed method is that it cannot be used for high traffic volume sections. This is because vehicles are considered as unwanted features on the pavement. Too many vehicles present in the images could reduce the area of pavement

observed to such a degree that distress cannot be accurately evaluated. This proposed method also must use reference pavement surface distress rates (collected either through manual evaluation or automatic evaluation) to develop initial model calibrations.

Table 7. Error Summary for Predicted ODR

Dataset (Size: 25)	RMSE	Mean Absolute Error	Standard Error
6-inch	42.8826	35.0000	5.0577
12-inch	63.1958	43.7600	9.3070
24-inch	72.5551	66.2400	12.0770

3.4 Conclusions

Routine evaluation of pavement surface distress condition is a challenge to all transportation agencies. In the real world it is impossible to get exhaustive condition data for all pavement surfaces. Current methods for pavement surface distress evaluation are time-consuming and expensive. To overcome these limitations, this research presents a novel approach for overall pavement surface distress condition evaluation through the analysis of routinely-acquired and publically-available HiSR-DAP. These images are already paid for through a variety of means, permitting a dramatic reduction in the cost of intensive survey through manual or automated samples, making it extremely practical and immediately implementable across all regions without tree cover. Our results have shown that natural color aerial photographs of 6-inch spatial resolution can be used to evaluate the overall pavement distress conditions with a high degree of certainty ($R^2 > 95\%$). At a lesser degree of certainty, 12-inch and 24-inch natural color aerial photographs can also be used to detect overall pavement conditions. When considering the associated cost, the

lower spatial resolution aerial photographs can be potentially applied to evaluate overall pavement surface distress for rapid, high-level information checks. Research results also have shown that visible red band or spectral features alone can be used to estimate the overall pavement conditions with a high degree of certainty ($R^2 > 92\%$).

The proposed method of detecting pavement surface distress conditions by analyzing HiSR natural color digital aerial photography could be used as a predictor of overall distress conditions in situations where field inspectors cannot evaluate except with considerable labor (e.g., sections in remote areas). It is not likely that the proposed method will completely replace field pavement surface inspection due to its lack of crack-level detailed pavement surface distress information and the necessity of using field pavement surface distress inspection results as reference data to develop the regression models. However, the spectral response in HiSR natural color digital aerial photography presents additional information not considered in field inspection and could be used to predict the overall pavement surface conditions in un-sampled areas based on a dramatically reduced number of intensive survey sites. Therefore, it can reduce the amount of work, time, and money associated with pavement surface evaluation. Operationally this proposed approach could be readily implemented as a service internally by transportation agencies such as NMDOT or implemented through consulting firms. Eventually this proposed method could be automated through software development. Such software would only require users to insert the pavement surface distress rates of a limited number of manual survey sites, add associated HSR multispectral digital aerial photography, and upload the evaluation polygon, while the computing-intensive processes such as eliminating unwanted features is fully automated.

Chapter 4 Characterizing Pavement Surface Distress Conditions with Hyper-spatial Resolution Natural Color Digital Aerial Photography (HySR-DAP)

4.1 Introduction

Because of constant and frequent usage, roadway maintenance is an essential task to ensure the correct pavement performance (Oliveira and Correia 2008). Accurate condition assessment of pavement surface distress provides a critical input to the decision making process regarding pavement management (Georgopoulos et al. 1995).

Surveying roadway pavement surface distress conditions plays an important role in its function and structural evaluation analysis, influencing the adoption of adequate maintenance policies (Oliveira and Correia 2008). Historically, pavement evaluation was commonly performed with “boots on the ground” by having experts visually inspect the surface conditions with subjective *in situ* engineering judgment and interpretation (Kim et al. 2006; Schnebele et al. 2015). Pavement surface conditions were observed and recorded by inspectors in person in the field “walk and look” and the hand-written data was later inputted into a computer database.

In the 1980s, vehicle-mounted electronic sensors (e.g., video cameras, digital cameras, and laser sensors) at a fine enough resolution emerged and were used for automated pavement surface evaluation (Haas et al. 1985; Curphey et al. 1986; Hudson and Uddin 1987; Schnebele et al. 2015). Both manual observation and automated observation methods are classified as ground-based evaluation methods because the evaluation action occurs from the ground. Ground-based evaluation methods can collect

detailed pavement surface condition data for various types of distresses (e.g., alligator cracking and transverse cracking). However, these methods are expensive (McGhee 2004), labor-intensive (manual observation only) (Cheng and Miyojim 1998; Hudson and Uddin 1987; Cheng et al. 1999; Wang and Li 1999; Wang 2000; Schnebele et al. 2015), time-consuming (Schnebele et al. 2015), tedious (Timm and McQueen 2004), subjective (manual observation only) (Sokolic 2003; Hong 2009; Attoh-Okine and Adarkwa 2013), potentially dangerous to inspectors in the hazardous roadway environment (Schnebele et al. 2015), require specialized staff on a regular basis (Wolters et al. 2011), and can exhibit a high degree of variability (Bogus et al. 2010), thereby causing inconsistencies in surveyed data over space and across evaluation (Zhang et al. 2015). In addition, data collected on the ground serves only a single purpose (i.e., pavement surface evaluation) and cannot be shared with other government agencies (e.g., U.S. Geological Survey) to reduce the cost (Zhang et al. 2015).

Another method to evaluate pavement surface is through airborne observation. Airborne methods require deploying cameras (both analog and digital) on aircraft that can fly over pavement sections. Airborne remote sensing techniques, also known as aircraft-based evaluation, is getting more attention because of its synoptic coverage (Jensen and Cowen 1999), although it has not been used for operational evaluation programs to the author's knowledge. The resulting aerial images, which typically have high-spatial resolutions ranging from 3-inch (0.075 m) to 1 m, can be used to evaluate the overall condition of pavement surfaces in a more rapid, cost-effective (data can be shared with other government agencies), and safer manner (Zhang et al. 2015; Zhang and Bogus 2014). However, the spatial resolutions of these images limit the ability to detect and

assess fine and detailed defects such as individual cracks on a pavement surface because most cracks have widths less than 0.01 m (Guo 2010). Although visual interpretation of large scale (e.g., 1:100) panchromatic analog aerial photographs can be used to identify untreated cracks and other high-contrast pavement defects such as patching and bleeding, extremely high cost and limited compatibility with modern image processing techniques ultimately prevent the further exploration of their applications for pavement surface distress evaluation (McMaster 1952; Stoecker 1968; Stoecker 1970).

The above literature reveals the actual obstacle for using digital aerial images for detailed pavement surface distress evaluation is the spatial resolution is too coarse to resolve detailed distresses, which often manifest at the millimeter scale. Recent advances in remote sensing have enabled us to effectively collect hyper-spatial resolution (sub-centimeter or sub-inch) natural color digital aerial photography (HySR-DAP) at a low cost. HySR-DAP has been used to facilitate research in many fields, such as archaeology (Verhoeven, 2009), ecology (Scoffin, 1982; Aber et al. 1999; Guichard et al. 2000), zoology (Fraser et al. 1999), emergency management (Sklaver et al. 2006), vegetation and soil monitoring (Aber et al. 2001), and topographic mapping (Wundram and Loffler 2008; Marzloff and Poesen 2009; Smith et al. 2009). However, previous studies regarding the application of HySR-DAP for detailed pavement surface distress condition assessment are limited. The only published research on this topic was performed by Chen et al. (Chen et al. 2011). This research shows the potential to use HySR-DAP to evaluate crack-level pavement surface distress conditions, but the assessment capability is limited to 2 cm wide cracks on bridge pavements because the spatial resolution of the used HySR-DAP is 1-inch (0.025 m).

Based on our review of literature, the use of HySR-DAP for evaluating detailed pavement surface distress condition is lacking and presents a significant gap in the research. The intellectual significance of this research lies in exploring the utility of millimeter scale HySR-DAP acquired from a low-altitude and low-cost small-unmanned aircraft system (S-UAS), in this case a tethered helium weather balloon, to permit characterization of detailed pavement surface distress conditions. Unlike the ground-based or aircraft-based evaluation methods, this research collected detailed pavement surface distress information through a middle-ground approach – using a low-altitude S-UAS.

To collect millimeter scale HySR-DAP and appropriately process them for characterizing detailed pavement surface distress conditions, two emerging remote sensing techniques, including S-UAS based hyper-spatial resolution imaging and aerial triangulation (AT) are leveraged for image collection and image processing. An S-UAS, which can fly lower to the ground than traditional manned aircraft, and thus permit ready collection of hyper-spatial resolution (HySR, i.e., ground sampling distance (GSD) < 1 cm) aerial images using compact low-cost sensors, is used for HySR-DAP collection. AT, also known as structure-from-motion (SfM) in the computer vision field, is used to process the collected HySR-DAP to generate millimeter GSD mosaicked orthophotos and digital surface models (DSMs) for standardized evaluation of detailed horizontal and vertical pavement surface conditions, potentially reducing the cost and duration of evaluation while improving the comparability of surveyed results.

In recent years, S-UAS have emerged as an important platform for collection of HySR aerial data (Colomina and Molina 2014; Tang and Shao 2015)—a trend that is all

but certain to continue (Lippitt 2015). For now, due to a wide variety of regulatory and safety concerns, the legal use of S-UAS is severely restricted in the United States. In anticipation of an established regulatory environment and availability of S-UAS for routine pavement surface distress evaluation, this research used a tethered helium weather balloon system to simulate the collection of HySR-DAP from untethered S-UAS, as suggested by the Public Lab (Balloon & Kite Mapping 2014). This organization is a popular community across the world for researchers/hobbyists using inexpensive do-it-yourself (DIY) S-UAS to collect various remote sensing data, including HySR-DAP. Currently, the tethered helium weather balloon is not restricted from flying in the United State as long as the flight location is 5 miles (8 km) away from the airports and the flight altitude above ground level (AGL) is less than 400 ft (120 m) (Balloon Regulations & Policies 2014).

As a basic photogrammetric method, AT is used for calculating the three-dimensional (3D) coordinates of objects by analyzing overlapping aerial images captured from varied perspectives (Yuan et al. 2009). AT traditionally requires the manual identification of thousands of control points linking images to one another and to a reference dataset to enable least squares estimation of the optimal triangulation model. New computation approaches (e.g., SfM and graphic processing unit (GPU) based image processing) have enabled the automation of traditional AT and expansion of the number of triangulated XYZ locations to millions up to hundreds of millions, ultimately permitting routine estimation of 3D surface structure and subsequently orthorectification of large datasets at approximately the spatial resolution of input images (Zhang et al. 2011; Zomrawi et al. 2011). When coupled with HSR aerial image data such as that collected

by low-altitude S-UAS, this technique holds the potential to permit the estimation of horizontal and vertical measurements at millimeter scales (Zhang et al. 2011), and ultimately, the detection and assessment of pavement surface distresses at finer scales than has traditionally been possible by airborne survey.

HySR-DAP acquired from S-UAS has already been commercially applied in the context of airport runway condition assessment in Germany (Airsight 2016), which indicates its application in roadway pavement surface condition assessment is promising. Using roadway flexible pavement (i.e., asphalt concrete) sections in the State of New Mexico in the United States as an example, we explored the utility of AT technique and millimeter scale HySR-DAP acquired from a low-altitude and low-cost S-UAS to characterize detailed pavement surface distress condition to assess: (1) if millimeter-scale HySR-DAP can be used to characterize detailed pavement surface distress condition, and if they can; (2) how well can HySR-DAP characterize detailed pavement surface distress conditions when compared with ground-based manual measurement? The answers to these questions lay the foundation for the development of automated procedures for the extraction of detailed pavement surface distress metrics and operational use of HySR-DAP to detect and assess pavement surface distress conditions.

4.2 Materials and Methods

Using HySR-DAP acquired from a low-altitude and low-cost S-UAS as input, AT was used to generate 3 mm GSD mosaicked orthophotos and co-registered DSMs for characterizing pavement surface distress conditions. Key metrics used to evaluate flexible pavement surface distresses were identified from the United States Department of Transportation (USDOT) Highway Performance Management System (HPMS) Field

Manual (HPMS 2014), and included rutting (item 50), alligator cracking (item 52), and transverse cracking (item 53). These metrics were measured from the orthophotos and DSMs and then compared with ground reference data manually collected by trained inspectors using standard protocols (Cordova et al. 2009). Unlike the manual evaluation methods operationally used by transportation management agencies, which are characterized by subjective visual observation, inspectors of this research used measuring tapes to objectively measure distresses.

4.2.1 Data Acquisition and Preparation

A low-altitude AGL and low-cost S-UAS was constructed to simulate the collection of HySR-DAP from other untethered low altitude AGL S-UAS (Figure 7) that are now common in the marketplace. This system includes a tethered helium weather balloon with custom-designed rigging based on the Picavet suspension system, as suggested by the Public Lab (Balloons & Kite Mapping 2014). As mentioned in the previous section, a tethered helium weather balloon is permitted to fly in the United States as long as the flight meets the rules about location and altitude. The sensor affixed to the platform was an off-the-shelf small-format Canon SX260 HS digital camera. This camera has a 12-megapixel Complimentary Metal-Oxide Semiconductor (CMOS) detector array collecting in the visible blue, green, and red wavelength bands through Bayer array sampling and a built-in GPS unit. A firmware enhancement application known as the Canon Hack Development Kit (CHDK), was used to permit more control over the operation of the Canon SX260 HS camera, including shutter speed, shutter lag, aperture size, and intervalometer (Figure 8).

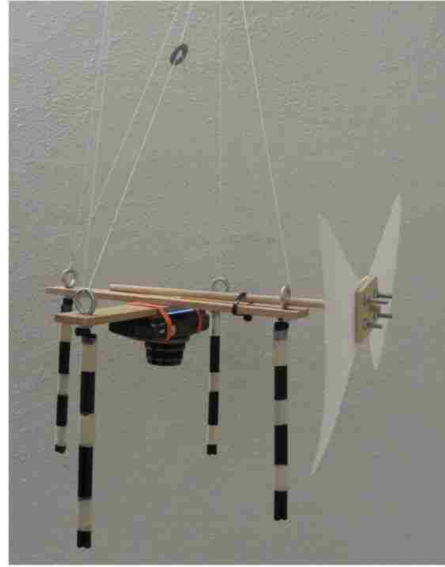


Figure 7. Examples of untethered low altitude AGL S-UAS; (a) rotary-wing S-UAS; (b) Fixed-wing S-UAS

HySR-DAP data were collected from 28 study sites (i.e., sections of roadway pavement surfaces) in Bernalillo County, New Mexico. Twenty-one sites were located on United States Highway 66, two sites were located on the campus of the University of New Mexico (UNM), and five sites were located on New Mexico Highway 333. All study site roadways run in a generally east-west direction. Approximately 300 overlapping HSR aerial images were acquired for each study site at about 5 m AGL to permit a nominal GSD of 0.002 m. At this AGL, the size of the ground area covered by each frame is approximately 8×6 m. Image acquisition was not controlled into flight lines, but was instead collected as a highly redundant block in a largely randomized pattern. However, the long side of each frame was approximately aligned perpendicular to the roadway while the short side of each frame was approximately parallel to the roadway. Crab angles were relatively stable along the roadways because balloon operators were standing along the shoulder of the roadways.



(a)



(b)



(c)



(d)

Figure 8. The helium weather balloon small-unmanned aircraft system (S-UAS); (a) a filled helium weather balloon and a helium tank; (b) customized rigging and mounted Canon SX260 HS digital camera; the characteristics of the rigging are lightweight, durable, resilient, capable of protecting the sensor, capable of removing the string in the aerial images and capable of dynamically adjusting the sensor position (i.e., the lens always facing down the nadir or principal point); (c) balloon mapping kit, including a balloon, reels, gloves, rubber bands, and zip ties; (d) front facet of Canon SX 260 HS digital camera and Canon Hack Development Kit (CHDK) graphical user interface (GUI).

Ground control point (GCP) data were collected by a trained six-person surveying crew at each of the 28 sites. GCPs were identified using identifiable objects on the pavement surfaces, including sharp edges of cracking, intersections of cracking, and asphalt stains. GCPs were collected on the pavement surfaces using a survey grade CHC X900+ real-time kinematic (RTK) Global Navigation Satellite System (GNSS) in a base/rover configuration (Figure 9). Base stations were set up over National Geodetic Survey (NGS) benchmarks. Data were collected using the Carlson SurvCE software package and a WGS84 UTM Zone 13 North projection. When collecting the GCP coordinates, detailed photos of each GCP were acquired with the survey instrument in place. These detailed photos were used to facilitate the placement of GCPs on the acquired HSR aerial imagery. A total of 16 GCPs were collected for each site. The collected GCP coordinates were post-processed with the National Oceanic and Atmosphere Administration (NOAA) Online Positioning User Service (OPUS) and the ultimate root mean square (RMS) RTK accuracy achieved was 0.004 m + 1 ppm horizontally and 0.006 m + 1 ppm vertically.

A ground reference dataset of pavement surface conditions was collected by a trained two-person crew at each of the study sites. The crew performed manual measurements based on the standard evaluation protocols adopted by the HPMS Field Manual. Both inspectors assessed pavement surface distresses (rutting, alligator cracking, and transverse cracking) independently and the results were recorded as the average value of the two independent measurements. In accordance with the HPMS Field Manual, rutting depth was measured for only the rightmost driving lane for both inner and outer wheel paths at three locations along the wheel path within each site and then the depth

was averaged for each wheel path. The HPMS Field Manual requires reporting the percent area of total alligator cracking to the nearest 5%. For transverse cracking, the HPMS Field Manual requires reporting an estimation of relative length in meters per kilometers (feet per mile).



Figure 9. An illustration of the RTK system in a base/rover configuration.

4.2.2 Aerial Triangulation

After excluding blurred and oblique HSR aerial images, between 120 and 300 overlapping aerial images were processed and assessed for each study site according to the protocols established by Zhang et al. (Zhang et al. 2016). As one of the most complex photogrammetric workflows, traditional AT is composed of many processes, which include image import, interior orientation, tie points determination, GCP measurements, bundle block adjustment, and quality control (Kersten 1999). As in traditional AT,

automated AT (or SfM) uses overlapping images acquired from multiple viewpoints (Kersten 1999). However, automated AT differs from traditional AT by determining internal camera geometry using an *in situ* automated process and by triangulating camera position and orientation automatically without the need for a pre-defined set of visible GCPs at known 3D positions [53] (Westoby et al. 2012). To do so, automated AT requires a high degree of overlap (ideally 75% for sidelap and 80% for forward overlap) to observe the full geometry of scene structure (Zhang et al. 2011). For this research, images were collected in a hyper redundant block pattern and the sidelap and forward overlap percentage meet or exceed the 75% and 80% requirements identified by Zhang et al. (Zhang et al. 2011).

In recent years, many software packages have emerged to efficiently implement automated AT. The commercial software Agisoft Photoscan was selected as the tool of choice for this study as it permits minimal human intervention. Among the 16 GCPs, 10 were used to calibrate the automated AT process while the remaining six were reserved to evaluate the horizontal and vertical accuracy of the AT outputs, including orthophotos and DSMs.

For each of the 28 study sites, an *in situ* camera model was generated based on all of the input HySR aerial images. Therefore, the camera model is not identical across the sites. For each of the study sites, millions of tie points were automatically identified from the input of overlapping images to build a dense point cloud, and then a triangulation irregular network (TIN) mesh was generated based on the identified tie points. Lastly, a DSM was created based on the digital mesh and a mosaicked orthophoto was created based on input images to co-register with DSM.

Once these processes were completed, orthophotos and the DSMs were exported as rasters in TIFF format at a spatial resolution of 0.003 m. Orthophotos and DSMs are generated in a single processing routine and are therefore tightly co-registered. An example of the orthophotos and DSM are showed in Figure 10. Orthophotos were used to assess the horizontal accuracy while DSMs were used to assess the vertical accuracy. Root-mean-squared-error (RMSE) was used to assess the accuracy (Congalton and Green 2009), and the results show that the overall horizontal accuracy is 0.004 m while the overall vertical accuracy is 0.007 m. The number of overlapping images used and accuracy for each study site is reported in Table 8. More details regarding the accuracy assessment can be found in the study performed by Zhang et al. (Zhang et al. 2016).

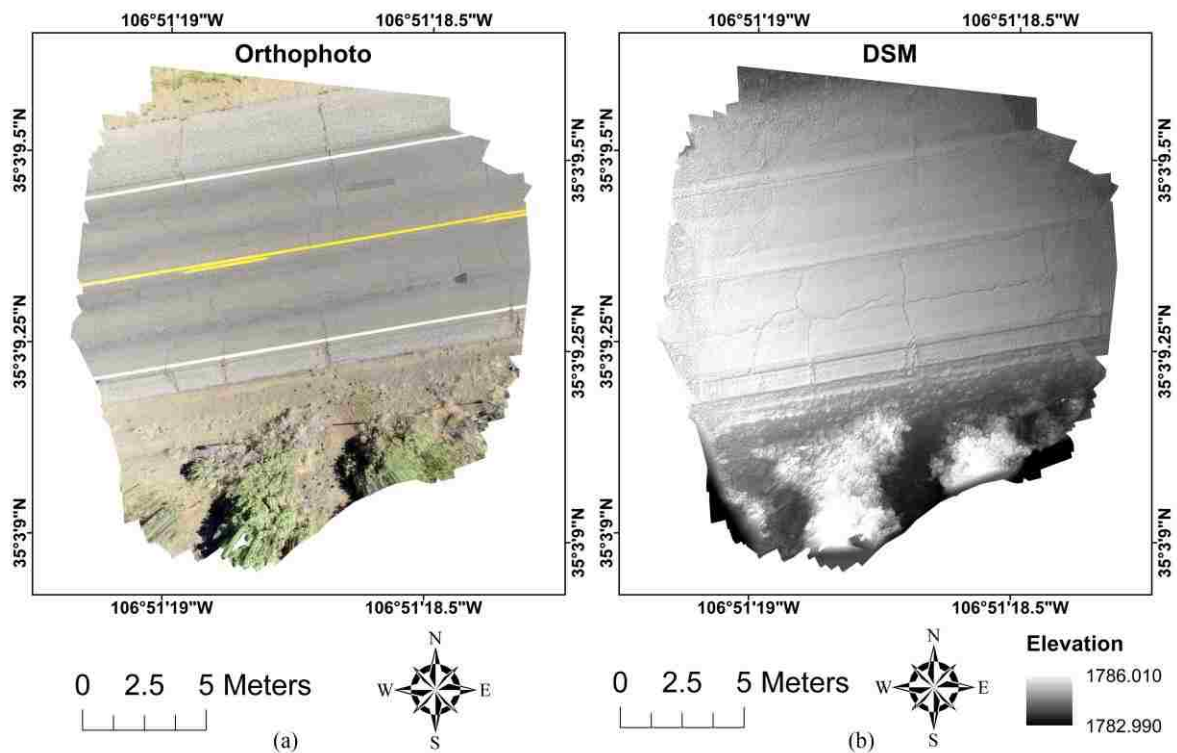


Figure 10. (a) An example of hyper-spatial resolution orthophotos with 0.003 m resolution and (b) an example of hyper-spatial resolution digital surface model (DSM) with 0.003 m resolution. The black to white color scale in (b) indicates elevations.

Table 8. Accuracy Assessment Result (RMSE) for Each Study Site. RMSE refers to root-mean-squared-error

Study Site	No. of Image Frames	Horizontal Accuracy (m)	Vertical Accuracy (m)
1	122	0.003	0.006
2	135	0.005	0.011
3	183	0.003	0.006
4	177	0.003	0.007
5	181	0.003	0.007
6	180	0.004	0.008
7	165	0.004	0.006
8	133	0.004	0.006
9	126	0.003	0.006
10	189	0.003	0.006
11	162	0.005	0.007
12	156	0.004	0.006
13	292	0.005	0.007
14	207	0.005	0.008
15	163	0.005	0.008
16	150	0.005	0.007
17	225	0.004	0.007
18	155	0.004	0.008
19	145	0.004	0.007
20	136	0.003	0.005
21	168	0.004	0.006
22	130	0.003	0.006
23	105	0.003	0.006
24	103	0.004	0.005
25	109	0.004	0.006
26	155	0.004	0.007
27	112	0.003	0.006
28	115	0.003	0.006
Mean	157	0.004	0.007

4.2.3 Rutting Depth Measurement

Rutting is an unrecoverable longitudinal surface depression in both inner and outer wheel paths (Cordova et al. 2009). In ground-based manual measurement, rutting depth was measured with a wooden bar and a measuring tape. The wooden bar was used

as a reference line between the two highest points of the rut and the measuring tape was used to measure the distance from the lowest point on the pavement surface perpendicularly to the point at the bottom of the wooden bar that is perpendicular to the lowest point. The actual measured points in the field are the lowest points as visually determined by inspectors. The minimum scale of the measuring tape used for manual evaluation was 0.001 m. The length and width of the wooden bar is 48-inch (1.22 m) and 0.8-inch (0.02 m).

DSMs (reconstructed 3D pavement surface) were used to measure rutting depths using a digital process designed to simulate the ground-based manual measurement. Points and polygons were created on DSMs to simulate the locations of the actual measured points and wooden bars. The actual measured points in the field and the locations of the wooden bars are shown in Figure 11. With the actual measured point (as photographed in the field) as the center, two polygons (one on either side of the filed measured point) with a size of 0.61 m by 0.02 m were created to simulate the location of the wooden bar.

Unlike ground-based manual measurement, it is not possible to directly identify the highest point at the bottom of the wooden bar. Therefore, the following method was used to identify the highest and lowest points of rutting. Using the polygon as the boundary, the DSM pixels within the boundary were extracted and reclassified to find the highest point on both sides of the actual field measured points. If there were multiple pixels having the same highest value, the one closer to the actual measured point in the field was used.

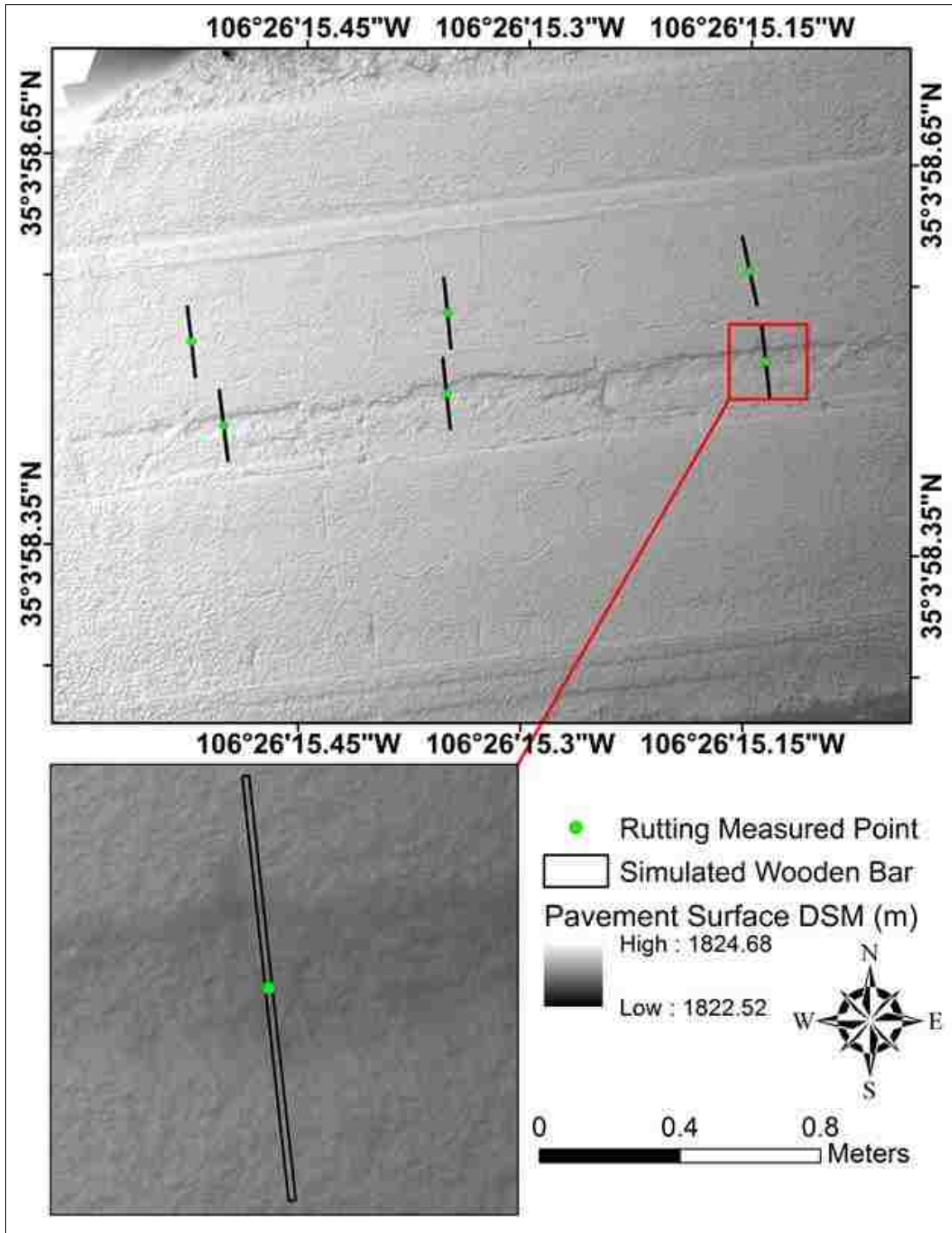


Figure 11. An illustration of the locations of rutting depth actual measured points and wooden bars.

Then, as shown in Figure 12, the two highest points within the two polygons are considered as Point A and Point B, while the two measured points as Point C and Point D. The distance from Point C to Point D is the rutting depth. Points A, B, and C will have the same height if the heights of Points A and B are equal. However, under most circumstances the heights of Points A and B are different. Therefore, a weighted average method was used to calculate the height of Point C:

$$H_C = \frac{H_A * D_A + H_B * D_B}{D_A + D_B} \quad (9)$$

$$RD = H_C - H_D \quad (10)$$

where H represents the height of a given point, and therefore H_A represents the height of Point A, and H_B represents the height of Point B. D_A represents the horizontal distance from Point A to Point D, while D_B represents the horizontal distance from Point B to Point D. RD represents the rutting depth. H_A and H_B were determined from the DSMs, while D_A and D_B were determined from the orthophotos.

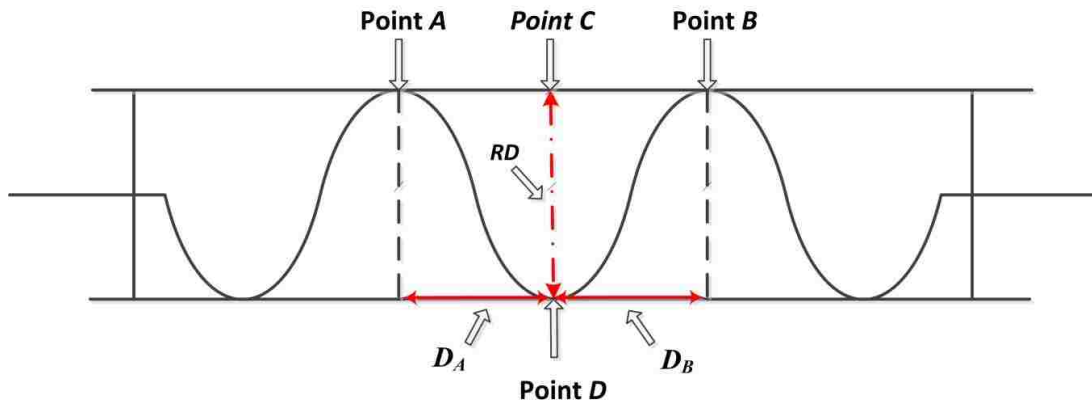


Figure 12. Rutting depth calculation process. D_A indicates the horizontal distance from Point A to Point D, while D_B is the horizontal distance from Point B to Point D. RD indicates the calculated rutting depth.

4.2.4 Alligator Cracking Measurement

Alligator cracking is interconnected cracks resembling check wire or alligator skins (Cordova et al. 2009). Longitudinal cracking (cracks that are parallel to the pavement's centerline) should also be included as alligator cracking (HPMS 2014). According to the HPMS Field Manual, alligator cracking should be reported as the percentage of the total evaluated area to the nearest 5% at a minimum. In manual evaluation, inspectors measure the cumulative length of alligator cracking and mark the location of occurrence in one or two wheel paths. For example, typically the width of the driving lane is 12 ft (3.66 m), and therefore, for a 328 ft (100 m) section, the total area is 3940 ft² (366 m²). If alligator cracking exists for both wheel paths, and for each wheel path the total length of the measured alligator cracking is 49 ft (15 m) while the width is 1.64 ft (0.5 m), the total area of the measured alligator cracking is 15 m² ($15 \times 0.5 \times 2 = 15$). There the total area percentage should be 5 percent ($15/366 \times 100 = 4.09\%$, which should be rounded up to the nearest 5 percent, which is 5%).

In order to simulate the alligator cracking measurement prescribed by the HPMS Field Manual, orthophotos were visually analyzed to locate alligator cracks and then mark them with on-screen digitization in GIS software. Polygons were digitized to represent both the entire evaluated pavement section and the sections that alligator cracking occurred. The polygon defining the entire evaluated pavement section was used to calculate the total evaluated area, while the polygons defining alligator cracking were used to calculate the total area of alligator cracking. The area percentage of alligator cracking was then calculated by comparing the areas of the two sets of polygons. The use of polygons to determine area percentage of alligator cracking is shown in Figure 13. It

should be noted that both actual area percentage and rounded area percentage were calculated for each site, but only rounded area percentage was used for comparison to ground-based manual measurements.

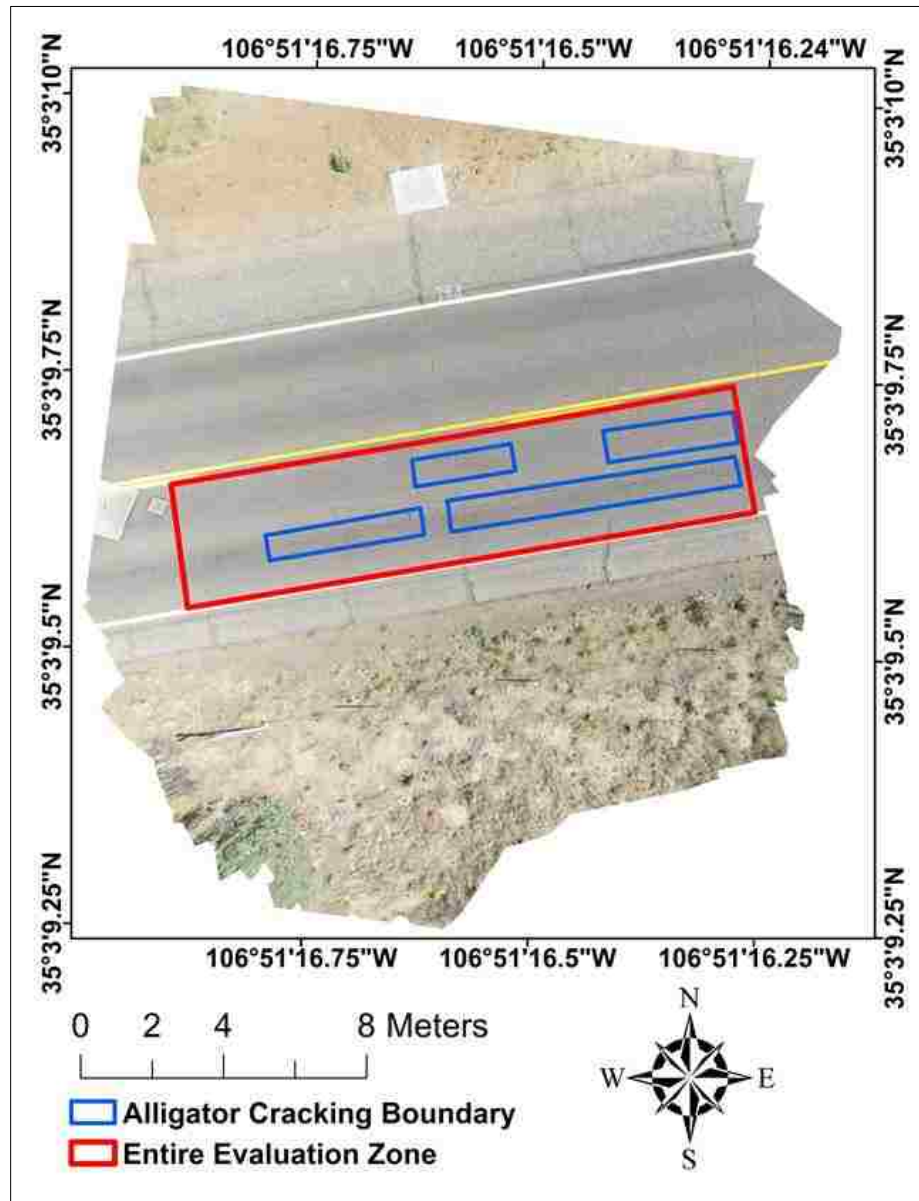


Figure 13. An illustration of orthophoto-based alligator cracking measurement. The blue polygons are the digitized alligator cracking area while the red polygon is the entire manual evaluation zone. Areas for these polygons can be calculated with GIS software and therefore, alligator cracking area percentage can be determined by dividing alligator cracking area by the entire evaluation zone area.

4.2.5 Transverse Cracking Measurement

Transverse cracking are cracks that are perpendicular to the pavement's centerline (Cordova et al. 2009). According to the HPMS Field Manual, field inspectors should measure the length of each transverse crack that extends at least half of the lane width (6 ft [1.83 m] or longer cracks) to calculate the total length of transverse cracking. The total length of transverse cracking will be normalized by the total length of the evaluated pavement section, and therefore, the final results will be delivered in the format of feet per mile (or meter per kilometer).

In order to simulate the transverse cracking measurement prescribed by the HPMS Field Manual, orthophotos were visually analyzed and any transverse cracks longer than 6 ft (1.83 m) were identified and digitized in GIS software as polylines to facilitate the calculation of total length of transverse cracking (Figure 14). The same polygon created for the alligator cracking measurement representing the entire evaluated pavement section was used to measure the total length of the evaluated pavement section.

4.2.6 Measurement Results Comparison

For each study site, rutting depth (for both wheel paths), alligator cracking area percentage, and transverse cracking length measured from the DSMs and orthophotos were compared with ground-based manual measurement results to examine the utility of using HSR-AP derived products to detect and assess detailed pavement surface distresses. In order to select the most appropriate statistical test, the sample size of each set of measurements was examined. Most statistical researchers and scientists accept that non-parametric statistical tests should be employed if the sample size is less than 30 (Agresti and Min 2003; Tomkins 2006; Arnold and Emerson 2011; Hoskin 2014), even if sample

values are normally distributed. The examination revealed that the sample size for each set of measurements was 28, and therefore, non-parametric statistical tests were used to compare ground-based measurements with HSR-AP derived products based measurements.

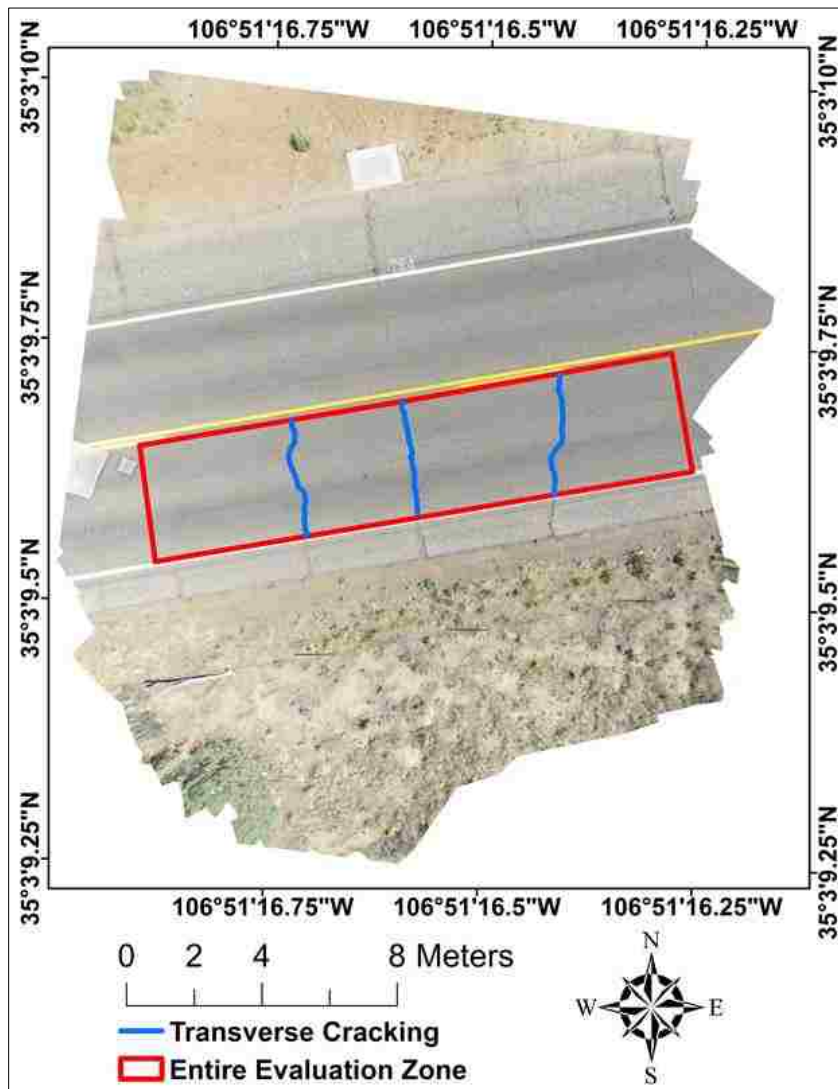


Figure 14. An illustration of orthophoto-based transverse cracking measurement. The blue polylines are the digitized transverse cracking while the red polygon is the entire evaluation zone. The lengths of these transverse cracks and the length of the entire evaluation zone can be calculated with GIS software and, therefore, transverse cracking length can be determined by dividing total transverse cracking length by the entire evaluation zone length.

Measurement comparisons were performed as a paired group and unpaired group. Paired group tests are more appropriate if two groups of measurements are dependent (i.e., repeated measurements for the same subject but at two different times). Unpaired group tests are more appropriate if two groups of measurements are independent (i.e., measurement for one sample in Group A has no bearing on the measurement for one sample in Group B). The relationship between ground-based manual measurements and HySR-DAP derived products measurements can be interpreted in both a dependent way and an independent way. In the dependent way, repeated measurements of a specific distress at a study site were performed on the ground and from HySR-DAP derived products at two different times, and therefore, they are dependent. In the independent way, the ground-based measurement of a specific distress at a study site has no bearing on the HySR-DAP derived product based measurement of a specific distress at the same study site since they are measured from two different data sources. Since the relationship can be interpreted in both ways, to err on the side of caution, this research used both paired group and unpaired group statistical tests to examine if the detailed pavement surface distress rates measured from HySR-DAP derived products and distress rates manually measured on the ground are statistically different.

In the paired group comparisons, repeated measurements (i.e., ground-based measurement and HySR-DAP derived products based measurement) of a specific distress (e.g., alligator cracking) for a specific study site (e.g., site 20) constitute a pair, and the purpose of this comparison is to examine whether the median difference between the two sets of paired measurements is zero. Nonparametric Wilcoxon Signed Rank test

(Wilcoxon 1945), which does not assume normality in the data, was used in this study as a robust alternative to parametric Student's *t*-test.

In the unpaired group comparisons, two sets of measurements (i.e., the ground-based measurement and the HySR-DAP derived products based measurement) of a specific distress constitute two independent groups, and the purpose of this comparison is to examine whether two independent groups of samples exhibit the same distribution pattern (i.e., shape and spread) or have differences in medians. Nonparametric Mann-Whitney U test (Mann and Whitney 1947), also known as Wilcoxon Rank-Sum test, which also does not assume normality in the data, was used to detect differences in shape and spread as well as differences in medians.

4.3 Results

For rutting depth, the ground-based and DSM-based measurements are summarized in Table 9. It should be noted that the results are organized by inner and outer wheel paths for each study site. Table 10 summarizes the ground-based and orthophoto-based measurements for alligator cracking area percentage and transverse cracking length.

The box plots, histogram plots, and radar plots displaying each set of measurements were visually examined and are shown in Figures 15–17. Box plots revealed that only DSM-based rutting measurement showed evidence of outliers (dots found above the whiskers). However, box plots did not show a substantial difference in the medians between ground-based measurements and HySR-DAP derived products based measurements. There also did not appear to be a substantial difference in the box sizes. Histogram plots provide a visual presentation of the frequency distribution of each distress' measurement differences (residuals). Measurement difference was defined as the

difference between ground-based measurement and HySR-DAP derived products based measurement. The plots did not show a substantial difference in the two sets of measurements for each distress. Most of the residuals were distributed around the value of zero. Radar plots provide another visual presentation of the measured distress rates for each study site. The plots did not reveal a substantial difference in the shape and spread of distribution between the two sets of measurements for each distress.

Table 9. Rutting Depth Measurements for Inner and Outer Wheel Path (in m)

Site ID	Inner Wheel Path		Outer Wheel Path	
	Ground Depth	DSM Depth	Ground Depth	DSM Depth
1	0.021	0.024	0.006	0.009
2	0.012	0.020	0.009	0.017
3	0.015	0.016	0.007	0.007
4	0.017	0.017	0.008	0.013
5	0.022	0.019	0.018	0.015
6	0.019	0.016	0.021	0.017
7	0.017	0.022	0.018	0.023
8	0.022	0.018	0.018	0.017
9	0.013	0.013	0.016	0.018
10	0.008	0.010	0.015	0.016
11	0.020	0.016	0.024	0.021
12	0.023	0.019	0.014	0.014
13	0.017	0.018	0.010	0.013
14	0.010	0.015	0.007	0.009
15	0.010	0.014	0.011	0.012
16	0.017	0.014	0.018	0.012
17	0.008	0.013	0.007	0.011
18	0.014	0.014	0.015	0.011
19	0.007	0.010	0.011	0.011
20	0.016	0.013	0.007	0.009
21	0.015	0.011	0.017	0.014
22	0.010	0.007	0.009	0.006
23	0.010	0.005	0.006	0.008
24	0.003	0.006	0.010	0.005
25	0.003	0.005	0.007	0.006
26	0.003	0.007	0.003	0.007
27	0.002	0.004	0.004	0.004
28	0.024	0.031	0.025	0.033

Table 10. Alligator Cracking Area Percentage and Transverse Cracking Length Measurements

Site ID	Alligator Cracking Area Percentage (%)		Transverse Cracking Length (m/km)	
	Ground Measure	Orthophoto Measure	Ground Measure	Orthophoto Measure
1	10	10	638	660
2	5	5	728	783
3	5	5	606	589
4	15	15	1326	1290
5	5	10	1395	1410
6	25	20	1032	1064
7	20	25	774	766
8	20	20	1113	1098
9	15	10	1136	1148
10	25	25	653	632
11	20	20	814	771
12	35	35	1141	1121
13	30	30	1145	1212
14	25	25	1186	1136
15	20	25	859	905
16	45	45	1219	1256
17	25	25	649	682
18	30	30	839	815
19	25	25	1135	1102
20	25	25	958	978
21	15	15	665	683
22	5	5	264	280
23	5	5	369	359
24	5	10	175	202
25	10	10	248	284
26	10	10	263	290
27	0	0	0	0
28	35	35	534	500

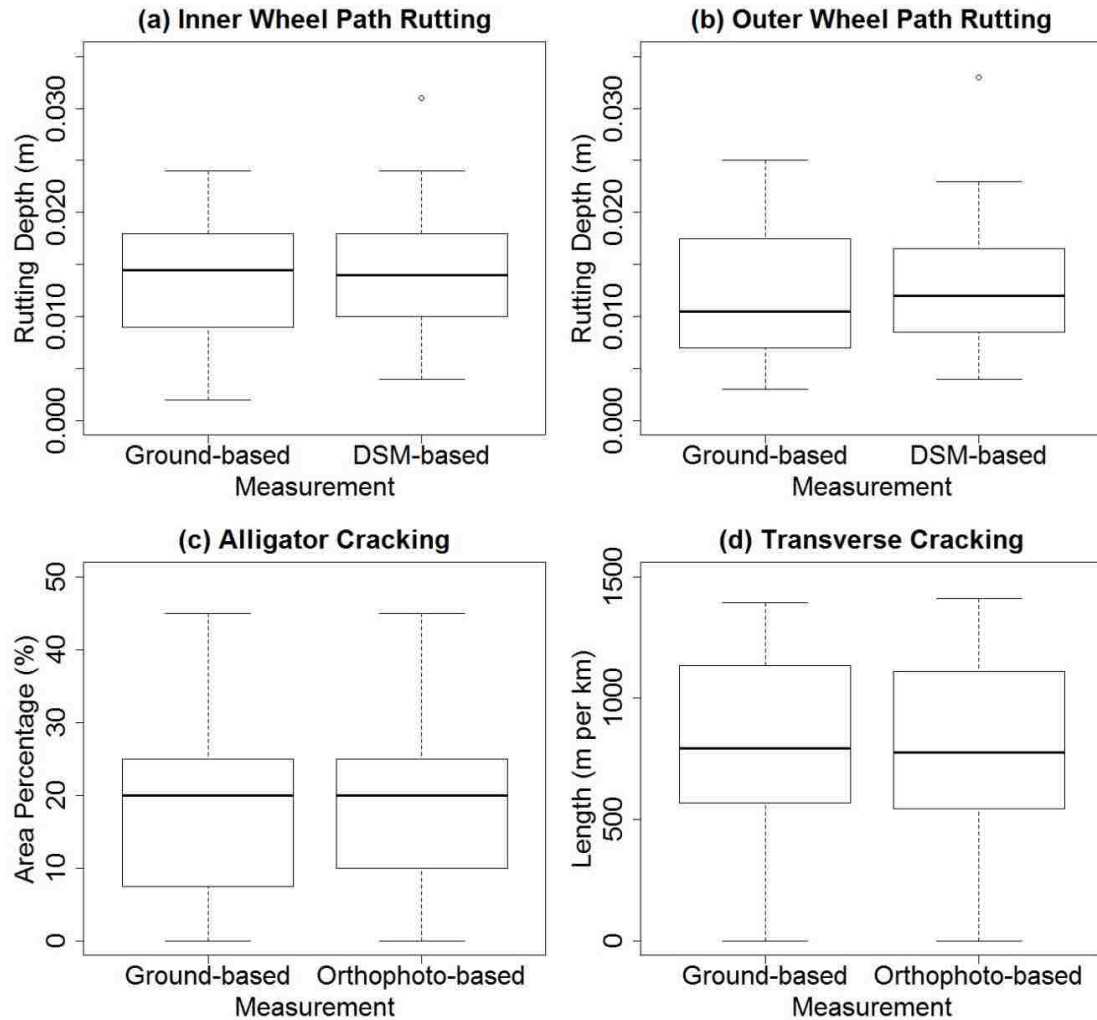


Figure 15. Box plot for each set of measurement. In each quadrant, the two boxes are ground-based measurement and HSR-AP derived products based measurement, respectively. (a) Inner wheel path rutting depth measurement; (b) outer wheel path rutting depth measurement; (c) alligator cracking area percentage measurement; (d) transverse cracking length measurement. The uppermost bar is the maximum measurement value, while the lowermost bar is the minimum measurement value. The bar inside of the box indicates the median. The dots in (a) and (b) indicate measurement outliers.

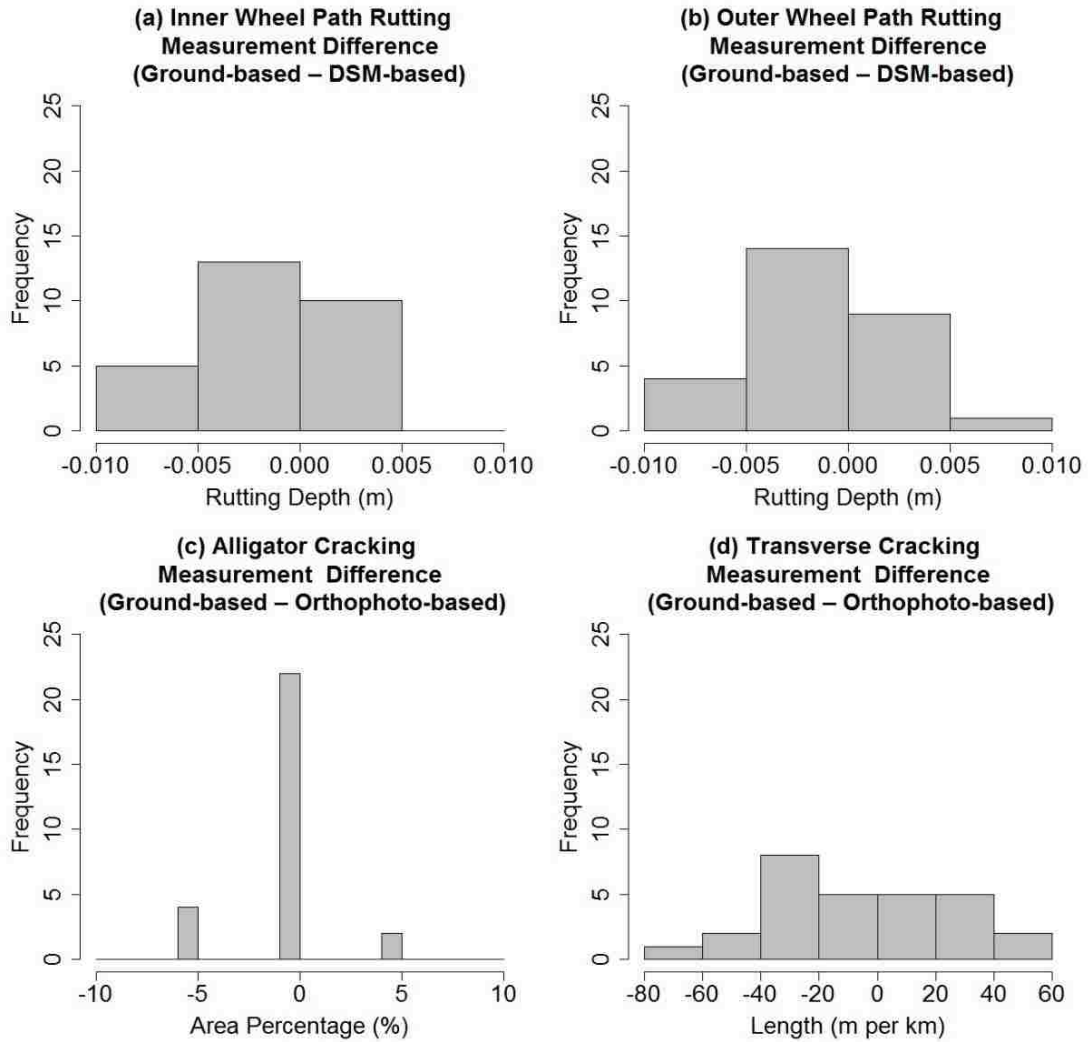


Figure 16. The frequency distribution of each distress' measurement differences (residuals); measurement difference is defined as the difference between ground-based measurement and HSR-AP derived products based measurement. (a) Inner wheel path rutting depth measurement difference; (b) outer wheel path rutting depth measurement difference; (c) alligator cracking area percentage measurement difference; (d) transverse cracking length measurement difference.

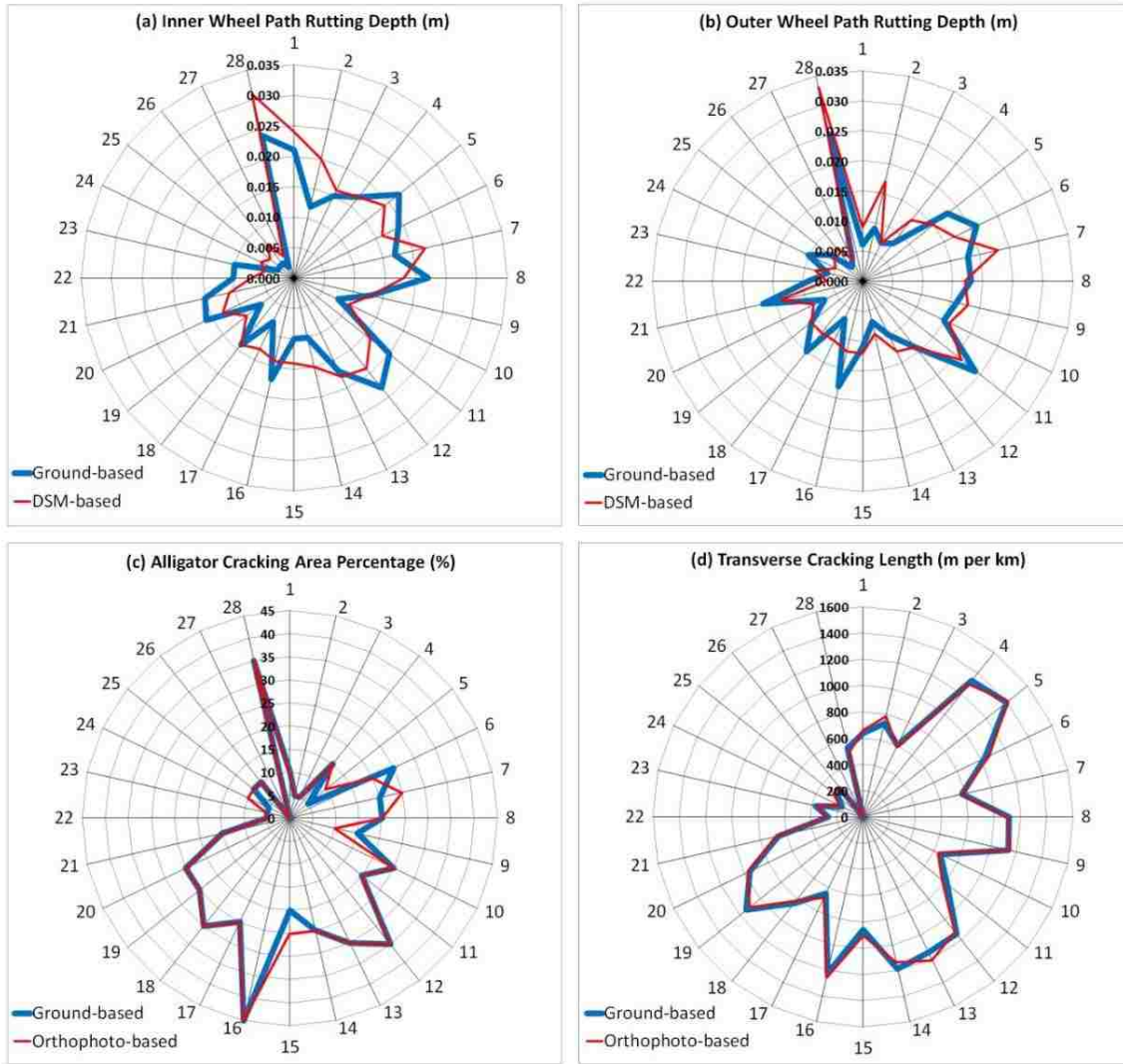


Figure 17. Radar plot for each set of measurement. In each quadrant, the whole numbers (i.e., 1 to 28) adjacent to the outmost ring indicate each of the twenty-eight study sites. (a) Inner wheel path rutting depth measurement, and the decimal numbers adjacent to the multiple-rings indicate rutting depths in m; (b) outer wheel path rutting depth measurement, and the decimal numbers adjacent to the multiple-rings indicate rutting depths in m; (c) alligator cracking area percentage measurement, and the whole numbers adjacent to the multiple-rings indicate alligator cracking area percentages; (d) transverse cracking length measurement, and the whole numbers adjacent to the multiple-rings indicate transverse cracking length in m per km.

Continuing with visual analysis, formal statistical tests were performed. The Wilcoxon Signed Rank test was performed to compare the measurement results of each type of distress at the paired group level. For rutting depth, the test was performed for both the inner wheel path and outer wheel path. For each comparison test, the null hypothesis is that the median difference between each pair of measurements is zero. Test results are summarized in Table 11. For each pair of measurements, p -values are greater than 0.05, and therefore the null hypothesis should be accepted; thereby indicating that for each distress the median difference between the paired ground-based measurement and HySR-DAP derived products based measurement is zero at a 95% confidence interval. In other words, for rutting, alligator cracking, and transverse cracking, ground-based measurements and HySR-DAP derived products based measurements are not statistically different at a 0.05 significance level.

Table 11. Wilcoxon Signed Rank Test Results for Each Distress

Test ID	Distress	Null Hypothesis	p -Value
1	Inner Wheel Path Rutting Depth	The median difference between the two paired measurements (ground-based measurement vs. DSM-based measurement) is zero	0.424
2	Outer Wheel Path Rutting Depth	The median difference between two paired measurements (ground-based measurement vs. DSM-based measurement) is zero	0.541
3	Alligator Cracking Area Percentage	The median difference between two paired measurements (ground-based measurement vs. orthophoto-based measurement) is zero	0.688
4	Transverse Cracking Length	The median difference between two paired measurements (ground-based measurement vs. orthophoto-based measurement) is zero	0.701

The Mann-Whitney U test was performed to compare the measurement results of each distress unpaired, as a group. For rutting depth, the test was again performed for both the inner wheel path and outer wheel path. Although the Mann-Whitney U test does not require normally distributed data, it does not mean that it is assumption free. For the Mann-Whitney U test, data from each population must be an independent random sample, and the population must have equal variances. For non-normally distributed data, the Levene's test and Barlett's test are usually adopted to determine variance equability.

For the Levene's test and the Barlett's test, the null hypothesis is that the population variances are equal. Test results are summarized in Table 12. For each comparison, the *p*-value is greater than 0.05, and therefore the null hypothesis should be accepted; thereby indicating that the population variances for each pair of comparisons are equal at a 95% confidence interval. Therefore, the Mann-Whitney U test is appropriate for all metrics.

Table 12. Levene's Test and Bartlett's Test Results

Distress	Comparison	Null Hypothesis	Variance Test <i>p</i> -Value	
			Levene's Test	Bartlett's Test
Inner Wheel Path Rutting Depth	Ground-based Measure vs. DSM-based Measure	Population variances are equal	0.481	0.832
Outer Wheel Path Rutting Depth	Ground-based Measure vs. DSM-based Measure	Population variances are equal	0.546	0.866
Alligator Cracking Area Percentage	Ground-based Measure vs. DSM-based Measure	Population variances are equal	0.987	0.929
Transverse Cracking Length	Ground-based Measure vs. DSM-based Measure	Population variances are equal	0.946	0.962

For each of the Mann-Whitney U tests, the null hypothesis is that there is no difference in the distribution (shape and spread) of ground-based measurement and HSR-AP derived products based measurement. For all tests, the null hypothesis was retained, meaning that there is no significant difference in the distribution pattern (Table 13) at a 95% confidence interval.

Table 13. Mann-Whitney U Test for Each Distress

Test ID	Distress	Null Hypothesis	<i>p</i> -Value
1	Inner Wheel Path Rutting Depth	The distribution pattern (shape and spread) of measurement values for ground-based measure vs. DSM-based measure is the same	0.850
2	Outer Wheel Path Rutting Depth	The distribution pattern (shape and spread) of measurement values for ground-based measure vs. DSM-based measure is the same	0.786
3	Alligator Cracking Area Percentage	The distribution pattern (shape and spread) of measurement values for ground-based measure vs. orthophoto-based measure is the same	0.855
4	Transverse Cracking Length	The distribution pattern (shape and spread) of measurement values for ground-based measure vs. orthophoto-based measure is the same	0.948

4.4 Discussion

Formal statistical test results revealed that there is no evidence showing that detailed pavement surface distress (i.e., rutting, alligator cracking, and transverse cracking) rates measured from HySR-AP derived products and distress rates manually measured on the ground using standard protocols are statistically different at a 0.05 significance level. Visual comparison of the results supports this finding. Ultimately, these results show that orthophotos and DSMs generated from HySR-DAP acquired from S-UAS can be

effectively used to characterize detailed pavement surface distress that is comparable to ground-based manual measurement.

It should be noted that current manual evaluation methods operationally used by transportation management agencies rely on only visual observation to estimate distress rates (e.g., estimate the length of the cracks), which is highly subjective (Bogus et al. 2010). However, inspectors of this research physically measured the distress rates to collect ground reference data, which is objective. When using the on-screen analysis and digitization to detect and assess distress, the inspectors did not digitize a crack unless it exists and the inspectors were able to identify it, which is also objective. Given the horizontal and vertical accuracy (RMSE = 4 mm and 7 mm, respectively) of the orthophotos and DSMs, the discrepancy between the ground-based manual measurement method and the HSR-AP method could be from either method. This is because distress measurements made by inspectors involves random errors which cannot be avoided (Reichenbacher and Einax 2011; Fridman 2011).

Further investigation of the measurements for each type of distress revealed a more detailed pattern. For the inner and outer wheel path rutting depth, DSM-based measurements are generally higher than ground-based measurements, with 15 sites showing higher DSM-based rutting depth and only ten sites exhibiting higher ground-based rutting depth. The measured vertical accuracy (RMSE = 7 mm) of the DSMs can be interpreted as an indication that much of the discrepancy between the two methods is likely a product of variability in the reconstructed DSMs. This also indicates that DSM-based measurement has a tendency to overestimate rutting depth. Increasing the vertical

accuracy of DSMs may be able to reduce the variability in the reconstructed DSMs, and ultimately reduce the variability in rutting depth measurement.

For alligator cracking area percentage, 22 sites have equal orthophoto-based measurements and ground-based measurements. For transverse cracking, the percent difference between orthophoto-based measurements and ground-based measurements for 20 sites are less than 5%. The measured horizontal accuracy (RMSE = 4 mm) of the orthophotos can be interpreted as an indication that much of the discrepancy between the two methods is likely a product of variability in the field measurements. Field measurement is prone to disturbances originated from traffic, weather conditions, physical conditions, and so on. However, on-screen digitization is not affected by these factors.

Formal statistical test results and visual comparison of results also reveal that discrepancies in the vertical (i.e., rutting) are higher than in the horizontal (i.e., alligator cracking and transverse cracking). However, these results may not indicate that the proposed method works more effectively for characterizing horizontal pavement surface distresses such as cracking. This is because cracking measurements were rounded (for alligator cracking) or normalized (for transverse cracking), which would increase apparent accuracy. In contrast, rutting measurement in the field or on DSMs was error prone, which would decrease apparent accuracy.

Although the novel aspect of this research lies in evaluating whether HSR-AP acquired from S-UAS can be used to characterize detailed pavement surface distress conditions, the remote sensing techniques and methods (e.g., S-UAS based hyper-spatial resolution imaging, SfM, and digitization) associated with this research are readily

deployable for detailed pavement surface condition assessment once restrictions on S-UAS operations are lifted. SfM enabled AT to leverage graphic processing units to permit the generation of tightly co-registered orthophotos and DSMs from large HSR aerial image sets. Collectively, these techniques enabled the 3D characterization of pavement surfaces at unprecedented millimeter scales. In a broader context, the proposed method can be used for myriad other infrastructure condition inspection tasks. These results can be replicated by researchers or practitioners from the infrastructure management and asset management communities to assess whether HySR-DAP acquired from S-UAS can be used to characterize their managed infrastructure or assets such as oil and gas pipelines, bridges, and dams.

Although detailed pavement surface distress conditions are detected and assessed through manual digitizing, it is actually less labor-intensive, less expensive, and more accurate when compared with operationally used ground-based manual observation. The physical and financial requirements for digitization are less than for ground-based manual observation. This is because inspectors are not required to drive to the evaluation destination and walk or drive along the roadways to perform inspection. When inspectors are conducting ground-based physical measurement, at least three people are required because one of them is designated as the safety spotter (inspectors do not have the authority to stop the traffic) and two of them perform the physical measurements. The time for the three-person crew to complete an evaluation for a pavement section with a size of 8 m by 6 m is approximately 20 minutes. However, evaluating the same pavement section with HySR-DAP derived products will only need one inspector for approximately 10 minutes.

Undeniably, there are costs associated with acquiring HySR-DAP from S-UAS, but the cost of using S-UAS acquired aerial data has been substantially reduced in recent years (Lippitt 2015). In addition, the cost can be reduced by collaborating with various government agencies such as the U.S. Geological Survey (USGS), U.S. Department of Agriculture (USDA), and U.S. Department of Homeland Security (USDHS) because these agencies also need HySR aerial imagery data for their managerial activities. Long-term archived HySR aerial imagery records also provide transportation management agencies with the capability to identify spatial and temporal patterns of pavement surface distress conditions from a primary record. It should also be noted that high costs cannot prevent a method from deployment if it has other advantages. For example, New Mexico Department of Transportation (NMDOT) had been using visual observation methods to annually evaluate their 12,500 miles of roadways for many years at an annual cost of approximately \$720,000. However, recently NMDOT adopted survey vehicle-based automated evaluation methods and the annual cost jumped to approximately \$2,100,000 (Montoya and Mann 2015).

More importantly, manual digitization is much more accurate than currently adopted manual observation methods which are based on only subjective judgement (no physical measurement). Formal statistical test results reveal that HySR-DAP derived products based measurements are comparable to ground-based measurements. For this research, inspectors performed physical measurements to ensure consistent and reliable measures of distress on which to evaluate the efficacy of HySR-DAP derived measures.

Even if the proposed methods are readily deployable, the next logical step is automating the extraction of pavement surface distress metrics given the data quantities

involved (Lippitt 2015). Automation will reduce the cost of scaled operational deployment as the U.S. Federal Aviation Administration (FAA) establishes regulations and clears restrictions for S-UAS work in the near future. One potential approach to automate the extraction of alligator cracking and transverse cracking is geographic object-based image analysis (GEOBIA) methods (Blaschke 2010). One potential approach to automate the extraction of rutting depth is having digitized wheel path polygons stored in a GIS database and then routinely monitoring their height change by comparing DSMs acquired at different times (e.g., yearly). Nevertheless, significant algorithm development will be required for both potential approaches, especially for cracking detection and assessment. It might be comparatively easy to identify transverse cracking, but the path to computational rules defining alligator cracking is less clear. For example, according to the HPMS manual, longitudinal cracking should be considered alligator cracking if it occurs in inner or outer wheel paths.

To summarize, S-UAS based hyper-spatial resolution imaging and AT techniques can be used to provide detailed and reliable primary observations suitable for characterizing detailed pavement surface distress conditions, which lays the foundation for the future application of these techniques for automated detection and assessment of detailed pavement surface distress conditions. Operationally HySR-DAP based pavement surface evaluation could be implemented as a service internally by transportation agencies or implemented through consulting firms. Eventually the extraction of distress metrics from HySR-DAP should be automated to enable cost effective scaling of S-UAS based asset management, requiring end users (i.e., federal, state, or local transportation

management agencies) only to design a flight plan and select the distresses to be evaluated, with all other processes being automated.

4.5 Conclusions

This research evaluated whether HySR-DAP acquired from S-UAS can be used to characterize detailed roadway pavement surface distress conditions. Research results indicate that using HySR-DAP acquired from S-UAS as input, AT can be used to generate millimeter scale orthophotos and DSMs and these products can be effectively used to characterize detailed pavement surface distresses comparable to ground-based manual measurement. This finding lays the foundation for future research into automated pavement surface distress detection and assessment by demonstrating that HySR-DAP has the capability to provide accurate and reliable information to characterize detailed pavement surface distress conditions; automation is the logical next step. In recent years, many other sensors such as thermal infrared (TIR) and LiDAR are becoming commercially available in miniaturized forms suitable for operation on S-UAS. Many of these sensors, while more expensive per sensor, have the potential to improve detailed pavement surface distress evaluation. In the near term, the proposed digitization method could be used to measure pavement surface distress conditions in situations where field inspectors cannot evaluate without considerable labor costs (e.g., sections in remote areas) or where survey vehicles cannot gain access; however, in the long term, the proposed method is capable of completely replacing field pavement surface distress evaluation due to its high accuracy, potential for full automation, and the potential to dramatically reduce long-term cost.

Chapter 5 Estimating Pavement Surface Distress Conditions with Geospatial Modeling

5.1 Introduction

Routine evaluation of pavement surface distress condition, which makes up a substantial portion of road maintenance budgets, represents a substantial challenge to transportation management agencies at all levels (i.e. federal, state, and local). Every year they need to evaluate myriad pavement sections distributed over vast geographic areas. For example, the New Mexico Department of Transportation (NMDOT) routinely evaluates pavement surface distress conditions for approximately 12,500 centerline miles of highways.

Currently, two methods are operationally used for inspecting pavement surface distress conditions: manual evaluation and automated evaluation. Manual evaluation involves with trained inspectors visually inspect the surface conditions with subjective judgment while walking or riding (Kim et al. 2006). Automated evaluation is implemented by using vehicle-mounted electronic sensors (e.g. video cameras, digital cameras, and laser sensors) to acquire fine enough resolution images to analyze them automatically to produce evaluation results (Zhang et al. 2016). Both manual and automated evaluation methods have strengths and weaknesses (McGhee 2004; Bogus et al. 2010; Schnebele et al. 2015; Zhang et al. 2015). However, they have two weaknesses in common: time-consuming and expensive. This is because both manual and automated evaluation methods are conceptually rooted in the principle that “exist then survey”. That being said, both manual and automated evaluation methods aim at surveying (not

inferring) each individual pavement section to create a complete and comprehensive condition dataset (Haas et al. 1994).

In the real world, it is not always possible to collect exhaustive data every desired point because of practical, technical, and economical constraints (Bolstad 2005). However, accurate, complete, and prompt evaluation of pavement surface distress is extremely important for effective management of the roadway network (Haas et al. 1994). In order to reduce the amount of work, time, and money associated with pavement surface distress condition evaluation and at the same time achieve a high level of accuracy and completeness, modeling might be one the efficient options.

Modeling pavement surface distress condition is conceptually rooted in the principle that the occurrences of events are limited in spatial distribution (Strickland 2015). That being said, occurrences of events are neither uniform nor random in distribution – there are factors (e.g., socioeconomic factors) constrain and influence where events or processes will occur (Brown et al. 2004). In the context of road pavement, the degradation is also neither uniform nor random in distribution; various factors influence the occurrences of degraded pavement sections (Hartgen et al. 2014). When taking into account the influence of factors known to affect pavement degradation, it is possible to infer pavement surface distress condition which allows the amount of survey sites to be reduced and/or targeted.

Many transportation management agencies have developed a variety of pavement performance models for use in their pavement management activities. According to Lytton (1987), these models can be classified into three categories, including primary response models, structural performance models, and functional performance models.

Primary response models are used to can predict primary response of pavement to a specific factor such as traffic loads. Structural performance models are used to predict pavement structural capacity. Functional performance models are used to predict pavement's functionality such as pavement surface friction, wet-weather safety index, and so on. This research focuses on modeling overall pavement surface conditions which follows in this functional performance model category.

Previous studies on modeling overall pavement surface distress condition are limited. Several studies (e.g. Lou et al. 2001; Terzi 2007; Owolabi et al. 2012) applied modeling techniques (neural network model, linear regression model, fuzzy system mode, artificial intelligence neural network model, and cluster-based model) to predict roadway pavement surface distress condition. However, most of these studies concentrate on predicting pavement surface distress condition without considering geospatial data. Some of these studies (Attoh-Okine 2001; Al-Kheteeb et al. 2011) used a list of limited environmental factors (e.g. temperature) as independent variables for modeling individual pavement surface distresses (e.g. alligator cracking).

A comprehensive literature review reveals that the use of geospatial data for estimating overall pavement surface condition is lacking and presents a significant gap in the research. This research investigated if overall pavement surface condition could be modeled based on routinely collected and publicly available geospatial data characterizing traffic volumes, environmental conditions, and topography. The research investigated what factors affect overall pavement surface distress condition and how many survey sites are required to produce reasonable results. Linear regression analysis was used to model overall pavement surface conditions. Despite its simplicity, linear

regression is a powerful and the most common tool to define the relationship between a dependent variable and the multiple explanatory variables that determine it (Rawlings et al. 1998).

5.2 Methodology

A multiple linear regression model was selected to model the relationship between overall distress rates (ODRs) for pavement surfaces and explanatory variables characterizing traffic volumes, environmental conditions, and topography. The multiple linear regression model development followed the steps established by Hair et al. (1998).

5.2.1 Data Acquisition and Preparation

Within the state of New Mexico, 11,170 data collection sites were identified for use in this study. The actual evaluation zone for each data collection site covers the rightmost driving lane with a length of one tenth of a mile (528 ft or 0.16 km) from a given milepost. A point geographic information system (GIS) database obtained from the Earth Data Analysis Center (EDAC) at the University of New Mexico (UNM) provides the roadway number, milepost number, and roadway direction for each milepost (Figure 18). The locations of these mileposts in Figure 18 also indicate the locations of the data collection sites.

Pavement surface distress condition data were acquired from records of manual pavement evaluations conducted for the NMDOT during the summer of 2009 (Cordova et al. 2009). The reference data are all from flexible pavements (i.e. asphalt concrete or AC pavements), since most of the pavements in New Mexico are of this type. For flexible pavements, when including rutting and shoving distresses, the NMDOT inspects severity

and extent of the following eight distresses on a scale of 0 – 3 (0=Not Present, 1=Low, 2=Medium, and 3=High): 1) Raveling & Weathering; 2) Bleeding; 3) Rutting and Shoving; 4) Longitudinal Cracking; 5) Transverse Cracking; 6) Alligator Cracking; 7); Edge Cracks; 8) Patching. Each data collection site's overall distress rate (ODR) can then be calculated based on the following equation:

$$ODR = \sum_{i=1}^8(\alpha_i \times \beta_i \times \gamma_i) \quad (11)$$

Where i represents each of the eight distresses, α denotes severity rating, β indicates extent rating, and γ represents weighting factor for each type of distress. The weighting factors used by NMDOT for the each of these distresses are 3, 2, 14, 12, 12, 25, 3, and 2, respectively, for each of the eight distresses. The calculated ODR for each of the 11,170 study sites ranges from 0 to 621. The lower the ODR value, the better the pavement condition. The maximum possible value is 657. For this research, ODR was used as the dependent variable.

Explanatory or independent variables were selected thorough literature review (Elbheiry et al. 2011; Adlinge and Gupta 2015) and based upon best available data. These best available data can be classified into three categories: traffic volumes, environmental factors, and topographic factors. Table 14 lists the data and possible explanatory variables that can be extracted from them. Explanatory variables obtained from environmental and topographic data are in the format of digital grid (raster image, Figure 19 to Figure 23) and these values were extracted to each site (milepost) in the acquired GIS milepost database.

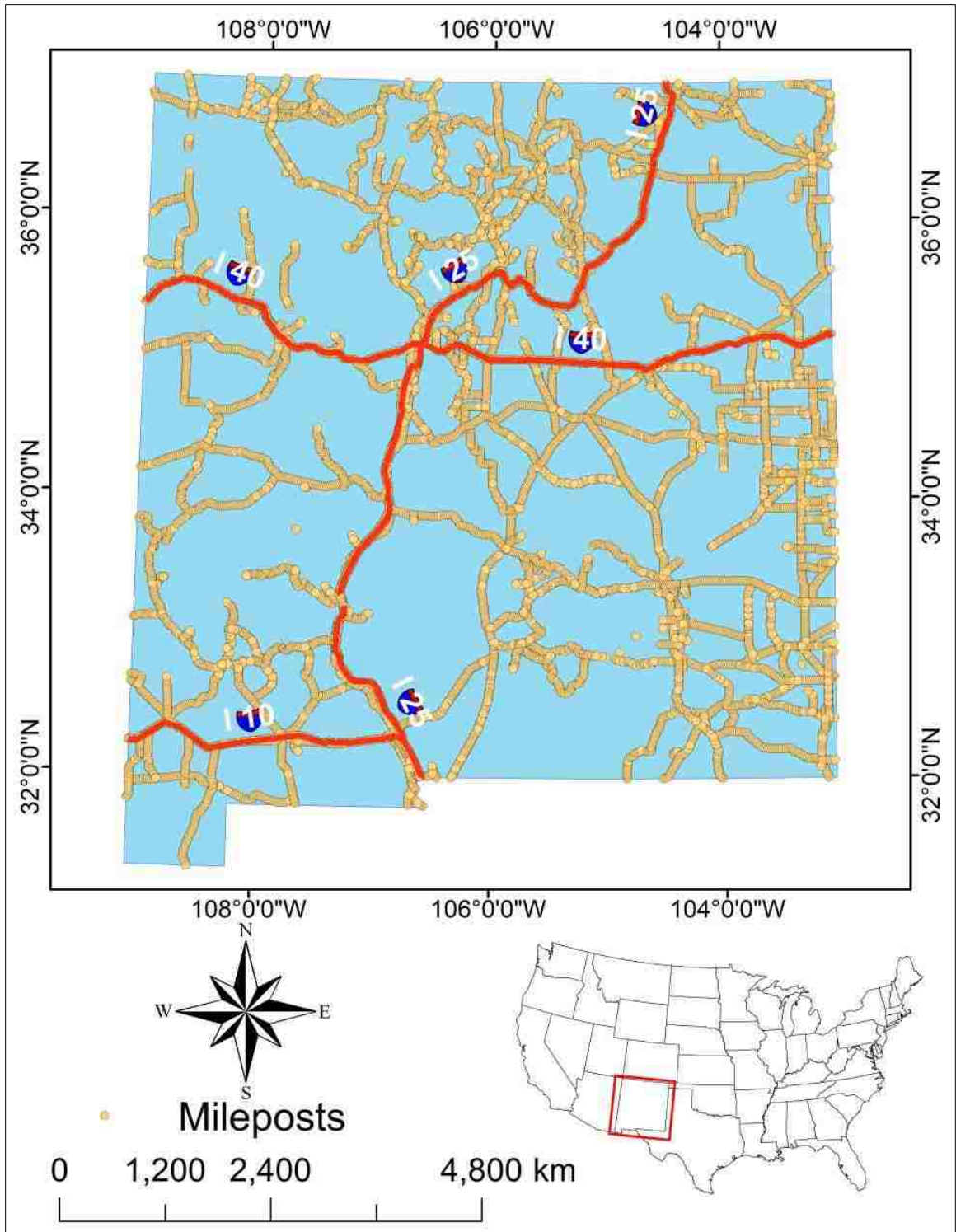


Figure 18. State of New Mexico and locations of surveyed mileposts. The yellow dots indicate the locations of mileposts and the number of total mileposts is 11,170.

Table 14. Best Available Datasets and Extracted Explanatory Variables

Type	Dataset	Year	Source	Extracted Variables
Traffic Volume	Traffic Volume	2005-2009	NMDOT	V ₁ : 2009 AADT; V ₂ : AADT in 5 Years Mean (2006-2009)
	Heavy Vehicle Traffic Volume	2005-2009	NMDOT	V ₃ : 2009 Heavy Vehicle AADT; V ₄ : Heavy Vehicle AADT in 5 Years Mean (2006-2009)
Environmental Conditions	Precipitation	2000-2009	PRISM	V ₅ : 2009 Total Precipitation; V ₆ : 5-year Average Annual Precipitation (2005-2009); V ₇ : 10-year Average Annual Precipitation (2000-2009);
	Average Annual Maximum Temperature (AAMAT)	2000-2009	PRISM	V ₈ : 2009 AAMAT; V ₉ : 5-year AAMAT (2005-2009); V ₁₀ : 10-year AAMAT (2000-2009)
	Average Annual Minimum Temperature (AAMIT)	1999-2009	PRISM	V ₁₁ : 2009 AAMIT; V ₁₂ : 5-year AAMIT (2005-2009); V ₁₃ : 10-year AAMAT (2000-2009);
Topographic Factors	Soil Types	2009	EDAC	V ₁₄ : Soil Type
	Elevation	2009	EDAC	V ₁₅ : Elevation
	Slope	2009	EDAC	V ₁₆ : Slope
	Aspect	2009	EDAC	V ₁₇ : Aspect

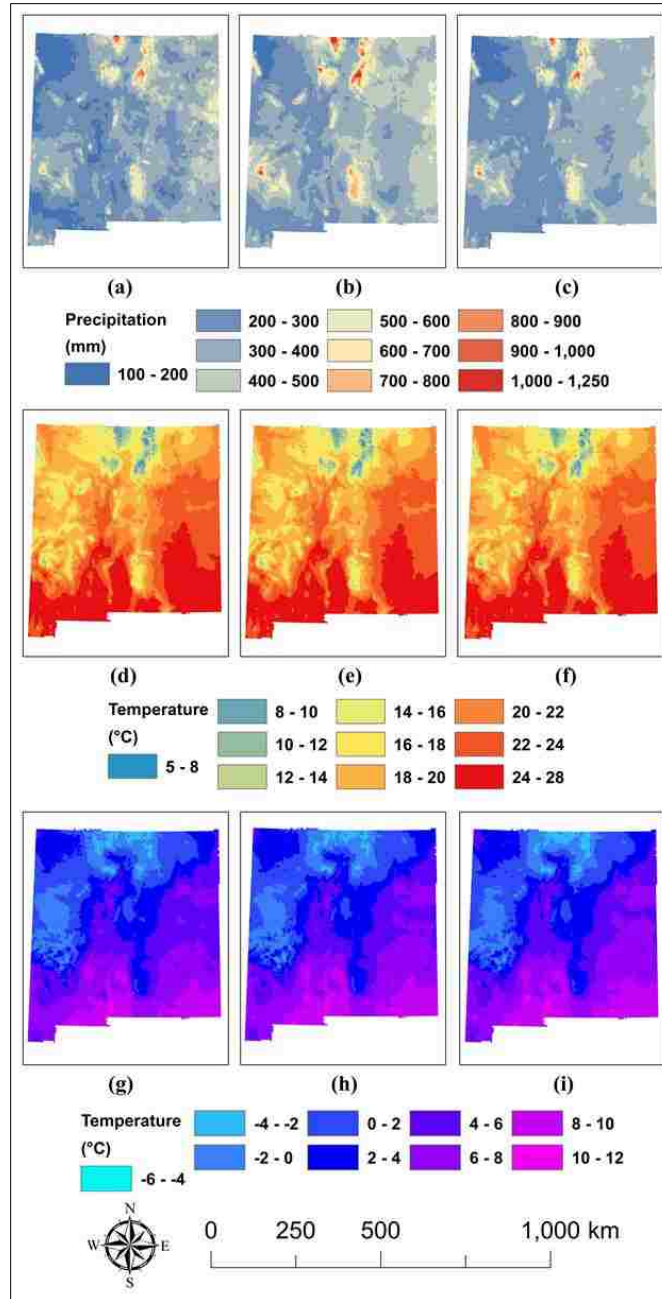


Figure 19. Data characterizing the environmental conditions of the State of New Mexico; AAP indicates average annual precipitation, AAMAT indicates average annual maximum temperature, and AAMIT indicates average annual minimum temperature; (a) shows the total precipitation for the year of 2009; (b) shows the average annual precipitation (AAP) from 2005 to 2009; (c) shows the AAP from 2000 to 2009; (d) shows the average annual maximum temperature (AAMAT) for the year of 2009; (e) shows

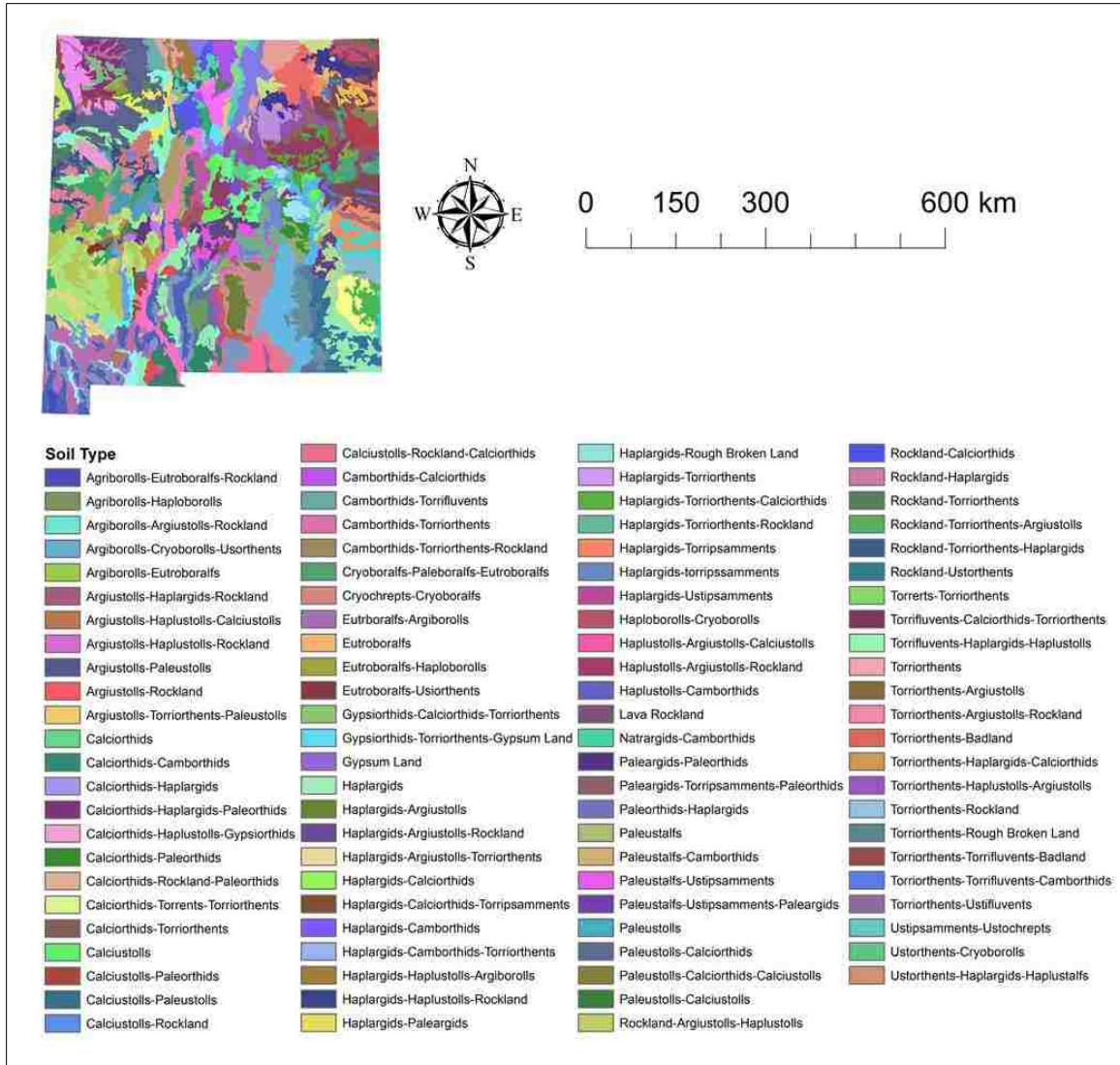


Figure 20. Data characterize the soil types of the State of New Mexico.

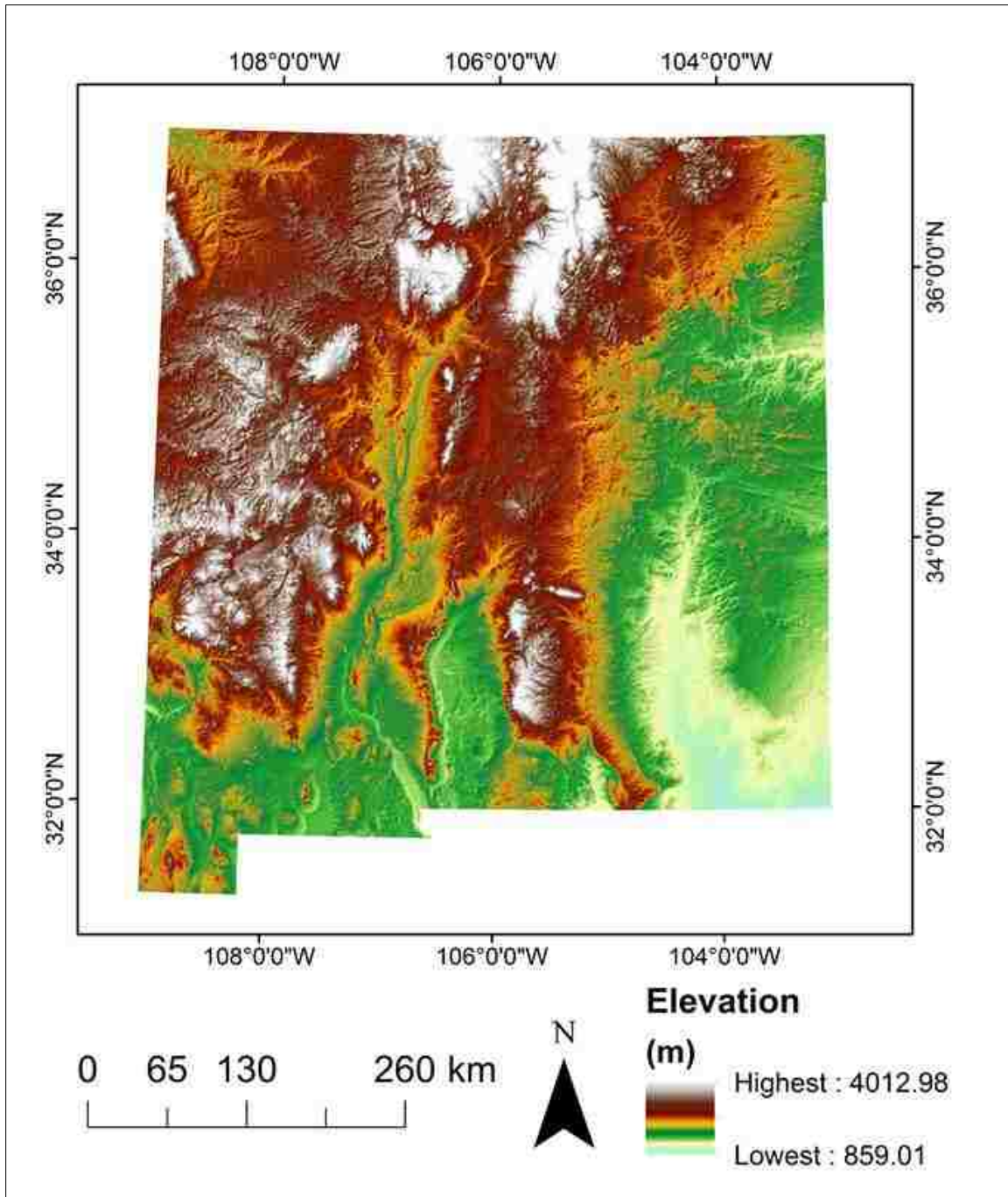


Figure 21. Data show the elevation of the State of New Mexico in shaded relief.

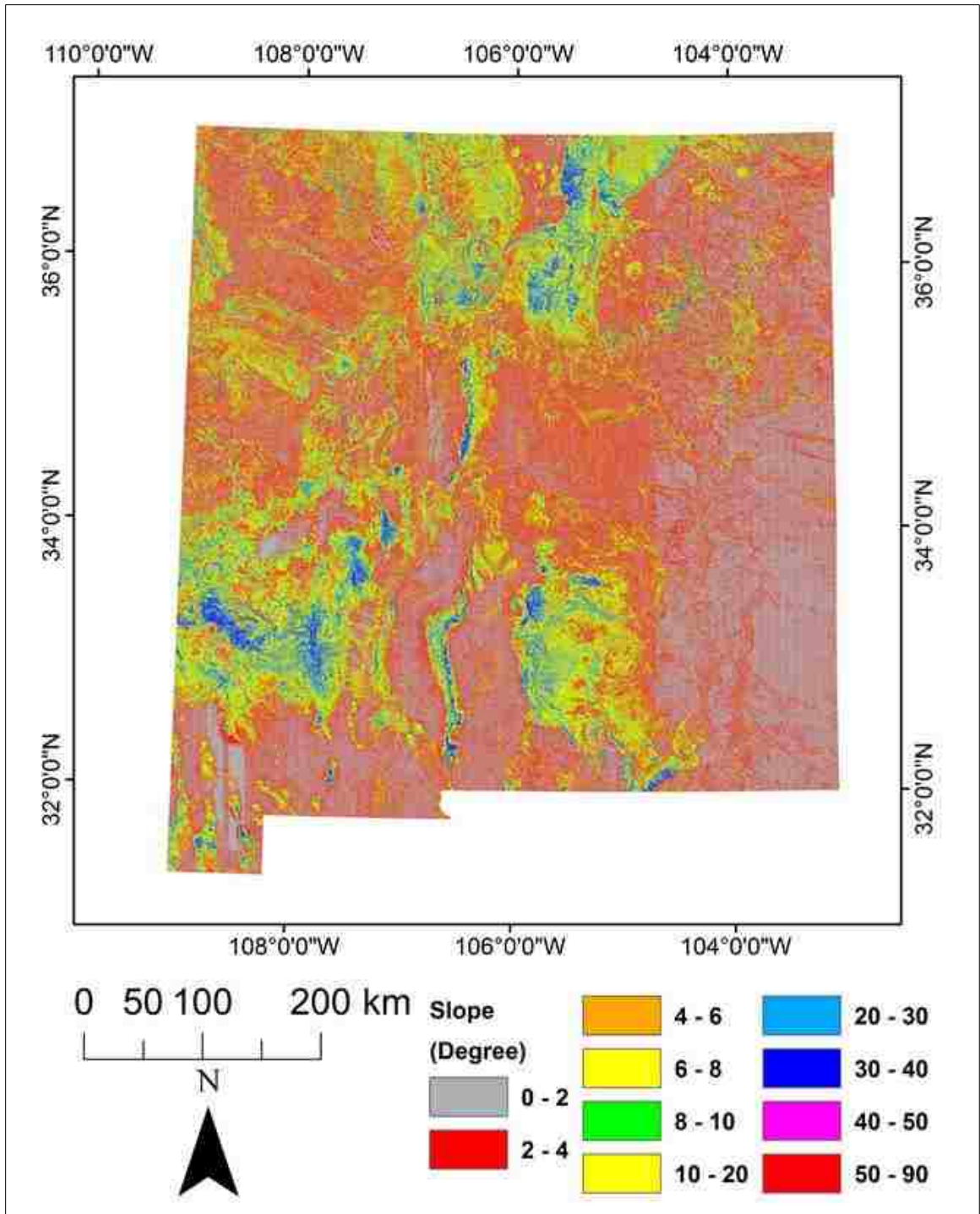


Figure 22. Data show the slope of the State of New Mexico in degrees.

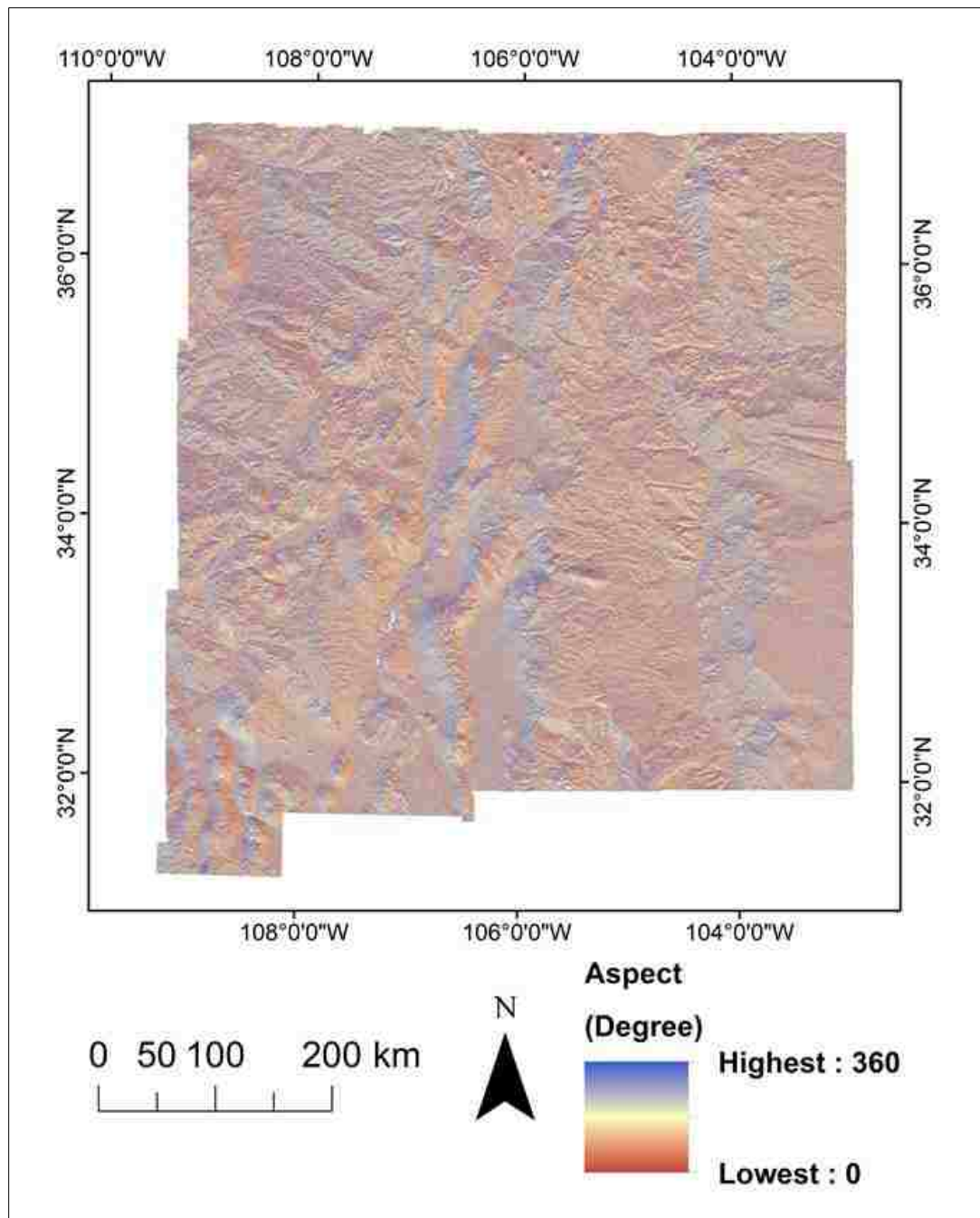


Figure 23. Data show the aspect of the State of New Mexico in degrees.

Traffic volume data were collected by NMDOT at pre-determined locations (milepost) and delivered as a standard annual average daily traffic (AADT). Heavy vehicle traffic volume was considered because heavy trucks typically cause more damages to pavement surfaces than commuting cars (Salama et al. 2006). The Heavy vehicle traffic volume was also collected by NMDOT at the same pre-determined survey sites and delivered as AADT. Traffic volume data were surveyed by NMDOT at pre-determined (~2,500) mileposts and presented as attributes associated with each milepost. To match the spatial coverage of environmental factors and topographic factors, it is necessary to interpolate traffic volume data for unmeasured locations.

5.2.1.1 Traffic Volume Interpolation for Unmeasured Locations

According to Shamo et al. (2015), traffic volume data can be interpolated with spatial interpolation techniques because of their characteristics of spatial distribution and variability. Before interpolating traffic volume for New Mexico, it is necessary to examine if the pre-determined mileposts for the traffic volume survey are spatially autocorrelated. The Global Moran's I test was used to measure the overall clustering of the survey sites. As shown in Table 15, test results revealed that these survey sites are spatially autocorrelated or clustered (p -value < 0.05 and Z score > 0), and, therefore, it is valid to perform interpolation for the traffic volume data within New Mexico from 2005 to 2009.

Table 15. Global Moran's Test for New Mexico Traffic Volume

Year	Moran's I Index	<i>p</i> -Value	Z Score
2005	0.310386	< 0.0001*	55.961373
2006	0.457583	< 0.0001*	54.993811
2007	0.329742	< 0.0001*	57.555267
2008	0.377550	< 0.0001*	22.772707
2009	0.406651	< 0.0001*	21.144202

Note: * indicates significance at $p = 0.05$ level.

There are many spatial interpolation methods, but the three most dominant techniques are inverse distance weighted (IDW), kriging, and spline (Lee and Wong 2011). IDW is one of the most frequently used deterministic models in spatial interpolation. It is based on the assumption that the attribute value of an unsampled point is the weighted average of known values within the neighborhood, and the weights are inversely related to the distances between prediction and the sampled locations (Bolstad 2005). Although IDW is more conceptually intensive, it has the tendency to work better with small datasets and it generally leads to a smoother surface (Zhang et al. 2014). Therefore, IDW was selected as the interpolation method. With IDW, values for unsampled points are estimated by:

$$Z_j = \frac{\sum_i \frac{Z_i}{d_{ij}^n}}{\sum_i \frac{1}{d_{ij}^n}} \quad (12)$$

where Z_j is the estimated value for the unknown point at location j , d_{ij} is the distance from known point i to unknown point j , Z_i is the value for the known point i , and n is a user defined exponent to control how fast a point's influence wanes with distance (Bolstad 2005). According to Zhang et al. (2014), the value 2 is commonly used for n ,

and the search radius for neighboring points is commonly limited to 12. The interpolated grids of traffic value and heavy vehicle traffic volume from 2005 to 2009 are showed in Figure 24 and Figure 25.

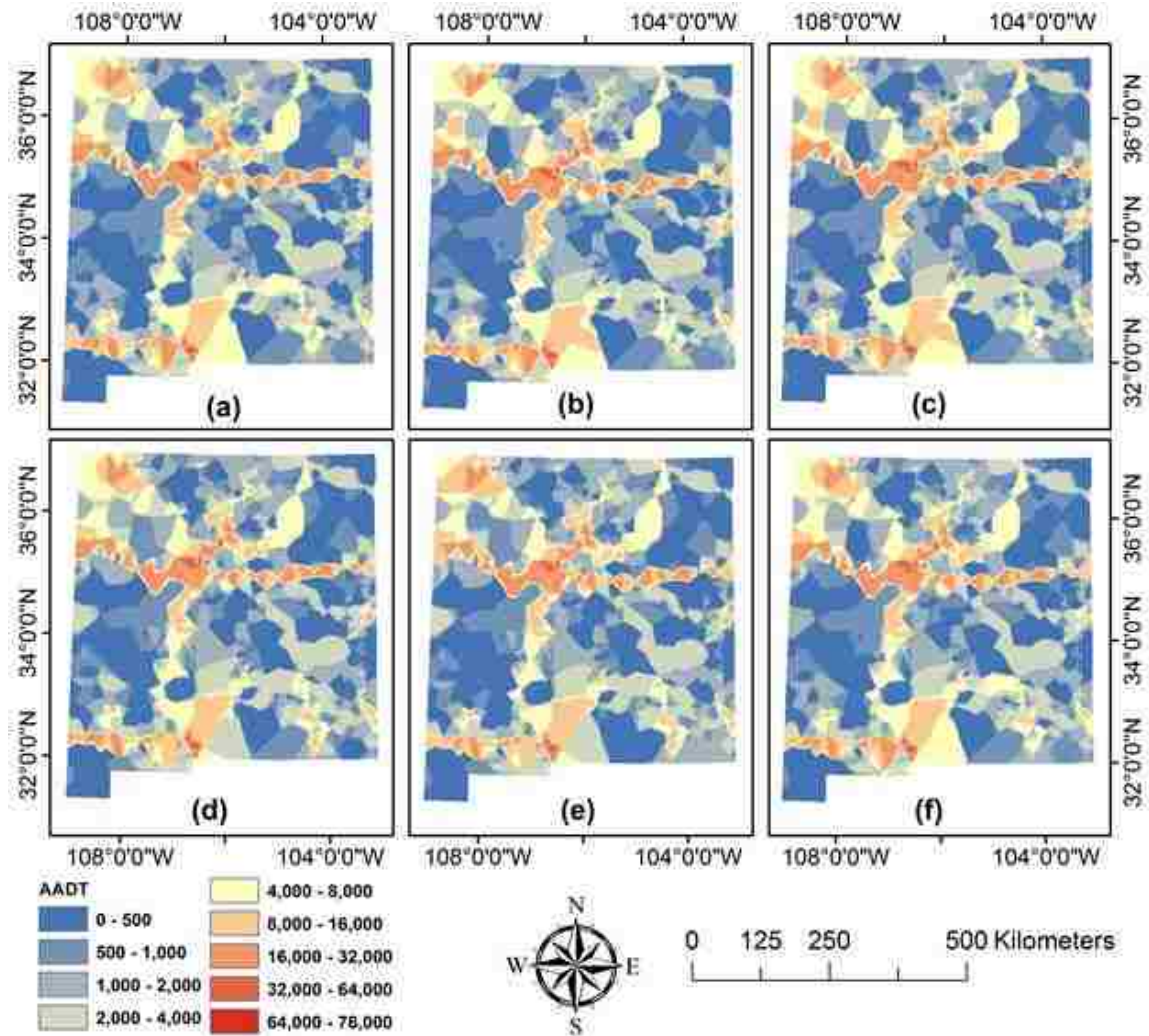


Figure 24. Data characterizing the traffic volume of the State of New Mexico; Inverse distance weighted (IDW) method was used for spatial interpolation; (a) Interpolated AADT for the year of 2005; (b) Interpolated AADT for the year of 2006; (c) Interpolated AADT for the year of 2007; (d) Interpolated AADT for the year of 2008; (e) Interpolated AADT for the year of 2009; (f) Interpolated AADT for 5 years from 2005 to 2009.

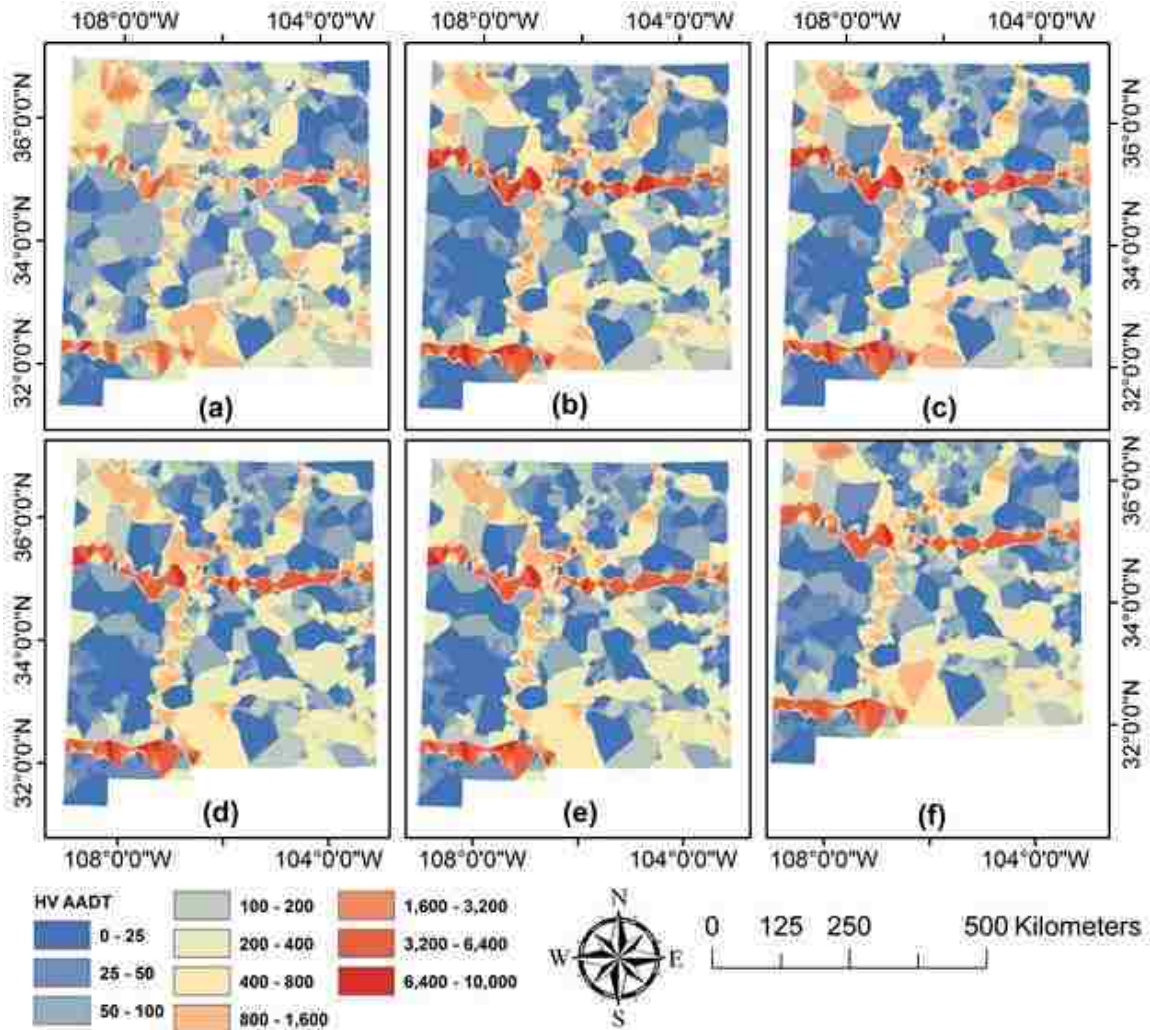


Figure 25. Data characterizing the heavy vehicle traffic volume of the State of New Mexico; HV indicates heavy vehicle; Inverse distance weighted (IDW) method was used for spatial interpolation; (a) Interpolated HV AADT for the year of 2005; (b) Interpolated HV AADT for the year of 2006; (c) Interpolated HV AADT for the year of 2007; (d) Interpolated HV AADT for the year of 2008; (e) Interpolated HV AADT for the year of 2009; (f) Interpolated HV AADT for 5 years from 2005 to 2009.

5.2.1.2 Explanatory Variable Values Extraction

Explanatory variables obtained from traffic factors, environmental factors, and topographic factors are all in digital grid (raster image) format. The values of these digital grids were extracted to each milepost to facilitate modeling.

5.2.2 Model Development

There are 17 explanatory variables and among them 16 variables are continuous data. One variable, soil type, is a categorical data (nominal data). Therefore, the initial model was developed as a general linear model (GLM) because its suitability for both continuous and categorical data. The model is expressed as the following:

$$ODR = \beta_0 + \beta_1 V_1 + \beta_2 V_2 + \dots + \beta_{17} V_{17} \quad (13)$$

Where β_0 represents the intercept parameter, V_1 to V_{17} represent the 17 explanatory variables (see Table 16) and β_1 to β_{17} represent the corresponding coefficients.

In accordance with Hair et al. (1998), Pearson's correlation analysis was used to examine if there is significant correlation among these explanatory variables. It should be noted that V_{14} is categorical data and therefore, its correlation to other explanatory and dependent variables was examined via Spearman's correlation analysis. As shown in Table 16, topographic factors (V_{14} to V_{17}) were weakly correlated (correlation coefficient $< |0.3|$) with ODR. Therefore, they were excluded from the regression. Table 3 also revealed that several explanatory variables (e.g., V_5 , V_6 , V_7) were strongly correlated (correlation coefficient > 0.7) with each other. In other words, there is collinearity among explanatory variables. Among the strongly correlated explanatory variables, only those showing the highest correlation coefficient with dependent variable ODR were used for developing the model. These variables are V_2 , V_3 , V_6 , and V_{11} .

Table 16. Pearson's and Spearman's Correlation Analysis of Explanatory Variables

Variables	ODR	V ₁	V ₂	V ₃	V ₄	V ₅	V ₆	V ₇	V ₈	V ₉	V ₁₀	V ₁₁	V ₁₂	V ₁₃	V ₁₄	V ₁₅	V ₁₆	V ₁₇
ODR	1.000	0.905 (*)	0.905 (*)	0.830 (*)	0.834 (*)	0.878 (*)	0.891 (*)	0.887 (*)	0.751 (*)	0.753 (*)	0.755 (*)	-0.896 (*)	-0.894 (*)	-0.894 (*)	-0.041 (*)	0.124 (*)	0.001	-0.003
V ₁	0.905 (*)	1.000	0.988 (*)	0.686 (*)	0.706 (*)	-0.258 (*)	-0.281 (*)	-0.295 (*)	0.074 (*)	0.082 (*)	0.084 (*)	0.082 (*)	0.086 (*)	0.080 (*)	-0.000	-0.064 (*)	0.001	0.045 (*)
V ₂	0.908 (*)	0.988 (*)	1.000	0.694 (*)	0.720 (*)	-0.262 (*)	-0.283 (*)	-0.299 (*)	0.072 (*)	0.079 (*)	0.082 (*)	0.078 (*)	0.082 (*)	0.076 (*)	-0.001	-0.059 (*)	0.002	0.046 (*)
V ₃	0.830 (*)	0.686 (*)	0.694 (*)	1.000	0.981 (*)	-0.198 (*)	-0.196 (*)	-0.202 (*)	0.114 (*)	0.117 (*)	0.117 (*)	0.087 (*)	0.092 (*)	0.088 (*)	0.019	-0.081 (*)	-0.006	0.025 (*)
V ₄	0.838 (*)	0.706 (*)	0.720 (*)	0.981 (*)	1.000	-0.213 (*)	-0.212 (*)	-0.217 (*)	0.121 (*)	0.124 (*)	0.124 (*)	0.089 (*)	0.093 (*)	0.090 (*)	0.018	-0.085 (*)	-0.006	0.023 (*)
V ₅	0.878 (*)	-0.258 (*)	-0.262 (*)	-0.198 (*)	-0.213 (*)	1.000	0.924 (*)	0.916 (*)	-0.351 (*)	-0.372 (*)	-0.383 (*)	-0.189 (*)	-0.188 (*)	-0.187 (*)	-0.031 (*)	0.239 (*)	0.008	-0.028 (*)
V ₆	0.891 (*)	-0.281 (*)	-0.283 (*)	-0.196 (*)	-0.212 (*)	0.924 (*)	1.000	0.980 (*)	-0.387 (*)	-0.412 (*)	-0.425 (*)	-0.202 (*)	-0.203 (*)	-0.205 (*)	-0.033 (*)	0.305 (*)	0.005	-0.035 (*)
V ₇	0.887 (*)	-0.295 (*)	-0.299 (*)	-0.202 (*)	-0.217 (*)	0.916 (*)	0.980 (*)	1.000	-0.323 (*)	-0.350 (*)	-0.366 (*)	-0.157 (*)	-0.157 (*)	-0.157 (*)	-0.025 (*)	0.232 (*)	0.003	-0.039 (*)
V ₈	0.751 (*)	0.074 (*)	0.072 (*)	0.114 (*)	0.121 (*)	-0.351 (*)	-0.387 (*)	-0.323 (*)	1.000	0.999 (*)	0.997 (*)	0.901 (*)	0.903 (*)	0.908 (*)	0.160 (*)	-0.947 (*)	-0.031 (*)	0.006
V ₉	0.753 (*)	0.082 (*)	0.079 (*)	0.117 (*)	0.124 (*)	-0.372 (*)	-0.412 (*)	-0.350 (*)	0.999 (*)	1.0000	0.999 (*)	0.896 (*)	0.899 (*)	0.904 (*)	0.157 (*)	-0.949 (*)	-0.031 (*)	0.008
V ₁₀	0.755 (*)	0.084 (*)	0.082 (*)	0.117 (*)	0.124 (*)	-0.383 (*)	-0.425 (*)	-0.366 (*)	0.997 (*)	0.999 (*)	1.000	0.892 (*)	0.896 (*)	0.900 (*)	0.155 (*)	-0.947 (*)	-0.031 (*)	0.009
V ₁₁	-0.896 (*)	0.082 (*)	0.078 (*)	0.087 (*)	0.089 (*)	-0.189 (*)	-0.202 (*)	-0.157 (*)	0.901 (*)	0.896 (*)	0.892 (*)	1.000	0.998 (*)	0.995 (*)	0.142 (*)	-0.888 (*)	-0.039 (*)	0.001
V ₁₂	-0.894 (*)	0.086 (*)	0.082 (*)	0.092 (*)	0.093 (*)	-0.188 (*)	-0.203 (*)	-0.157 (*)	0.903 (*)	0.899 (*)	0.896 (*)	0.998 (*)	1.000	0.999 (*)	0.141 (*)	-0.893 (*)	-0.039 (*)	0.001
V ₁₃	-0.894 (*)	0.080 (*)	0.076 (*)	0.088 (*)	0.090 (*)	-0.187 (*)	-0.205 (*)	-0.156 (*)	0.908 (*)	0.904 (*)	0.900 (*)	0.995 (*)	0.999 (*)	1.000	0.142 (*)	-0.904 (*)	-0.037 (*)	0.001
V ₁₄	-0.041 (*)	-0.000 (*)	-0.001 (*)	0.019 (*)	0.018 (*)	-0.031 (*)	-0.033 (*)	-0.025 (*)	0.160 (*)	0.157 (*)	0.155 (*)	0.142 (*)	0.141 (*)	0.142 (*)	1.000	-0.132 (*)	0.394 (*)	-0.003
V ₁₅	0.124 (*)	-0.064 (*)	-0.059 (*)	-0.081 (*)	-0.085 (*)	0.239 (*)	0.305 (*)	0.232 (*)	-0.947 (*)	-0.949 (*)	-0.947 (*)	-0.888 (*)	-0.893 (*)	-0.904 (*)	-0.132 (*)	1.000	0.033 (*)	-0.011
V ₁₆	0.001	0.001	0.002	-0.006	-0.006	0.008	0.005	0.003	-0.031 (*)	-0.031 (*)	-0.031 (*)	-0.039 (*)	-0.039 (*)	-0.037 (*)	0.394 (*)	0.033 (*)	1.000	0.018
V ₁₇	-0.003 (*)	0.045 (*)	0.046 (*)	0.025 (*)	0.023 (*)	-0.028 (*)	-0.035 (*)	-0.039 (*)	0.006	0.008	0.009	0.001	0.001	0.001	-0.003	-0.011	0.018	1.000

Note: * indicates significance at $p = 0.05$ level.

Because all remaining explanatory variables were continuous, multiple linear least squares regression was used because of its suitability for only continuous data. The model can then be expressed as:

$$ODR = \beta_0 + \beta_2 V_2 + \beta_3 V_3 + \beta_6 V_6 + \beta_{11} V_{11} \quad (14)$$

Where β_0 represents the intercept parameter, V_2 , V_3 , V_6 , and V_{11} represent the explanatory variables, and β_2 , β_3 , β_6 , and β_{11} represent the corresponding coefficients.

5.2.3 Model Validation

Among the 11,170 study sites, 10,000 (in-sample) were selected using a random sample stratified by ODR and used to develop the regression model. The remaining 1,170 study sites (out-of-sample) were used to cross-validate the model results. These out-of-sample cross-validation sites are approximately 12% of the in-samples that were used to develop the regression model, which satisfies the population size (5%) requirement for cross-validation (Algina et al. 2000).

The collected ODRs for the cross-validation sites are considered to be actual values, while the model-generated ODRs are considered as the predicted values. Root-mean-squared-error (RMSE) was used to examine if the errors associated with the model is acceptable. RMSE can be calculated as:

$$RMSE = \sqrt{\frac{1}{n} \sum_{i=1}^n (ODR_{p,i} - ODR_{a,i})^2} \quad (15)$$

Where ODR_a represents actual ODR, ODR_p represents predicted ODR, and n represents the number of out-of-sample for cross-validation which is 1,170.

Model performance was evaluated using RMSE and Adjusted R^2 (R^2_{adj}) which provides an additional penalty for increasing model complexity (Chai and Draxler 2014). The index of R^2 supposes that every independent variable in the model explains the variation in the dependent variable and it shows how well observations fit a curve or line. The equation for calculating R^2 is:

$$R^2 = 1 - \frac{\sum_{i=1}^m (ODR_{p,i} - ODR_{a,i})^2}{\sum_{i=1}^m (ODR_{p,i} - \frac{1}{m} \sum_{i=1}^m ODR_{a,i})^2} \quad (5)$$

Where ODR_a represents actual ODR, ODR_p represents predicted ODR, and m represents the number of in-sample for each decrement models. R^2_{adj} is a modified version of R^2 and it not only shows how well observations fit a curve or line, but also adjusts for the number of observations in a model. Therefore, R^2_{adj} is more appropriate for the decrement model comparison. The equation for calculating R^2_{adj} is:

$$R^2_{adj} = 1 - \frac{(1 - R^2)(t - 1)}{t - k - 1} \quad (6)$$

Where t = number of observations, and k = number of explanatory variables.

5.2.4 Determination of the Minimum Number of Survey Sites

The model was developed with 10,000 sample sites, which is approximately the number of sites a state transportation management agency like NMDOT currently collects annually. A 10% decrement modeling method was used to identify a threshold of loss in estimation accuracy. That being said, 9,000 (90% of 10,000) survey sites were used to rebuild the model and then the same cross-validation sites were used to assess the validity. The decrement ended with 1,000 survey sites. The RMSE and R^2_{adj} of the first decrement model were recorded and compared with the ones of the original model and so

on. This iteration was performed ten times until reaching the minimum sample size tested (1,000 survey sites).

5.3 Results and Discussion

Table 17 shows the results of the multiple linear least squares model using all 10,000 study sites. This model is valid at a 95% confidence interval (joint p -value < 0.001). The adjusted R^2 value is 0.9167, and the RMSE is 20.418. This error number is acceptable because the reference ODR obtained from manual evaluation can exhibit an error up to 84 based on variability in measurement (Bogus et al. 2010). Out-of-sample cross-validation revealed that the RMSE obtained from the validation sites was 27.095, which is increased from 20.418, but not substantially. This implied that overall pavement surface conditions can be estimated based on geospatial modeling with the selected traffic, environmental, and topographic factors.

Table 17. Multiple Linear Least Squares Regression Results Using 10,000 Sites

Variables	Coef. (β)	p -value	Adjusted R^2	RMSE	Joint p -value	Validation RMSE
V ₂	0.004	$< 0.0001^*$				
V ₃	0.003	$< 0.0001^*$				
V ₆	0.177	$< 0.0001^*$	0.9080	35.369	$< 0.0001^*$	42.067
V ₁₁	-7.563	$< 0.0001^*$				
Intercept	27.283	$< 0.0001^*$				

Note: Coef. indicates coefficient and * indicates significance at $p = 0.05$ level.

The results of decrement models are shown in Table 18 and Figure 26. The models for iteration 1 to 7 are valid at a 95% confidence interval (adjusted $R^2 > 0.5$ and joint p -value < 0.0001). In addition, the RMSEs for 10,000 to 4,000 in-sample regression and out-of-sample cross-validation are acceptable because they are all less than 84. However, models calibrated based on 3,000 or less samples were not valid (adjusted $R^2 < 0.5$ and joint p -value > 0.05). In addition, the out-of-sample cross-validation results revealed that the RMSEs are not acceptable (> 84). This implies for the State of New Mexico, the minimum number of survey sites required to model ODR with error less than variability in manual inspection is approximately 4,000, which is 40% of the total survey sites. It should be noted that the minimum amount of survey sites might be location-specific. That being said, the amount of 4000 survey sites may only apply to New Mexico. For example, a state that has more centerline miles of highways (compared with New Mexico) may need a minimum of 5,000 survey sites. This proposed method could be replicated by transportation agencies to investigate the minimum amount of survey sites for their states.

All topographic factors (soil type, elevation, slope, and aspect) considered in this research were not significantly correlated with overall pavement surface condition as measured by ODR. This might be because engineering solutions of roadway construction can effectively reduce the influence of topographic factors on pavement surface distress conditions. Traffic volumes, especially heavy vehicle traffic volumes, average annual precipitation, and average minimum temperatures have the most significant influence on pavement surface conditions in New Mexico.

Table 18. Results of the Estimation Models based on Various Number of Samples

Iteration	In-sample Regression			Out-of-sample Validation RMSE	
	Sites	Adjusted R ²	Joint <i>p</i> -value		
1	10,000	0.9080	< 0.0001*	35.369	42.067
2	9,000	0.8598	< 0.0001*	36.623	43.259
3	8,000	0.8152	< 0.0001*	50.964	60.883
4	7,000	0.7937	< 0.0001*	51.863	68.999
5	6,000	0.7742	< 0.0001*	53.491	70.961
6	5,000	0.6632	< 0.0001*	60.852	72.423
7	4,000	0.5142	< 0.0001*	70.951	79.852
8	3,000	0.1319	0.069	95.463	105.290
9	2,000	0.0866	0.826	107.352	127.889
10	1,000	0.0353	0.937	117.159	129.961

Note: * indicates significance at $p = 0.05$ level.

Figure 26 reveals that residuals (the difference between predicted ODR and actual ODR) could occur at any study sites that have ODR values between 0 and 600. One explanation for this is that operationally a pavement section will be repaired or reconstructed rapidly if its condition has impacts traffic safety and driving comfort. Repaired or reconstructed pavement sections will provide much lower ODR values and cause substantially different ODRs than predicted by model, which does not account for these maintenance activities.

Therefore, maintenance records of the pavement sections should be included in future iterations of such a model. Maintenance records were not used in this research due to data limitations (such records were not available). Given the autonomy of state DOTs in the United States, the availability of maintenance records will vary state-to-state.

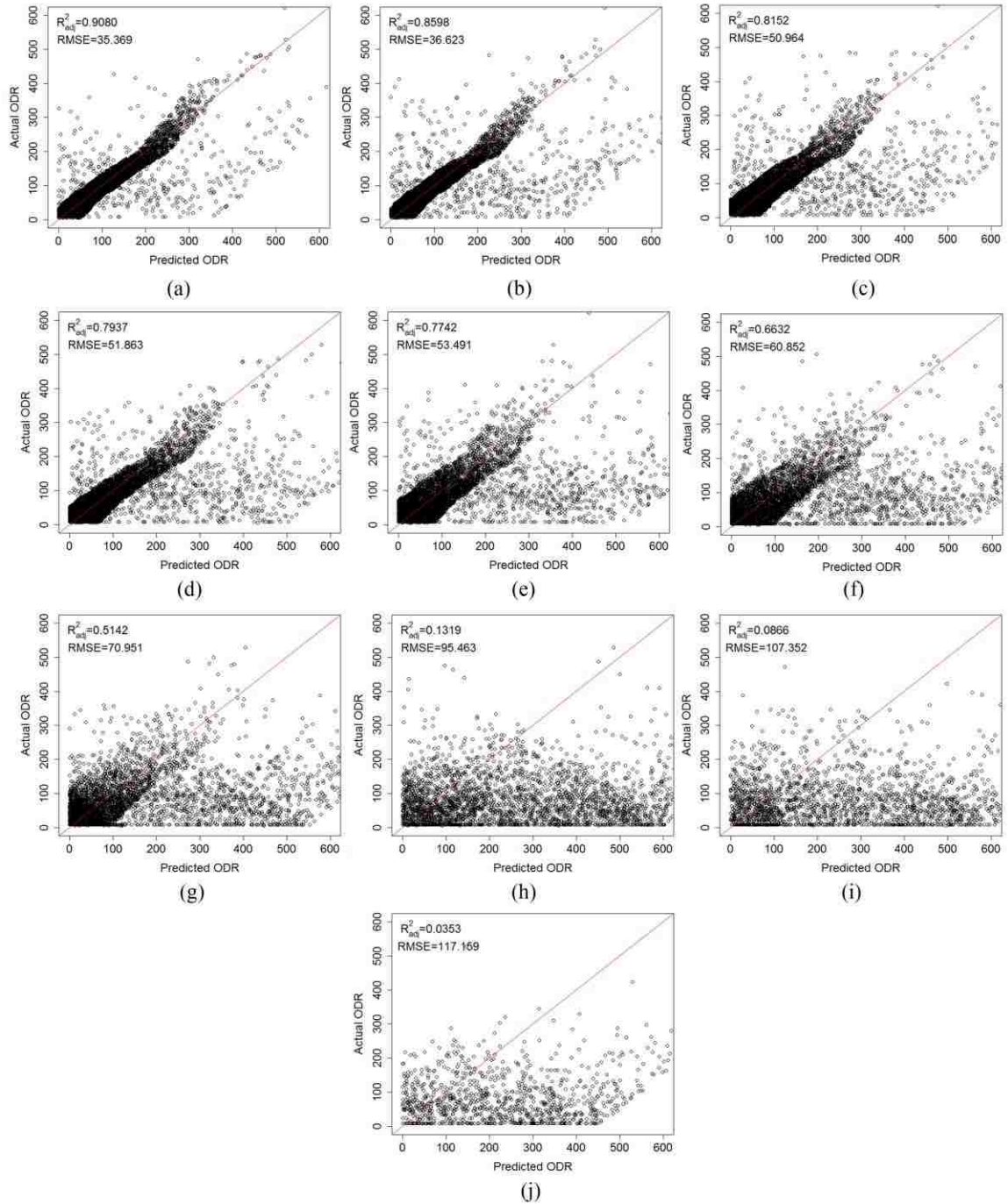


Figure 26. Correlation of predicted ODR versus actual ODR for in-samples regression results; (a) 10,000 in-samples correlation; (b) 9,000 in-samples correlation; (c) 8,000 in-samples correlation; (d) 7,000 in-samples correlation; (e) 6,000 in-samples correlation; (f) 5,000 in-samples correlation; (g) 4,000 in-samples correlation; (h) 3,000 in-samples correlation; (i) 2,000 in-samples correlation; (j) 1,000 in-samples correlation.

According to the Federal Highway Administration (FHWA), it takes approximately 15 years for a flexible pavement surface to drop 50% in quality (Lenz, 2011). Results reveal that factors significantly affect overall pavement surface conditions are all short-term ones. AADT in recent five years (2005 to 2009), heavy vehicle AADT in the same year (2009), average annual precipitation in recent five years (2005 to 2009), and annual minimum temperature in the same year (2009) have the most impact on overall pavement surface conditions.

Figure 27 shows that most residuals of the 10,000 in-sample regression model have absolute values that are less than 35, which is the RMSE for this regression model. Therefore, large residuals are defined as residuals that have absolute values greater than 35. A Global Moran's I test reveals that large residuals are spatially clustered (p -value < 0.0001 and Moran's I index is 0.4292). A further inspection identifies and selects all large residuals and they are shown in Figure 28. The clusters of large residuals exhibit a linear pattern, which is different from other natural phenomena (e.g., precipitation and temperature). This linear clustering pattern may be related to construction performance. This is because typically a certain length of roadways are constructed or maintained by the same contractor. Therefore, construction performance should also be considered in future model improvement. This factor was not considered in these models because of a lack of data maintained by NMDOT. Re-examining Figure 26 reveals that most large residuals are positive, indicating that the developed models have a tendency to overestimate the surface distress of pavement sections. Figure 28 also suggests that a large portion of the large residuals are located at the border of New Mexico and Colorado, where well-maintained record of data (e.g., traffic volume) may do not exist.

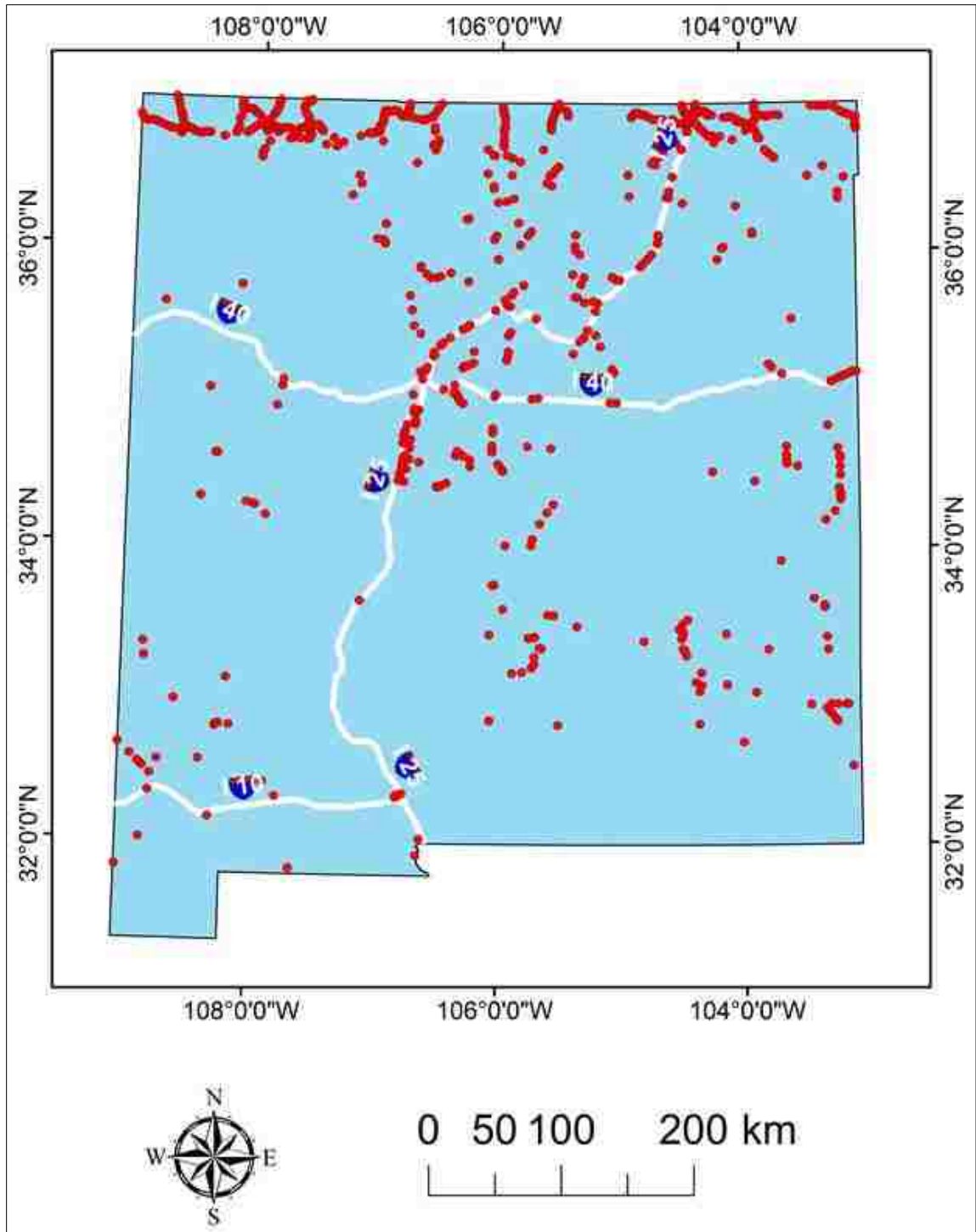


Figure 27. The distribution pattern of large residuals with a value greater than 35 or less than -35, which is the RMSE of the 10,000 in-sample regression; residual is defined as the difference between predicted ODR and actual ODR; Global Moran's I test shows the p -value is less than 0.0001 and the Moran's I is 0.4292, meaning the large residuals are spatially autocorrelated.

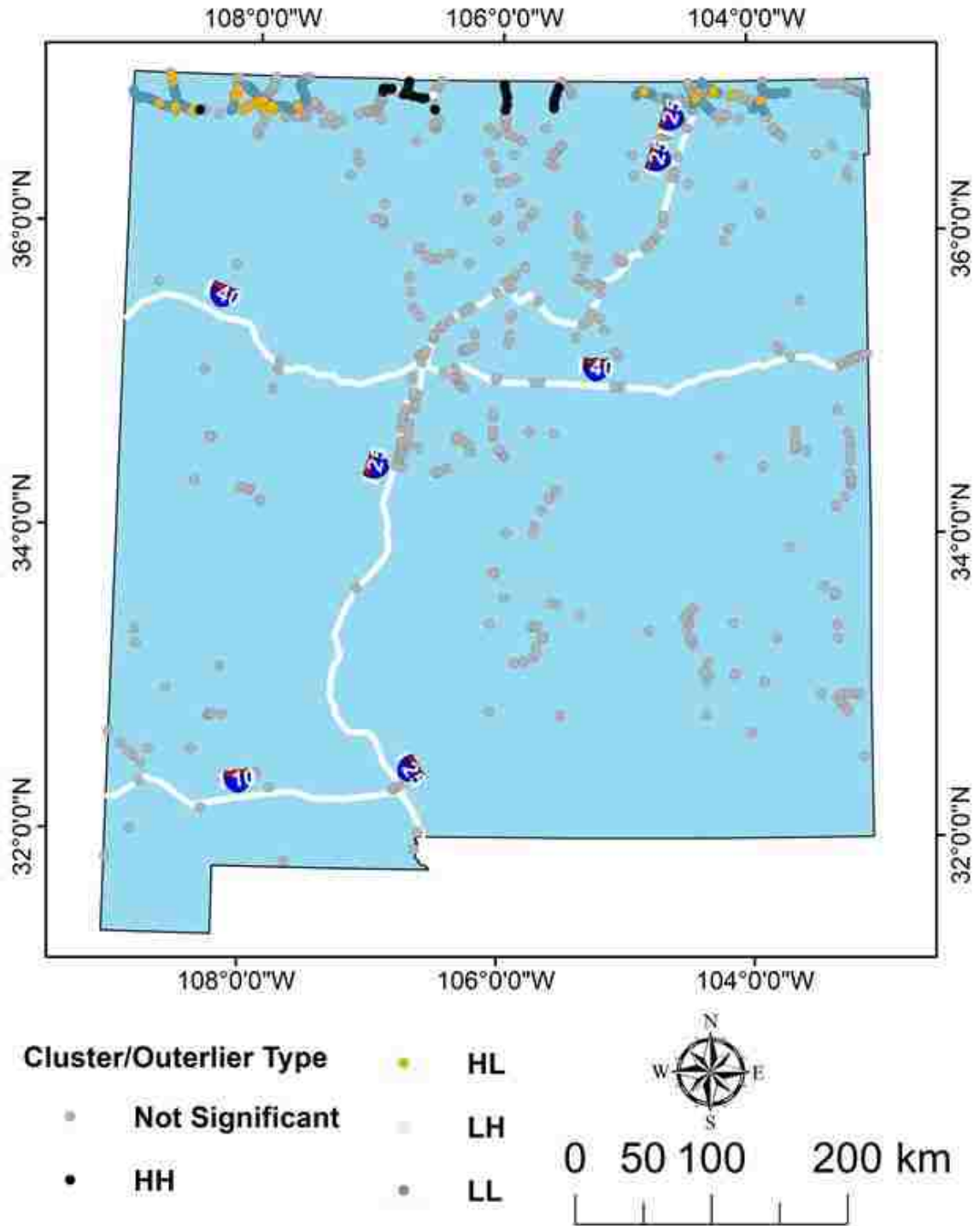


Figure 28. Anselin Local Moran's I test results. HH indicates high values are surrounded by high values at a 95% confidence interval; LL means low values are surrounded by low values at a 95% confidence interval; HL indicates high values are surrounded by low values, while LH indicates low values are surrounded by high values.

One major limitation of Global Moran's I test is that it tends to average local variations in the strength of spatial autocorrelation. Therefore, Anselin Local Moran's I test, which examines the local level of spatial autocorrelation, was used to identify locations where values of the variable are both extreme and geographically homogeneous. Figure 28 reveals that large residuals in northern New Mexico are locally clustered. Northern New Mexico has more mountainous terrain with large temperature and precipitation variations compared to central and southern New Mexico, and therefore, this may provide intervention to the models. This locally clustered pattern might also be caused by recent repair or reconstruction work.

With the help of geospatial modeling, overall pavement surface conditions can be estimated based on a smaller number of survey sites. For the state of New Mexico, the minimum number of survey sites is approximately 40% of the number of sites currently being surveyed. This indicates that states like New Mexico could significantly reduce the number of sites surveyed in the future if they leverage the geospatial modeling approach evaluated here.

5.4 Conclusions

Routine evaluation of pavement surface distress conditions is a challenge to all transportation management agencies. Practicality does not current permit the collection of exhaustive condition data for all pavement assets, though technology is changing this (Zhang et al. 2016). Current assessment methods for pavement surface distress conditions are expensive and time-consuming. To overcome these limitations, we present a novel approach for overall pavement surface distress condition evaluation based on geospatial modeling. Our results have shown that geospatial modeling could effectively ($R^2 > 0.9$)

estimate overall pavement surface distress conditions based on traffic and environmental factors. In addition, for the state of New Mexico, the minimum number of survey sites required to estimate ODR within the bounds of manual measurement error (Bogus et al. 2010) is 4,000, less than 40% of what has been historically collected. These results show the potential for geospatial modeling techniques to estimate overall pavement surface distress condition with fewer survey sites, substantially reducing pavement surface condition assessment costs and time. This automated system would only require users to collect the geospatial data for the surveyed sites, upload the geospatial data to the system, while the computing-intensive process such as model development is fully automated.

Chapter 6 Summary and Conclusions

This section provides a comprehensive and integrated conclusion based on the research results obtained from the three independent studies in the previous sections (Section 3, 4, and 5). This section also discusses the limitations of the research and their implications for future research. Although each of the three studies explores the utility of a specific GT (e.g., geospatial modeling), they are all applied in the context of pavement surface distress evaluation in the United States.

6.1 Summary of Research Results

Three geospatial technologies (GT), including high-spatial resolution natural color digital aerial photography (HiSR-DAP), hyper-spatial resolution digital aerial photography (HySR-DAP), and geospatial modeling, can permit rapid assessment of pavement surface distress conditions at a low cost. Specifically, the results have shown that HiSR-DAP of 6-inch spatial resolution can be used to evaluate the overall pavement surface distress conditions with a high degree of certainty ($R^2 > 95\%$). At a lesser degree of certainty ($R^2 > 82\%$ and $R^2 > 72\%$ respectively), 12-inch and 24-inch HiSR-DAP can also be used to assess overall pavement surface distress conditions.

Using HySR-DAP acquired from a small-unmanned aircraft system (S-UAS) as input, aerial triangulation (AT) can be used to generate millimeter scale orthophotos and digital surface models (DSMs) and these products can be effectively used to characterize detailed pavement surface distresses comparable to ground-based manual measurement (at a 5% significant level). This finding lays the foundation for future research into S-UAS based automated pavement surface distress evaluation.

Geospatial modeling can effectively ($R^2 > 90\%$) estimate overall pavement surface distress conditions based on traffic and environmental factors. In addition, for the state of New Mexico, the minimum amount of survey sites required to estimate overall pavement surface distress rates within the bounds of manual measurement error is 4,000, less than 40% of what has been historically collected.

6.1.1 Appropriate Application of Each Proposed Method

Each proposed method has a different application or focus in the context of pavement surface distress evaluation. The evaluation of pavement surface distress conditions using HiSR-DAP could be used as a rapid and cost-effective predictor of overall pavement surface distress conditions for routine, high-level information checks. This method could also be used to evaluate overall pavement surface distress conditions where field inspections are not possible to perform. It is not likely that this method will completely replace field inspection due to its lack of detailed pavement surface distress information and the necessity of using field inspection results as reference data for model development. The HySR-DAP based method could be used to rapidly and cost-effectively measure detailed pavement surface conditions in situations where field inspectors cannot evaluate without considerable labor costs (e.g., sections in remote areas) or where survey vehicles cannot gain access. This method also holds the potential to completely replace currently adopted field inspection methods once restrictions on S-UAS operations are lifted. Geospatial modeling could be used to rapidly and cost-effectively estimate overall pavement surface distress conditions based on traffic and environmental factors with substantially reduced survey sites. This method is readily deployable and can successfully reduce approximately 60% the survey sites that have

been historically evaluated. For the same reasons as HiSR-DAP based method, geospatial modeling method is not likely to be able to completely substitute for field inspection, but it could be used for routine, high-level information checks.

6.1.2 Broader Research Impact

In a broader context, these proposed methods hold the potential to be beneficial to infrastructure management and asset management. Many infrastructure assets, especially those are spatially distributed such as oil and gas pipelines, bridges, and dams, also have the need to be routinely evaluated and monitored to examine their serviceability. The proposed methods can be modified and customized by researchers or practitioners from investigate the condition of other types of assets.

Because of the capability to detect both detailed horizontal and vertical distress, the HySR-DAP based method can also be used to monitor or assess subsidence or displacement of infrastructure and assets, especially for high-rise buildings or structures. HiSR-DAP and HySR-DAP can also be used by infrastructure management agencies to support asset mapping and infrastructure development programs as well as post-disaster infrastructure condition assessment (Jensen and Cowen, 1999; Ezequiel et al., 2014).

Coupled with higher temporal resolution and spatial resolution GIS and remote sensing data, geospatial modeling techniques hold a great potential for applications in predicting infrastructure conditions at a national level. For example, the U.S. Department of Transportation (DOT) could build a model to estimate the condition of the interstate highway systems.

In addition, major technological advances in GT have provided new tools to national management agencies to collect more accurate, timely and unbiased information about their infrastructure assets.

6.2 Research Limitations

For the HiSR-DAP based method, one limitation is that it has limited utility for high traffic volume (e.g., traffic congestion) pavement sections. This is because vehicles are considered to be noises that reduce the area of pavement observed in aerial images. Another limitation is that it is still necessary to collect reference pavement surface distress rates to develop initial model calibrations.

For the HySR-DAP based method, aerial images are collected via small-unmanned aircraft systems (S-UAS). Currently, due to a wide variety of regulatory and safety concerns, the legal use of S-UAS is severely restricted in the United States. Therefore, this proposed method is not operationally ready before the restrictions on beyond line-of-sight S-UAS operations are lifted. In addition, this proposed method detects pavement surface distress rates through manual digitization; automation is the logical next step.

For the geospatial modeling based method, the limitation is that it did not include the pavement material, pavement age, pavement design, pavement construction, pavement repair, and other important pavement maintenance data in the modeling due to lack of availability.

One common limitation of the three proposed methods is that they require researchers or practitioners in the infrastructure management communities have a certain

amount of geospatial knowledge and skills. The expectation is that GT will be leveraged for infrastructure management education in the near future to create a new generation of infrastructure engineers to effectively employ GT.

6.3 Implications for Future Research

Future research with regard to using GT for pavement surface distress evaluation is to follow. One possible future research topic is to explore the utility of other routinely-acquired and publicly-accessible terrestrial remote sensing data to evaluate pavement surface distress conditions. These terrestrial remote sensing data include data acquired by commercial companies such as Google. Google Street-View may provide detailed information for roadway pavement surface distress evaluation. The potential of using these terrestrial remote sensing data for transportation asset management should also be explored. For example, these data could be used to inventory various roadway assets (e.g., pavements, bridges, signage, and guardrails).

Another topic that warrants further research is the automation, both for filtering out unwanted features on the pavement such as vehicles and shadows and extraction of detailed distress metrics given the data volumes involved (Lippitt 2015). The promising technology for automation is geographic object-based image analysis (GEOBIA: Blaschke 2010). Algorithms will be developed to optimize the image segmentation to detect each individual distress.

The development of suitable S-UAS for operational pavement surface distress evaluation also warrants further research. The environment for pavement surface distress evaluation is characterized by constant traffic volume and extensive pavement sections. This unique environment requires S-UAS to be able to fly for a long duration. Short flight

time limits the operational use of S-UAS for pavement surface distress evaluation because a roadway is linearly distributed over an extensive area. More importantly, the safety mechanism of S-UAS should be maximized to prevent the occurrence of crashes which will cause traffic accidents, especially for the S-UAS operated above highways.

New evaluation protocols and distress metrics should be developed since S-UAS acquired HySR-DAP holds the potential to completely replace currently adopted pavement surface distress evaluation methods. Current evaluation protocols and distress metrics are developed to satisfy ground-based evaluation methods. S-UAS based evaluation opens a new evaluation paradigm.

Considering the data volume involved for statewide pavement surface distress evaluation, the improvement of database for condition data warrants further exploration. This is especially critical for HySR-DAP since the image size is large (big data). Coupled with internet of things (IoT), such a database will enable transportation agencies to inventory long-term pavement surface images which can provide these agencies with the capability to identify spatial and temporal patterns of pavement surface distress conditions from a primary record.

In recent years, many other sensors such as thermal infrared (TIR) cameras and LiDAR are becoming commercially available in miniaturized forms suitable for operation on S-UAS. Many of these sensors, while more expensive per sensor, have the potential to improve detailed pavement surface distress evaluation. The payload of S-UAS has been steadily improved and coupled with these TIR and LiDAR sensors, and there is great potential for their application in pavement surface distress condition evaluation. Future research should be performed to explore the utility of these sensors.

REFERENCES

- Aber, J., Aber, S.W., and Leffler, B. (2001). "Challenge of infrared kite aerial photography." *Transaction of the Kansas Academy of Science*, 104, 18–27.
- Aber, J., Sobieski, R., Distler, D., and Nowak, M. (1999). "Kite aerial photography for environmental site investigations in Kansas." *Transactions of the Kansas Academy of Science*, 102, 57–67.
- Adarkwa, O.A., and Attoh-Okine, N. (2013). "Pavement crack classification based on Tensor Factorization." *Journal of Construction and Building Materials*, 48, 853 – 857.
- Adlinge, S.S., and Gupta, A.K. (2015). "Pavement deterioration and its causes." *IOSR Journal of Mechanical and Civil Engineering*, 6(60), 9–15.
- Agresti, A., and Min, Y. (2003). *On sample size guidelines for teaching inference about the binomial parameter in introductory statistics*, Department of Statistics, University of Florida: Gainesville, FL.
- Ahmad, A. (2006). "Digital photogrammetry: an experience of processing aerial photography of UTM acquired using digital camera." *Proceedings of Asia GIS Conference*, UTM Skudai, Malaysia, 1–11.
- Airsight UAV Pavement Inspections. (2016). Retrieved March 14, 2016, from <https://www.air sight.de/en/consulting/uavaerodrome->

inspections.html#references

- Algina, J., and Keselman, H.J. (2000). "Cross-validation sample size." *Applied Psychological Measurement*, 24(2), 173–179.
- Akbari, H., Shea Rose, L., and Taha, H. (2003). "Analyzing the land cover of an urban environment using high-resolution orthophotographs." *Landscape Urban Plan*, 63(1), 1–14.
- Alkhder, M. (2010). "Analytical study of road pavement performance models for a sample of roads in Syria." *Damascus University Journal*, 26(2), 161-190.
- Al-Kheteeb, L.A., Saoud, A., and Al-Msouti, M.F. (2011). "Rutting prediction of flexible pavements using finite elements modeling." *Jordan Journal of Civil Engineering*, 5(2), 173–190.
- Alkire, B.D. (2013). "Pavement condition surveys." Retrieved July 29, 2013, from <http://www.cee.mtu.edu/~balkire/CE5403/Lec%204A.pdf>
- Al-Mansour, A. (2004). "Flexible pavement distress prediction model for the City of Riyadh, Saudi Arabia." *Emirates Journal for Engineering Research*, 9(1), 81-88.
- Anderson, R. E., Poon, A., Lustig, C., Brunette, W., Borriello, G., and Kolko, B. (2009). "Building a transportation information system using only GPS and basic SMS infrastructure." *Transactions of the IRE Professional Group*, 233-242.
- Aoki, K., Yamamoto, K., and Shimamura, H. (2012). "Evaluation model for pavement

Surface distress on 3D point clouds from mobile mapping system.” *Proceedings of International Archives of the Photogrammetry, Remote Sensing and Spatial Information Sciences*, Volume XXXIX-B1, Melbourne, Australia.

Arnold, T.B., and Emerson, J.W. (2011). “Nonparametric goodness-of-fit tests for discrete null distribution. *The R Journal*, 3, 458–472.

Ashur, S., and Crockett, B. (1997). “Geographic information systems as a support tool in construction cost estimating in state DOTs.” *Transportation Research Record*, 1575, 112-115.

Attoh-Okine, N. (2001). “Grouping pavement condition variables for performance modeling using self-organization maps.” *Computer-Aided Civil and Infrastructure Engineering*, 16, 112-125.

Attoh-Okine, N., and Adarkwa, O. (2013). *Pavement conditions surveys – overview of current practices*, Delaware Center for Transportation, University of Delaware: Newark, DE.

Balloon & Kite Mapping. (2014). Retrieved March 12, 2014, from <https://publiclab.org/wiki/balloon-mapping>

Balloon Regulations & Policies. (2014). Retrieved March 12, 2014, from https://www.faa.gov/aircraft/air_cert/design_approvals/balloons/balloons_regs/

Balz, T., and Liao, M. (2010). “Building-damage detection using post-seismic high-

resolution SAR satellite data.” *International Journal of Remote Sensing*, 31(3), 3369-3391.

Bandini, P., Bogus, S. M., Montoya, K., Pham, H., and Migliaccio, G. C. (2012).

Improving NMDOT's pavement distress survey methodology and developing correlations between FHWA's HPMS distress data and PMS data, Research Bureau, New Mexico Department of Transportation, Albuquerque, NM.

Beauvais, G.P., Keinath, D. A., Hernandez, P., Master, L., Thurston, R. (2006). “Element distribution modeling, Version 2.” Retrieved August 1, 2013 from

http://www.natureserve.org/prodServices/pdf/EDM_white_paper_2.0.pdf

Bednarz, S.W., Acheson, G., and Bednarz, R.S. (2006). “Maps and map learning in social studies.” *Journal of Social Education*, 70(7), 398 – 404.

Berman, E. (2011). “The current state of geospatial modeling.” *Proceedings of the 2nd*

International Conference on Computing for Geospatial Research & Applications,

5.

Blaschke, T. (2010). “Object based image analysis for remote sensing.”

ISPRS Journal of Photogrammetry and Remote Sensing, 65, 2–16.

Bogus, S. M., Song, J., Waggerman, R., and Lenke, L. (2010). “Rank correlation method for evaluating manual pavement distress data variability.” *Journal of Infrastructure*

Systems, 16(1), 66 – 72.

- Bolstad, P. (2005). *GIS fundamentals, a first text on geographic information systems, 2nd Edition*, Eider Press, White Bear Lake, MN.
- Bolstad, P. (2012). *GIS fundamentals, a first text on geographic information systems, 4th Edition*, Eider Press, White Bear Lake, MN.
- Boyle, K., and Petrie, C. (2009). "Mapping history, people, and ideas: geospatial modeling in the arts, humanities, and social science." *Lecture Presentation*, 2 December.
- Brecher, A., Noronha, V., and Herold, M. (2004). "UAV2003: a roadmap for deploying unmanned aerial vehicle (UAVs) in transportation." *Findings of Specialist Workshop in Santa Barbara, CA*.
- Breuer, P., Chmielewski, T., Gorski, P., and Konopka, E. (2002). "Application of GPS technology to measurements of displacements of high-rise structures due to weak winds." *Journal of Wind Engineering and Industrial Aerodynamics*, 90(3), 223-230.
- Brown, D., Dalton, J., and Hoyle, D. (2004). "Spatial forecast methods for terrorist events in urban environments." *Proceedings of the Second NSF/NIJ Symposium on Intelligence and Security Informatics*, Tucson, AZ.
- Brownjohn, J.M.W. (2007). "Structural health monitoring of civil infrastructure." *Philosophical Transactions of the Royal Society A*, 365, 589-622.

- Celebi, M. (2000). "GPS in dynamic monitoring of long-period structures." *Journal of Soil Dynamics and Earthquake Engineering*, 20, 477-483.
- Chambon, S., Gourraud, C., Moliard, J.M., and Nicolle, P. (2010). "Road crack extraction with adapted filtering and markov model-based segmentation-introduction and validation." *Proceedings of the 5th International Conference on Computer Vision Theory and Applications*, VISAPP, Angers, France.
- Chan, C., Huang, B., Yan, X., and Richards, S.H. (2009). "Effects of asphalt pavement conditions on traffic accidents in Tennessee utilizing pavement management." TRB 88th Annual Meeting Compendium of Papers (CD-ROM). Transportation Research Board, Washington, D.C.
- Chang, K., Chang, J., and Liu, J. (2005). "Detection of pavement distress using 3D laser scanning technology." *Proceedings of the International Conference on Computing in Civil Engineering*, Cancun, Mexico, 1-11.
- Chen, S., Rice, C., Boyle, C., and Hauser, E. (2011). "Small-format aerial photography for highway-bridge monitoring." *Journal of Performance of Constructed Facilities*, 25(2), 105-112.
- Chen, W., Yuan, J., and Li, M. (2012). "Application of GIS/GPS in Shanghai airport pavement management system." *Journal of Procedia Engineering*, 29, 2322-2326.
- Cheng, H.D., Jiang, X., Li, J., and Glazier, C. (1999). "Automated real-time pavement

- distress analysis.” *Transportation Research Record*, 1655, 55-64.
- Cheng, H.D., Miyojim, M. (1998). “Automatic pavement distress detection system.” *Journal of Information Sciences*, 108, 219–240.
- Chini, M., Pierdicca, N., and Emery, W. (2009). “Exploiting SAR and VHR optical images to quantifying damage caused by the 2003 Bam Earthquake.” *IEEE Transaction on Geoscience and Remote Sensing*, 47(1), 145-152.
- Cimons, M. (2011). “Impacts everything from navigating to law enforcement.” Retrieved June 1, 2016, from <http://gep.frec.vt.edu/VCCS/materials/2011/Intro/Handouts/1.5-Geospatial%20Technology%20as%20a%20Core%20Tool%20-%20US%20News%20and%20World%20Report.pdf>
- Clark, W.A.V., and Hosking, P.L. (1986). *Statistical methods for geographers*, John Wiley & Sons, New York.
- Colomina, I., and Molina, P. (2014). “Unmanned aerial systems for photogrammetry and remote sensing: a review.” *ISPRS Journal of Photogrammetry and Remote Sensing*, 92, 79–97.
- Congalton, R.G., and Green, K. (2009). *Assessing the accuracy of remotely sensed data—principles and practices, 2nd Edition*, Taylor & Francis: Boca Raton, FL.
- Cordova, A.A., Bogus, S.M., Migliaccio, G.C., and Lenke, L.R. (2009). *2009 Pavement Evaluation Report: Northern New Mexico*. University of New Mexico,

Albuquerque, NM

Coudray, N., Karathanou, A., and Chambon, S. (2010). "Multi-resolution approach for fine structure extraction – application and validation on road images." *Proceedings of the 5th International Conference on Computer Vision Theory and Applications*, VISAPP, Angers, France.

Cowen, D.J., and Jensen, J.R. (1998). *Extraction and modeling of urban attributes using remote sensing technology, peoples and pixels: linking remote sensing and social science*, National Academy Press, Washington, D.C.

Curphey, D. R., Fronek, D. K., and Wilson, J. H. (1985). "Highway pavement surface remote sensing using video image processing." *Proceedings of the ASCE Spring Convention*, ASCE, Denver, CO.

Dar, I.A., Sankar, K., and Dar, M.A. (2011). "Fluorine contamination in ground water: a major challenge." *Journal of Environmental Monitoring and Assessment*, 173, 597 – 610.

Delgado, L., Cordova, K., and Rodriguez, A.J. (2004). "Contribution of geospatial technology in tropical medicine and international health applications." Retrieved July 17, 2013, from <http://www.chiex.net/documents/Articulo%20Delgado%20et%20al.pdf>

Elbheiry, M.R., Kandil, K.A., and Kotb, A.S. (2011). "Investigation of factors affecting pavement roughness." *Engineering Research Journal*, 132, C1–C13.

- Epstein, J.M. (2008). "Why model?" *Journal of Artificial Societies and Social Simulation*, 11(4), 12.
- Ezequiel, C.A.F., Cua, M., Libatique, N.C., Tangonan, G.L., Alampay, R., Labuguen, R.T., Favila, C.M., Horado, J.L.E., Canos, V., Devaney, C., Loreto, A.B., Bacusmo, J., Palma, B. (2014). "UAV aerial imaging applications for post-disaster assessment, environmental management and infrastructure development." *Proceedings of the 2014 International Conference on Unmanned Aircraft Systems, ICUAS*, 274–283.
- Faghri, A., and Hamad, K. (2002). "Application of GPS in traffic management systems." *Journal of GPS Solutions*, 5(3), 52-60.
- Forest, R., and Utsi, V. (2004). "Non destructive crack depth measurements with Ground Penetrating Radar." *Proceedings of the Tenth International Conference on Ground Penetrating Radar*, IEEE, Delft, The Netherlands.
- Fraser, W., Carlson, J., Duley, P., Holm, E., and Patterson, D. (1999). "Using kite-based aerial photography for conducting Adelie penguin censuses in Antarctica." *Waterbirds*, 22, 435–440.
- Fridman, A.E. *The quality of measurements*, 1st Edition, Springer-Verlag: Heidelberg, Germany.
- Garber, N.J., and Hoel, L.A. (2009). *Traffic and highway engineering, 4th Edition*,

Cengage Learning, Toronto, Canada.

Gavilan, M., Balcones, D., Marcos, O., Llorca, D.F., Sotelo, M.A., Parra, I., Ocana, M.,

Aliseda, P., Yarza, P., and Amirola, A. (2011). “Adaptive road crack detection system by pavement classification.” *Sensors*, 11(10), 9628–9657.

Georgopoulos, A., Loizos, A., and Flouda, A. (1995). “Digital image processing as a tool for pavement distress evaluation.” *ISPRS Journal of Photogrammetry and Remote Sensing*, 50(1), 23–33.

Gewin, V. (2004). “Mapping opportunities.” *Nature*, 427, 376–377.

Gomarasca, M.A. (2012). *Basics of geomatics*, Springer, Heidelberg.

Gomez, R.B. (2002). “Hyperspectral imaging: a useful technology for transportation analysis.” *Optical Engineering*, 41(9), 2137–2143.

Graham, R., and Roger, E. R. (1987). *Manual of aerial photography*, London and Boston, Focal Press, New York, NY.

Gramling, W.L. (1994). *Determining pavement condition: NCHRP synthesis of highway practice No. 203*, Transportation Research Board, Washington, D.C.

Guo, H.D. (2010). “Understanding global natural disasters and the role of earth observation.” *International Journal of Remote Sensing*, 3, 221–230.

Guichard, F., Bourget, E., and Agnard, J. (2000). “High-resolution remote sensing of

- intertidal ecosystems: A low-cost technique to link scale-dependent patterns and processes.” *Limnology and Oceanography*, 45, 328–338.
- Haas, C., Shen, H., Phang, W. A., and Haas, R. (1985). “An expert system for automation of pavement condition inventory data.” *Proceedings of North American Conference on Managing Pavements*, Toronto, Canada.
- Haas, R., Hudson, W.R., and Zaniewski, J. (1994). *Modern pavement management*, Krieger, Malamar, Fla.
- Hair, J.F., Anderson, R.E., Tatham, R.L., and Black, W.C. (1998). *Multiple data analysis*, 4th Edition, Prentice Hall Inc., Upper Saddle River, New Jersey.
- Halfawy, M.R., Pyzoha, D., and El-Hosseiny, T. (2002). “An integrated framework for GIS-based civil infrastructure management systems.” *Proceedings of Annual Conference of the Canadian Society for Civil Engineering*, Montreal, Quebec, Canada.
- Halfawy, M.R., Vanier, D.J., and Hubble, D. (2004). “Integration of municipal information systems for sustainable management of infrastructure assets.” Retrieved July 11, 2013, from <http://archive.nrc-cnrc.gc.ca/obj/irc/doc/pubs/nrcc47663/nrcc47663.pdf>
- Hartgen, D.T., Fields, M.G., Feigenbaum, B. (2014). *21st annual report on the performance of state highway systems (1984-2012)*, Reason Foundation,

Los Angeles, CA.

Herold, M. (2007). *Remote sensing of impervious surfaces*, CRC Press,

Boca Raton, Florida.

Herold, M., Roberts, D. A., Smadi, O., and Noronha, V. (2004). “Road condition mapping using hyperspectral remote sensing.” Presented at the 2004 AVIRIS Workshop, Pasadena, California, March 31 – April 2, 2004.

Herold, M., and Roberts, D. A. (2005). “Spectral characteristics of asphalt road aging and deterioration: implications for remote-sensing applications.” *Applied Optics*, 44(20), 4328–4334.

Herold, M., Roberts, D., Noronha, V., and Smadi, O. (2008). “Imaging spectrometry and asphalt road survey.” *Transportation Research Part C*, 16, 153-166.

Highway Performance Monitoring System (HPMS) Field Manual 2014. (2014).

Retrieved May 12, 2014 from

[https:// www.fhwa.dot.gov/policyinformation/hpms/fieldmanual/HPMS_2014.pdf](https://www.fhwa.dot.gov/policyinformation/hpms/fieldmanual/HPMS_2014.pdf)

Hong, L. (2009). “Pavement information system: detection, classification, and compression.” Master’s thesis, The University of Toledo, Toledo, OH.

Hoskin, T. (2014). “Parametric and nonparametric: demystifying the terms.” Retrieved November 20, 2015, from <http://www.mayo.edu/mayo-edu-docs/center-for-translational-science-activities-documents/berd-5-6.pdf>

- Hudson, W. R. and Uddin, W. (1987). "Future pavement evaluation technologies: prospects and opportunities." *Proceedings of the 2nd North American Pavement Management Conference*, Toronto, Canada, Vol. 3, 3.233–3.258.
- Hudson, W. R., Elkins, G. E., Uddin, W., and Reilley, K. T. (1987). *Improved methods and equipment to conduct pavement distress surveys*, ARE, Inc., Massillon, OH.
- Huang, Y., and Xu, B. (2006). "Automatic inspection of pavement cracking distress." *Journal of Electronic Imaging*, 15(1), 0130171– 0130176.
- Imam, E. (2011). "Use of geospatial technology in evaluating landscape cover type changes in Chandoli National Park, India." *Journal of Computational Ecology and Software*, 1(2), 95 – 111.
- Isa, L.C.A.H.M., Masoem, D.M., and Hwa, L.T. (2005). "Pavement performance model for federal roads." *Proceedings of the Eastern Asia Society for Transportation Studies*, Vol. 5, 428-440.
- Janssen, V., Grinter, T., and Roberts, C. (2011). "Can RTP GPS be used to improve cadastral infrastructure?" *Engineering Journal*, 15(1), 43-54.
- Jensen, J.R. (2007). *Introductory digital image processing: a remote sensing perspective*, 3rd Edition, Upper Saddle River, NJ.
- Jensen, J.R., and Cowen, D.D. (1999). "Remote sensing for urban/suburban infrastructure and socio-economic attributes." *Photogrammetric Engineering and Remote*

Sensing, 81, 709–720.

Kersten, T. (1999). “Digital aerial triangulation in production—experiences with block Switzerland.” *In Photogrammetric Week '99*; Wichmann, Verlag: Heidelberg, Germany, Stuttgart, Germany, 193–204.

Kim, H., Soleymani, H., Han, H., Nam, H. (2006). “Evaluation of asphalt pavement crack sealing performance using image processing technique.” *Proceedings of the International Symposium on Automation and Robotics in Construction*, IAARC, Tokyo, Japan, 341–345.

Koch, C., and Brilakis, I. (2011). “Pothole detection in asphalt pavement images.” *Advanced Engineering Informatics*, 24, 507–515.

Kveiborg, O., and Fosgerau, M. (2007). “Decomposing the decoupling of Danish road freight traffic growth and economic growth.” *Transport Policy*, 14, 39–48.

Kulkarni, R.B., and Miller, R. W. (2002). “Pavement management systems: past, present, and future.” Retrieved August 1, 2013, from http://www.ltrc.lsu.edu/TRB_82/TRB2003-000210.pdf

Kushwaha, S.P.S., and Roy, P.S. (2003). “Geospatial technology for wildlife habitat evaluation.” *Journal of Tropical Ecology*, 43(1), 137-150.

Lambers, K., Eisenbeiss, H., Sauerbier, M., Kupferschmidt, D., Gaisecker, T, Sotoodeh, S., and Hanusch, T. (2007). “Combing photogrammetry and laser scanning for the

- recording and modeling of the late intermediate period site of Pinchango Alto, Palpa, Peru.” *Journal of Archaeological Science*, 34, 1702-1712.
- Lebourgeois, V., Begue, A., Degenne, P., and Bappel, E. (2010). “Improving harvest and planting monitoring for smallholders with geospatial technology: the Reunion Island experience.” *International Sugar Journal*, 109 (1298), 109-119.
- Lee, H. D., and Kim, J. J. (2005). “Development of a crack type index.” *Transportation Research Record*, 1940, 99–109.
- Lee, J., and Wong, D.W.S. (2001). *Statistical analysis with ArcView GIS*. Wiley, New York, NY
- Leipnik, M., Kemp, K., and Loaiciga, H. (1993). “Implementation of GIS for water resources planning and management.” *Journal of Water Resources Planning and Management*, 119(2), 184-205.
- Lemer, A.C.(1998). “Progress toward integrated infrastructure-assets-management systems: GIS and beyond.” Retrieved July 19, 2013, from <http://citeseerx.ist.psu.edu/viewdoc/download?doi=10.1.1.6.4080&rep=rep1&type=pdf>
- Lenz, R.W. (2011). *Pavement design guide – flexible pavement design system (FPS) 19: users’ manual*, Texas Department of Transportation, Austin, TX.
- Lettsome, C.A., Tsai, Y., and Kaul, V. (2012). “Enhanced adaptive filter-bank-based Automated pavement crack detection and segmentation system.”

Journal of Electronic Imaging, 21(4), 043008.

Li, D., Shan, J., and Gong, J. (2009). *Geospatial technology for earth observation*, Springer, New York, NY.

Li, X., Xu, Z., Qiu Y., Qi, J., Tang, S. (2013). “Application of GIS technique in environmental impact assessment.” *Progress in Environmental Science and Engineering*, 610, 831-835.

Li, Q., Zou, Q., Zhang, D, and Mao, Q. (2011). “FoSA: F* seed-growing approach for crack-line detection from pavement images.” *Journal of Image and Vision Computing*, 29, 861-872.

Li, Q., Yao, M., Yao, X., and Xu, B. (2010). “A real-time 3D scanning system for pavement distortion inspection.” *Measurement Science and Technology*, 21(1), 015702.

Lippitt, C.D. (2015). “Perspectives from the field: Remote sensing from small unmanned platforms: A paradigm shift.” *Environmental Practice*, 17(3), 235–236.

Liu, J., and Mason, P.J. (2009). *Essential image processing for GIS and remote sensing*, Wiley-Blackwell, Oxford, UK.

Liu, T., and Yang, X. (2012). “Geospatial modeling of urban landscape changes through an agent-based approach.” *Proceedings of 2012 AutoCarto International Symposium on Automated Cartography*, 16-18 September.

- Lou, Z., Gunaratne, M., Lu, J.J., and Dietrich, B. (2001). "Application of neural network model to forecast short-term pavement crack condition: Florida case study." *Journal of Infrastructure Systems*, 7, 166-171.
- Loukeri, E.D., and Chassiakos, A.P. (2004). "Development of pavement performance models using fuzzy systems." *Proceedings of the Fourth International conference on Engineering Computational Technology*, Stirlingshire, UK, Paper 129.
- Lu, W., Cheng, S., Yang, H., and Liu, D. (2008). "Application of GPS technology to build a mine-subsidence observation station." *Journal of China University of Mining and Technology*, 18(3), 377-380.
- Lytton, R.L. (1987). "Concepts of pavement performance prediction and modeling." *2nd North American Pavement Management Conference*, Canada, Vol. 2, 2.3-2.20.
- Ma, C.X. (2008). "Pavement distress detection based on nonsubsampling contourlet transform ." *Proceedings of the International Conference on Computer Science and Software Engineering*, CSSE, Wuhan, China, 28–31.
- Mamlouk, M. (2013). "Pavement distress and evaluation." Retrieved July 16, 2013, from <http://pavement.engineering.asu.edu/wordpress/wp-content/uploads/2013/02/Mamlouk2.pdf>
- Mann, H.B., and Whitney, D.R. (1947). "On a test of whether one of 2 random variables is stochastically larger than the other." *The Annals of Mathematical Statistics*, 18, 50–60.

Mannering, F.L, Washburn, S.P., and Kilareski, W.P. (2009).

Principles of highway engineering and traffic analysis, 4th edition, John Wiley & Sons, Inc., Hoboken, NJ.

Mannering, F.L., and Washburn, S.S. (2012). *Principles of highway engineering and traffic analysis, 5th edition*, John Wiley & Sons, Inc., Hoboken, NJ.

Mahler, D. S., Kharoufa, Z. B., Wong, E. K., and Shaw, L. G. (1991). "Pavement distress analysis using image processing techniques." *International Journal of Microcomputers in Civil Engineering*, 6(1), 1–14.

Marzloff, I., and Poesen, J. (2009). "The potential of 3D gully monitoring with GIS using high-resolution aerial photography and a digital photogrammetry system." *Geomorphology*, 111, 48–60.

Maser, K.R. (1996). "Condition assessment of transportation infrastructure using ground-penetrating RADAR." *Journal of Infrastructure Systems*, 2(2), 94–101.

Matsuoka, M., and Yamazaki, F. (2004). "Use of satellite SAR intensity imagery for detecting building areas damaged due to earthquakes." *Journal of Earthquake Spectra*, 20(3), 975-994.

McGhee, K. H. (2004). *Automated pavement distress collection techniques – a synthesis of highway practice*, National Cooperative Highway Research Program, Transportation Research Board, Washington, D.C.

- McMaster, H. M., and Legault, A. R. (1952). *Pavement condition surveys by means of aerial photograph*, University of Nebraska Press, Lincoln, NE.
- Migliaccio, G.C., Zandbergen, P.A., and Martinez, A.A. (2015). “Assessment of methods for adjusting construction cost estimates by geographical location.” *Journal of Construction Engineering and Management*, 31(2), 04014037.
- Mintsis, G., Basbas, S., Papaioannou, P., Taxiltaris, C., and Tziavos, I.N. (2004). “Applications of GPS technology in the land transportation system.” *European Journal of Operational Research*, 152(2), 399-409.
- Montoya, K., and Mann, J. Personal communication, May 19, 2015.
- Mustaffara, M., Ling, T.C., and Puan, O.C. (2008). “Automated pavement imaging program (APIP) for pavement cracks classification and quantification – a photogrammetric approach.” *Proceedings of Congress of the International Society for Photogrammetry and Remote Sensing*, Melbourne, Australia, 367–372.
- Nagai, M., Chen, T., Shibasaki, R., Kumugai, H., and Ahmed, A. (2009). “UAV-borne 3-D mapping system by multisensory integration.” *IEEE Transactions on Geoscience and Remote Sensing*, 47(3), 701–708.
- Neumann, K. J. (2008). “Trends for digital aerial mapping cameras.” *Proceedings of the International Archives of the Photogrammetry, Remote Sensing and Spatial Information Sciences*, Beijing, China, 551–554.

- Nguyen, T.S., Avila, M., Begot, S., Duculty, F., and Bardet, J.C. (2009). “Automatic detection and classification of defect on road pavement using anisotropy measure.” *Proceedings of the European Signal Processing Conference*, Glasgow, Scotland, 617–621.
- Nugent, G., Barker, B., Grandgenett, N., and Adamchuk, V. I. (2010). “Impact of robotics and geospatial technology interventions on youth STEM learning and attitudes.” *Journal of Research on Technology in Education*, 42(4), 391 – 408.
- Olamigoke, E.A., and Emmanuel, A.A. (2013). “The role of road transportation in local economic development: a focus on Nigeria transportation system.” *Developing Country Studies*, 3, 46–53.
- Oliveira, H., and Correia, P.L. (2008). “Identifying and retrieving distress images from road pavement surveys.” *Proceedings of the 1st Workshop on Multimedia Information Retrieval: New Trends and Challenges*, IEEE, San Diego, CA.
- Owolabi, A.O., Sadiq, O.M., and Abiola, O.S. (2012). “Development of performance models for a typical flexible road pavement in Nigeria.” *International Journal for Traffic and Transport Engineering*, 2(3), 178-184.
- Patterson, M.C.L., and Brescia, A. (2008). “Integrated sensor for UAS.” *Proceedings of the 23rd Bristol International Unmanned Air Vehicle Systems (UAVS) Conference*, 07-09 April, Bristol, United Kingdom, 13.

Pearson, K. (1991). "On lines and planes of closest fit to systems of points in space."

Philosophical Magazine, 2(11), 559–572.

Peng, K., and Zhou, X. (2011). "Research for predicting road skid resistance based on

machine vision." *Proceedings of the GeoHuman International*

Conference II: Emerging Technologies for Design, Construction, Rehabilitation,

and Inspection of Transportation Infrastructure, Hunan, China, 57–63.

Petzold, R. G., and Freund, D. M. (1990). "Potential for geographic information systems

in transportation planning and highway infrastructure management."

Transportation Research Record, 1261, 1-9.

Peyret, F., Betaille, D., and Hintzy, G. (2000). "High-precision application of GPS in the

field of real-time equipment positioning." *Automation in Construction*, 9, 299-314.

Prakash, A., Sharma, B.N., and Kazmierowski, T.J. (1994). "Investigation into

observational variations in pavement condition survey." *Proceedings of the 3rd*

International Conference on Managing Pavements, Volume 2, Transportation

Research Board, Washington, D.C., 290–301.

Pynn, J., Wright, A., and Lodge, R. (1999). "Automatic identification of cracks in road

surfaces." *Proceedings of International Conference on Image Processing and Its*

Applications, IEEE, Manchester, UK, 671–675.

Rango, A.S., Laliberte, A.S., Herrick, J.E., Winters, C., and Havstad, K. (2008).

- “Development of an operational UAV/remote sensing capability for rangeland management.” *Proceedings of the 23rd Bristol International Unmanned Air Vehicle Systems (UAVS) Conference, 07-09 April, Bristol, United Kingdom, 9.*
- Rawlings, J.O., Pantula, S.G., and D.A. (1998). *Applied regression analysis: a research tool*, 2nd Edition, Springer, New York, NY.
- Reed, P. A. and Ritz, J. (2004). “Geospatial technology.” *Journal of the Technology Teacher*, 63(6), 17 – 20.
- Reichenbacher, M., and Einax, J.W. (2011). *Challenges in analytical quality assurance*, 1st Edition, Springer-Verlag: Heidelberg, Germany.
- Rezaeian, M., and Gruen, A. (2011). “Automatic 3D building extraction from aerial and space images for earthquake risk management.” *Georisk: Assessment and Management of Risk for Engineered Systems and Geohazards*, 5(1), 77-96.
- Rehor, M., and Bahr, H.P. (2007). “Detection and analysis of building damage caused by earthquakes using laser scanning data.” *Proceedings of the International Symposium on Strong Vrancea Earthquakes and Risk Mitigation, Bucharest, Romania.*
- Rodrigue, J., Comtois, C., and Slack, B. (2013). *The geography of transportation system*, 3rd Edition, Routledge, London, UK.
- Saarenketo, T., and Scullion, T. (2000). “Road evaluation with ground penetrating radar.”

- Journal of Applied Geophysics*, 43, 119–138.
- Safaei, M., Omar, H., Yousof, Z.B.M., and Ghiasi, V. (2010). “Applying geospatial technology to landslide susceptibility assessment.” *Electronic Journal of Geotechnical Engineering*, 15, 677 – 696.
- Salama, H.K., Chatti, K., and Lyles, R.W. (2006). “Effect of heavy multiple axle trucks on flexible pavement damage using in-service pavement performance data.” *Journal of Transportation Engineering*, 132(10), 763–770.
- Samadzadegan, F., and Rastiveisi, H. (2008). “Automatic detection and classification of damaged buildings, using high resolution satellite imagery and vector data.” *The International Archives of the Photogrammetry, Remote Sensing and Spatial Information Sciences*, 37(B8), 415-420.
- Scoffin, T. (1982). “Reef aerial photography from a kite.” *Coral Reefs*, 1, 67–69.
- Schnebele, E., Tanyu, B.F., Cervone, G., and Waters, N. (2015). “Review of remote sensing methodologies for pavement management and assessment.” *European Transportation Research Review*, 7(2), 1–19.
- Schott, J. R. (2007). *Remote sensing: the image chain approach*, 2nd Edition, Oxford University Press, New York, NY.
- Schowengerdt, R.A. (2006). *Remote sensing: models and methods for image processing*, 3rd Edition, Academic Press, Burlington, MA.

- Shahin, M.Y., and Kohn, S.D. (1979). *Development of a pavement condition rating procedure for roads, streets, and parking lots*, Army Construction Engineering Research Laboratory, Champaign, IL.
- Shamo, B., Asa, E., and Membah, J. (2015) “Linear spatial interpolation and analysis of annual average daily traffic data.” *Journal of Computing in Civil Engineering*, 29(1), 04014022.
- She, T.H., Aouad, G., and Sarshar, M. (1999). “A geographic information system (GIS) – based bridge management system.” *Computer-aided Civil and Infrastructure Engineering*, 14(6), 417-427.
- Sklaver, B., Manangan, A., Bullard, S., Svanberg, A., and Handzel, T. (2006). “Rapid imagery through kite aerial photography in a complex humanitarian emergency.” *International Journal of Remote Sensing*, 27, 4709–4714.
- Smith, T.M. (1994). “The impact of highway infrastructure on economic performance.” Retrieved June 1, 2016, from <http://www.fhwa.dot.gov/publications/publicroads/94spring/p94sp8.cfm>
- Smith, M., Chandler, J., and Rose, J. (2009). “ High spatial resolution data acquisition for the geosciences: Kite aerial photography.” *Earth Surface Processes and Landforms*, 34, 155–161.
- Sokolic, I. (2003). “Criteria to evaluation to the quality of pavement camera systems in

- automated evaluation vehicle.” Master’s thesis, University of New Mexico, Albuquerque, NM.
- Stoeckeler, E. G. (1968). *Use of color aerial photography for pavement evaluation studies in Maine*, State Highway Commission, Material and Research Division.
- Stoeckeler, E. G. (1970). “Use of aerial color photography for pavement evaluation studies.” *Highway Research Record*, 319, 40–57.
- Strahler, A.H., Woodcock, C.E., and Smith, J.A. (1986). “One the nature of models in remote sensing.” *Remote Sensing of Environment*, 20(2), 121–139.
- Strickland, J. (2015). *Predictive analytics using R*, Lulu Press, Raleigh, NC.
- Sunitha, V., Veeraragavan, A., Srinivasan, K.K., and Mathew, S. (2012). “Cluster-based pavement deterioration models for low-volume rural roads.” *International Scholarly Research Network*, 1-8.
- Tang, L., and Shao, G. (2015). “Drone remote sensing for forestry research and practice.” *Journal of Forestry Research*, 26, 791–797.
- Terzi, S. (2007). “Modeling the pavement serviceability ratio of flexible highway pavements by artificial neural networks.” *Journal of Construction and Building Materials*, 21, 590-593.
- Thakur, J. K. (2012). *Geospatial techniques for managing environmental resources*, Springer, Dordrecht.

- Timm, D.H., McQueen, J.M. (2004). *A study of manual vs. automated pavement condition surveys*, Alabama Department of Transportation, Montgomery, AL.
- Tomkins, C.C. (2006). "An Introduction to non-parametric statistics for health scientists." Retrieved November 22, 2015, from <http://www.uahsj.ualberta.ca/files/Issues/3-1/pdf/20.pdf>
- Tucker, M., and Cetinkaya, B. (2005). "Automatic detection of earthquake-damaged Buildings using DEMs created from pre- and post-earthquake stereo aerial photographs." *International Journal of Remote Sensing*, 26(4), 823-832.
- Tsai, Y., Wu, Y., Ai, C., and Pitts, E. (2012). "Critical assessment of measuring concrete joint faulting using 3D continuous pavement profile data." *Journal of Transportation Engineering*, 138(11), 1291-1296.
- Uddin, W., Hudson, W. R., and Elkins, G. E. (1987). *Evaluation of equipment for measuring voids under pavements*, ARE, Inc., Massillon, OH.
- U.S. Department of Transportation Federal Highway Administration. (2013). *Highway performance monitoring system field manual*, Washington, D.C.
- Usher, J., and Truax, D. (2001). *Exploration of remote sensing applicability within Transportation*, Remote Sensing Technologies Center, Mississippi State University, Starkville, MS.
- Van Manen, N., Scholten, H.J., and Van De Velde, R. (2009). "Geospatial technology

- and the role of location in science.” *Geojournal Library*, 96, 1–13.
- Verhoeven, G. (2009). “Providing an archaeological bird’s-eye view—An overall picture of ground-based means to execute low-altitude aerial photography in archaeology.” *Archaeological Prospection*.16, 233–249.
- Vu, T. T. (2013). “Geospatial technology uses in post-disaster response – the power of the crowd.” *Journal of Disaster Advances*, 6(4), 1–3.
- Wang, H. (2007). “Application of GPS in railway project construction measures.” *Journal of Shanxi Architecture*, 12.
- Wang, K. C. P. (2000). “Designs and implementations of automated systems for pavement surface distress survey.” *Journal of Infrastructure Systems*, 6(1), 24–32.
- Wang, K.C.P., and Gong, W. (2002). “Automated pavement distress survey: a review and new direction.” *Proceedings of the 2002 Pavement Evaluation Conference*, Roanoke, Virginia, 21–25.
- Wang, K. C. P., and Li, X. (1999). “Use of digital cameras for pavement surface distress survey.” *Transportation Research Record*, 1675, 91–97.
- Westoby, M.J., Brasington, J., Glasser, N.F., Hambrey, M.J., and Reynolds, J.M. (2012). “Structure-from-motion photogrammetry: A low-cost, effective tool for geoscience applications.” *Geomorphology*, 179, 300–314.
- Wilcoxon, F. (1945). “Individual comparison by ranking methods.” *Biometrics Bulletin*,

1, 80–83.

Williams, K., Sader, S.A., Pryor, C., and Reed, F. (2006). “Application of geospatial technology to monitor forest legacy conservation easements.” *Journal of Forest*, 104(2), 89–93.

Wiyono, S. (2012). “The application of traffic simulation model to predict initiation and progression of crack for flexible pavements.” *Proceedings of 8th International Conference on Traffic and Transportation Studies*, 1-3 August, Changsha, China.

Wolters, A., Zimmerman, K., Schattler, K., and Rietgraf, A. (2011). *Implementing pavement management systems for local agencies*, Illinois Center for Transportation, Rantoul, IL.

Wright, P. (2014). *Missouri state wide imagery program*, Missouri GIS Advisory Council’s Data Development Committee, Office of Geospatial Information, Jefferson City, MO.

Wundram, D., and Loffler, J. (2008). “High-resolution spatial analysis of mountain landscapes using a low-altitude remote sensing approach.” *International Journal of Remote Sensing*, 27, 961–974.

Xu, Y. (2007). “Development and application of the GPS RTK in the highway construction.” *Bulletin of Surveying and Mapping*, 2, 18–20.

Yamazaki, F., Yano, Y., and Matsuoka, M. (2005). “Visual damage interpretation of

- buildings in Bam City using QuickBird images following the 2003 Bam, Iran Earthquake.” *Earthquake Spectra*, 21(S1), 329-336.
- Yu, S., Sukumar, S.R., Koschan, A.F., Page, D.L., and Abidi, M.A. (2007). “3D reconstruction of road surfaces using an integrated multi-sensory approach.” *Optics and Lasers in Engineering*, 45(7), 808–818.
- Yuan, X., Fu, J., Sun, H., and Toth, C. (2009). “The application of GPS precise point positioning technology in aerial triangulation.” *ISPRS Journal of Photogrammetry and Remote Sensing*, 64, 541–550.
- Zhang, S., Bogus, S.M. (2014). “Use of low-cost remote sensing for infrastructure management.” *Proceedings of the Construction Research Congress 2014*, ASCE, Atlanta, GA, 1299–1307.
- Zhang, S., Bogus, S.M., Neville, P.R.H., Zhang, G., Chen, C., and Valentin, V. (2015) “Extracting pavement surface distress conditions based on high spatial resolution multispectral digital aerial photography.” *Photogrammetric Engineering and Remote Sensing*, 81(9), 709–720.
- Zhang, Z., Dossey, T., Weissmann, J., and Hudson, W.R. (1994). “GIS integrated pavement and infrastructure management in urban areas.” *Transportation Research Record*, 1429, 84–89.
- Zhang, S., Lippitt, C.D., Bogus, S.M., Loerch, A.C., Sturm, J.O. (2016). “The accuracy

- of aerial triangulation products automatically generated from hyper-spatial resolution digital aerial photography.” *Remote Sensing Letters*, 7, 160–169.
- Zhang, S., Lippitt, C.D., Bogus, S.M. and Neville, P.R.H. (2016). “Characterizing pavement surface distress conditions with hyper-spatial resolution natural color Aerial photography.” *Remote Sensing*, 8(5), 392-1–392-23.
- Zhang, S., Migliaccio, G.C., Zandbergen, P.A., and Guindani, M. (2014). “Empirical assessment of geographically based surface interpolation methods for adjusting construction cost estimates by project location.” *Journal of Construction Engineering and Management*, 140(6), 04014015.
- Zhang, Y., Xiong, J., and Hao, L. (2011). “Photogrammetric processing of low altitude images acquired by unpiloted aerial vehicles.” *The Photogrammetric Record*, 26(34), 190–211.
- Zhou, G., and Zang, D. (2007). “Civil UAV system for earth observation.” *Proceedings of the International Geoscience and Remote Sensing Symposium (IGARSS)*, 23-27 July, Barcelona, Spain, 5319–5322.
- Zomrawi, H., Hussien, M.A., and Mohamed, H. (2011). “Accuracy evaluation of digital aerial triangulation.” *International Journal of Engineering and Innovative Technology*, 2, 7–11.

Appendix A. Flexible Pavement Distress Evaluation Reference Chart

DISTRESS	SEVERITY	EXTENT
<p>Raveling & Weathering:</p> <p>The wearing away of the pavement surface, due to dislodged aggregate particles and loss of asphalt binder. Normally the extent will be throughout the test section.</p>	<p>Low: Aggregate or binder has started to wear away on pavement surface. Some dislodged aggregate can be found on the shoulder. (1)</p> <p>Med: Aggregate or binder has worn away. Surface texture is rough and pitted. (2)</p> <p>High: Aggregate and/or binder has worn away, and surface texture is severely rough and pitted. (3)</p>	<p>Low: 1% to 30% of test section. (1)</p> <p>Med: 31% to 60% of test section. (2)</p> <p>High: 61% of test section, or more. (3)</p>
<p>Bleeding:</p> <p>A film of bituminous material on the pavement surface.</p>	<p>Low: Film is evident, but aggregate can still be seen. Spotty. (1)</p> <p>Med: Film is clearly seen, covers most of the aggregate, and is a little sticky. (2)</p> <p>High: Film is predominant, very sticky, and material is thick enough to shove. (3)</p>	<p>Low: 1% to 30% of test section. (1)</p> <p>Med: 31% to 60% of test section. (2)</p> <p>High: 61% of test section, or more. (3)</p>
<p>Rutting and Shoving:</p> <p>Longitudinal surface depressions in wheel path. (Check with a 4-foot rut bar.)</p>	<p>Low: ¼-inch to ½-inch in depth. (1)</p> <p>Med: ½-inch to 1-inch in depth. (2)</p> <p>High: More than 1-inch in depth. (3)</p>	<p>Low: 1% to 30% of test section. (1)</p> <p>Med: 31% to 60% of test section. (2)</p> <p>High: 61% of test section, or more. (3)</p>
<p>Cracks:</p> <p>Longitudinal Cracks: Wheel Track Mid-Lane Center Line</p> <p>Transverse Cracks: Full Width</p>	<p>Low: Sealed or non-sealed with a mean width of less than ¼-inch. May have very minor spalls. (1)</p> <p>Med: <u>A.</u> Sealed or non-sealed, and moderately spalled. Any width. <u>B.</u> Sealed, but sealant separated, allowing water to penetrate. <u>C.</u> Non-sealed cracks that are not spalled, but are over ¼-inch wide. <u>D.</u> Low severity alligator cracks exist near crack, or at the corners of intersecting cracks. <u>E.</u> Causes a significant bump to a vehicle. (2)</p> <p>High: <u>A.</u> Severely spalled. (Any width.) <u>B.</u> Medium to high severity alligator cracks exists near the crack, or at the corners of intersecting cracks. <u>C.</u> Causes a severe bump to a vehicle. (3)</p>	<p>Low: 1% to 30% of test section. (1)</p> <p>Med: 31% to 60% of test section. (2)</p> <p>High: 61% of test section, or more. (3)</p>
<p>Alligator Cracks:</p> <p>Pattern of interconnected cracks resembling chicken wire or alligator skin.</p>	<p>Low: Hairline, disconnected cracks. 1/8-inch wide, or less. No spalls. (1)</p> <p>Med: Fully developed cracks greater than 1/8-inch wide. Lightly spalled. (2)</p> <p>High: Severely spalled. Cells rock. May pump. (3)</p>	<p>Low: 1% to 30% of test section. (1)</p> <p>Med: 31% to 60% of test section. (2)</p> <p>High: 61% of test section, or more. (3)</p>
<p>Edge Cracks:</p> <p>Cracks which occur on the edge of the pavement.</p>	<p>Low: ¼-inch wide, or less. No spalls. (1)</p> <p>Med: Greater than ¼-inch wide. Some spalls. (2)</p> <p>High: Severely spalled. (3)</p>	<p>Low: 1% to 30% of test section. (1)</p> <p>Med: 31% to 60% of test section. (2)</p> <p>High: 61% of test section, or more. (3)</p>
<p>Patching:</p> <p>An area where the original pavement has been removed and replaced with similar or different material.</p> <p>Types of Patching: <u>Hot Mix Patch.</u> <u>Skin Patch.</u> <u>Other types (Please note on "note section" of the evaluation card.)</u></p>	<p>Low: Patch is present, and is in good condition. (1)</p> <p>Med: Somewhat deteriorated. Low to medium of any type of distress on patch. (2)</p> <p>High: Patch is deteriorated to point of soon or immediately needing replacement. (3)</p>	<p>Low: 1% to 30% of test section. (1)</p> <p>Med: 31% to 60% of test section. (2)</p> <p>High: 61% of test section, or more. (3)</p>

Appendix B. Flexible Pavement Distress Types and Ratings

Pavement Distress	Severity				Extent			
	None or Not Applicable	Low	Medium	High	None or Not Applicable	Low	Medium	High
Raveling & Weathering	0	1	2	3	0	1	2	3
Bleeding	0	1	2	3	0	1	2	3
Rutting & Shoving	0	1	2	3	0	1	2	3
Longitudinal Cracking	0	1	2	3	0	1	2	3
Transverse Cracking	0	1	2	3	0	1	2	3
Alligator Cracking	0	1	2	3	0	1	2	3
Edge Cracks	0	1	2	3	0	1	2	3
Patching	0	1	2	3	0	1	2	3

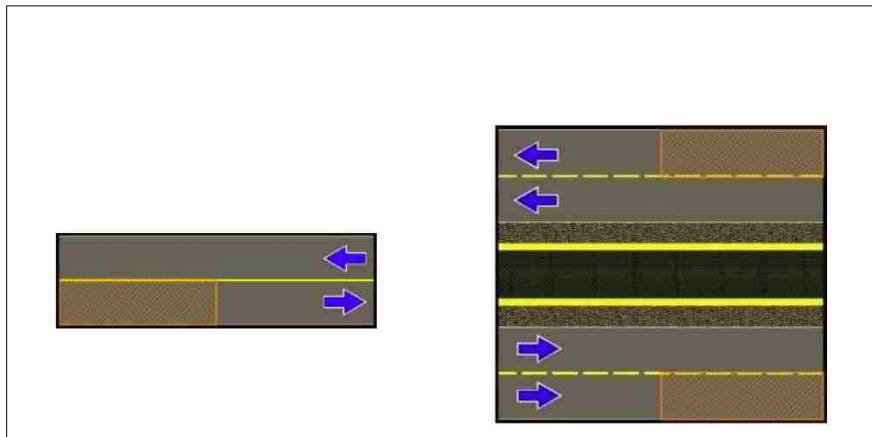
Appendix C. Rigid Pavement Distress Evaluation Reference Chart

DISTRESS	SEVERITY	EXTENT
Corner Break: Crack intersects joints at a distance less than 6 feet on either side, measured from the corner. Crack extends vertically through the entire slab thickness.	Low: Crack is tight (hairline). Well sealed cracks considered tight. No faulting or break-up. (1) Med: Crack is working and spalled at low or medium severity. No break-up of corner. Faulting of crack or joint less than ½- inch. Temporary patching may exist. (2) High: Crack is spalled at high severity; or the corner has broken into 2 or more pieces; or faulting more than ½-inch.(3)	Low: 1 to 3 per test section. (1) Med: 4 to 6 per test section. (2) High: 7 or more per test section. (3)
Faulting of Transverse Joints and Cracks: Elevation difference across a transverse joint or crack.	Low: Faulted joints or cracks which average 1/16-inch or less. (1) Med: Faulted joints or cracks which average more than 1/16-inch; but less than 1/4-inch. (2) High: Faulted joints or cracks which average 1/4-inch or more. (3)	Low: 1% to 30% of test section. (1) Med: 31% to 60% of test section. (2) High: 61% of test section, or more. (3)
Joint Seal Damage: Any condition which allows incompressible materials or water to infiltrate the joint from the surface. <u>Types of joint seal damage:</u> (1. Joint sealant stripping. 2. Joint sealant extrusion. 3. Weed growth. 4. Hardening of filler. 5. Loss of bond to slab edges. 6. Joint sealant absence.)	Low: Sealer is in generally good condition, with only minor damage. Little water and no incompressible can infiltrate the joint. (1) Med: Sealer is in generally fair condition, with one or more types) of damage occurring to a moderate degree. Water and also some incompressible can infiltrate easily. (2) High: Sealer is in generally poor condition, with one or more types of damage occurring to a severe degree. Water and incompressible infiltrate freely. (3)	Low: 1% to 30% of test section. (1) Med: 31% to 60% of test section. (2) High: 61% of test section, or more. (3)
Lane/Shoulder Drop-Off or Heave: The difference in elevation between the traffic lane and the shoulder.	Low: Elevation difference: ¼-inch to ½-inch. (1) Med: Elevation difference: ½-inch to 1 inch.(2) High: Elevation difference: One inch or more. (3)	Low: 1% to 30% of test section. (1) Med: 31% to 60% of test section. (2) High: 61% of test section, or more. (3)
Longitudinal Cracks: Cracks which run generally parallel, to the pavement centerline.	Low: Hairline crack with no spalling or faulting. (1) Med: Working crack with low, to moderately severe spalling and/or faulting less than ½-inch. (2) High: Crack greater than 1-inch wide; high severity spalling; faulted ½-inch or more. (3)	Low: 1 to 3 per test section. (1) Med: 4 to 6 per test section. (2) High: 7 or more per test section. (3)
Patch Deterioration: Area where part of the original pavement has been replaced or covered with similar or different material.	Low: Patch functioning well with little or no deterioration. Low severity spalling of patch edges may exist. Faulting across the slab-patch joint less than ¼-inch. Rated low, even if in excellent condition. (1) Med: Patch has low severity cracking, and/or some spalling of medium severity around the edges. Temporary patches have been placed because of permanent patch deterioration. (2) High: Patch has deteriorated to a condition which requires replacement, due to spalling, rutting or cracking within the patch. (3)	Low: One per test section. (1) Med: Two per test section. (2) High: Three or more per test section. (3)
Spalling of Transverse and Longitudinal Joints and Cracks: Cracking, breaking or chipping of slab edges within 2 feet of the joint. Spall does not extend vertically through the slab, but angles through the slab to the joint or crack.	Low: Spall less than 2-feet long; if spall is broken and fragmented, it must not extend more than 3-inches from joint/crack. Spalls <u>more</u> than 2-feet long with spall held tightly in place; if cracked, only 2 or 3 pieces. Joint/crack is lightly frayed: fray extends less than 3 inches from edge of joint/crack. (1) Med: One of the following conditions exists: A. Spall broken into pieces; spall extends more than 3 inches from joint/crack. B. Some/all pieces loose or missing; do not present a hazard. C. Joint/crack moderately frayed; fray extends more than 3". D. Temporary patching may exist. (2) High: Joint is severely spalled, spall is broken into pieces. Tire damage hazard. Requires speed reduction. (3)	Low: 1% to 30% of test section. (Normally, the extent will be throughout the test section.) (1) Med: 31% to 60% of test section. (2) High: 61% of test section, or more. (3)
Transverse and Diagonal Cracks: Medium or high severity cracks are working cracks, and are considered major structural distresses. (Note: hairline cracks that are less than 6-feet long are not rated.)	Low: Hairline crack without spalling or faulting. Well-sealed crack without visible faulting or spalling. (1) Med: Working crack with low to moderately severe spalling, and, or faulting less than ½-inch. (2) High: Crack greater than 1-inch wide; High severity spalling; faulted ½-inch or more. (3)	Low: 1 to 3 per test section. (1) Med: 4 to 6 per test section. (2) High: 7 or more per test section. (3)

Appendix D. Rigid Pavement Distress Types and Ratings

Pavement Distress	Severity				Extent			
	None or Not Applicable	Low	Medium	High	None or Not Applicable	Low	Medium	High
Corner Break	0	1	2	3	0	1	2	3
Faulting of Transverse Joints and Cracks	0	1	2	3	0	1	2	3
Joint Seal Damage	0	1	2	3	0	1	2	3
Lane/Shoulder Drop-Off or Heave	0	1	2	3	0	1	2	3
Longitudinal Cracking	0	1	2	3	0	1	2	3
Patch Deterioration	0	1	2	3	0	1	2	3
Spalling of Joints and Cracks	0	1	2	3	0	1	2	3
Transverse & Diagonal Cracks	0	1	2	3	0	1	2	3

Appendix E. Illustration of Test Sections on Two-Lane and Four-Lane Highways



Data are collected only in the positive direction on two-lane highways (one lane each direction). In addition, data are collected in the far right driving lane and never in passing lanes, turning lanes, or on the shoulder. For multi-lane highways (four or more through lanes combined in each direction), data are collected in both the positive and negative directions at a given milepost. In the positive direction the pavement evaluation is conducted from a given milepost plus 530 feet, while in the negative direction the evaluation is conducted from a given milepost minus 530 feet. This ensures that the pavement sections evaluated at a given milepost are parallel to each other. Like two-lane highways, the evaluation is conducted in the far right driving lane, and never in a passing lane, turning lane or on the shoulder.